BHUTAN HydroMet Journal

Volume III

National Centre for Hydrology and Meteorology
Royal Government of Bhutan
Thimphu: Bhutan

March 2025

Bhutan Hydro-Met Journal, March 2025
Published by National Centre for Hydrology and Meteorology

Address: Doeboom Lam,
Thimphu: Bhutan
P.O. Box No: 207
Website: www.nchm.gov.bt
Tel. No.: +975-2-327202
Fax No.: +975-2-327202

Editorial Note

Bhutan HydroMet Journal was started in 2022 and the first volume of the journal was launched successfully on 28th June 2022 during the 8th Board Meeting of National Centre for Hydrology and Meteorology. With the objective to institute research culture in the field of hydrology, meteorology, climate studies and cryosphere both within and outside the Centre, the editorial team for the Bhutan HydroMet Journal is happy to bring out the third volume of the journal with four scientific articles. Although the Bhutan HydroMet Journal is in its second year of publication, the editorial team has made all effort to follow the standards of international scientific journals. The aim of this journal is to disseminate the science-based information generated through extensive research process to the readers and particularly to the planners and decision makers to enable them to take decisions and make plans accordingly. Therefore, we hope that through this journal the scientific communities, students, decision makers, planners and general public will be greatly benefited. The editorial team would like to acknowledge all the support received from the management of the Centre in bringing out the second volume of Bhutan HydroMet Journal. We also would like to express our sincere gratitude to all the authors for their cooperation and tireless effort in finalizing their articles. We hope that the next volume (Bhutan HydroMet Journal, Vol.IV) will have more scientific articles and we would like to assure that the team will work together towards enhancing the journal.

Karma Toeb
Chief Editorial

Content

The atmospheric dynamics and meteorological processes associated with the rare and historic snowfall of 2021–22 winter season in Bhutan

Karma Tsering
International Centre for Integrated Mountain Development (ICIMOD)
Kathmandu, Nepal

Abstract

Preceded by at least two months of cold spell, the weather of the 2021–2022 winter season over the Bhutan Himalayas was remarkable due to extreme snowfall events, which in some places, had never occurred in the last six decades. The aggregates of repeated snowfalls in places surpassed the season's cumulative records since observation began on a systematic and regular basis. That winter was also unusual because of its early onset at the height of post-monsoon (September, October, November), and then continuing into early spring, (March, April, May) leading to one of the longest snow-dominated winter season in the Bhutan Himalayas in recorded history. The study of such rare events is of utmost importance as such extreme seasons have a significant impact on the human population and environment not only during such an event's occurrence but also all through the year. The analysis of the 2021–2022 winter snowfall was challenging given the sparse observations, the cloud contamination of the available satellite imageries, and the coarse resolution of modelled outputs, whether in retrospective or predictive configuration. Nonetheless, the study undertook an in-depth examination of the synoptic features and mesoscale dynamics associated with such a historic snowfall, thereby enhancing our understanding of rare, anomalous snowfall events. The study method adopted both qualitative and quantitative approaches in synthesising datasets and information from observations, reanalysis, mainstream media reports, social media posts, narratives around people's perceptions, and heuristic interpretation. The study shows that the aforesaid winter's exceptional snowfalls were the consequence of multiple meridional and zonal atmospheric phenomena preceding the snowfall event. The synoptic components that were involved in the lead-up to the event were the following: amplification and blocking of the subtropical westerly jet (SWJ) stream to spin up vortices of western disturbances (WDs); moisture exchange with a tropical depression carrying moisture north from the Bay of Bengal increasing the baroclinic instability; SWJ excitation due to dynamic coupling with the tropical depression, thereby further intensifying the WDs; cyclonic perturbations further strengthened as moisture-laden air mass is deflected upslope in contact with the high Himalayan range; vertical motion of the SWJ created centres of low-level cyclonic convergence and upper-level anti-cyclonic divergence; deepening low pressure near the south-west foothills of Bhutan pulled in more extratropical moisture plumes into the system; the active subtropical jet stream transported moisture deep into low-lying inner valleys like Punakha; and finally, the cold air mass from the high latitude penetrated deep into the mountains and spilled over into the adjacent plains, thereby dipping the surface temperature to near-freezing point. The timing and phasing of the extratropical westerly jet and the moisture flux from the tropical depression resulted in an atypical juxtaposition of moisture and cold air. This optimal phasing within the circulation pattern was key to the production of record snowfall in many places across Bhutan. This report assesses the 2021–22 winter snowfall through analyses of historical observations, climate reanalysis, and model simulations, as well as a review of the key published literature.

Introduction

Extreme weather events are part of the natural climate system, but they are relatively infrequent. Records of observations in recent decades show that some kinds of extreme weather events have become more common. Often in the past, people linked some of these general increases to climate change, so it was challenging for researchers and climate scientists to clarify the influence of climate change on specific extreme weather events. But advances in information technology and high-performance computing infrastructure over the last decade have enabled scientists to take on these challenges to provide evidence-based answers (ICIMOD, 2019). With improved methodologies, tools, and techniques, scientists can now not only determine the extent to which climate change contributes to some extreme weather events but also state with confidence that certain extreme weather events would not or could not have occurred but for climate change. Countless assessment reports and peer-reviewed papers have concluded that the climate is warming; and that most or all of the warming in the recent decades has to do with anthropogenic causes (Seneviratne et al., 2021).

Extreme weather attribution can provide valuable and actionable information on the future prevalence and severity of extreme events. It can also support decision making to strike a right balance in rationalising efforts and investments between mitigation and adaptation. Extreme-event interpretation and attribution are an emerging focus of investigative and interrogative climate change studies to connect attribution science to decision making (Stott and Walton, 2013).[i] Now there is sufficient knowledge and realisation that climate change significantly influences regional-scale weather while enforcing certain control over the magnitude and frequency of extreme events. Events like the 2021–22 winter snowfall elicit quick public responses that manifest the degree of societal resilience, vulnerability, and preparedness in addressing the impacts and reimagining measures to consolidate situational awareness and action. Yet, the aforesaid snowfall event is not unprecedented when viewed from the perspective of its unexpected occurrence; or due to the improbable phases in the state and dynamics of the atmosphere. Therefore, it is important to investigate the synoptic and mesoscale meteorological processes that intensify such occurrences and advance our knowledge for better prediction of future extreme events in all the weather elements. It is also highly relevant to understand the initialisation and evolution of this atypical event in order to improve future operational forecasts for better snow-related risk and resource management. Explaining and understanding how long-term global change affects the intensity and likelihood of extreme weather events continue to hold up as a frontier science challenge (Herring et al., 2014).

Winters in the Himalayas are dominated by the so called “Western Disturbances” (WD) (Venkiteshwaran, 1939), which are extratropical depressions of non-monsoonal precipitation pattern originating in the Mediterranean region being driven eastward by the westerlies. The westerlies’ wind system transports the moist entrainment triggered by the moist air advected from the warm Mediterranean Sea across the Himalaya. These cyclonic storms are characterised by an upper-level trough underlaid by a lower-level cyclonic circulation. It is embedded in the mid-latitude subtropical westerly jet stream travelling at a speed of up to 43 km/h (Dimri et al., 2016), thereby bringing winter rain to low-lying areas and snow in the mountains. On an average, about 4–6 WDs occur each month over an extended winter period from November to March, with each formation varying in amount and distribution pattern, and decaying in a few days (a lifecycle of three-to-four days). The moisture-laden, mid-latitude upper-tropospheric troughs bring winter precipitation over the Himalayas due to the orographic land–atmosphere interactions (Dimri et al., 2015) spawning convective instabilities, which are possibly amplified by the colder continental air aloft. The WDs have a major influence on the meteorological conditions of the Indian Subcontinent. The resulting weather system is critical for the replenishment of glaciers, permafrost response and regulation, as well as for groundwater stores, and is also associated with weather extremes like cold waves, winter storms, and flash floods.

The changing synoptic regimes over the Indian Subcontinent and the Tibetan Plateau conducive to enhanced lifting and moisture pooling could signal an increase in the potential for concurrent weather systems to interact over the Himalayan region in the future. There needs to be abundant moisture and deep convection that transport water vapor to high tropospheric levels and strong wind current, combined with orographic uplift, to transport the water vapour in the moisture plume along the southern slopes of the Himalayan range. These synoptic and mesoscale patterns create the potential for extreme snowfall events. Not much scientific work has been done to explore the initialisation and evolution of local heavy snowfalls over the Himalaya with focus on the synoptic-scale vapor thermodynamic and associated mesoscale mechanism giving important information about atmospheric signatures portending an extreme event. Weather extremes are frequent in the Himalayas, however events of great consequences like the winter snowfall of 2021-22 were rare but had occurred in the past: In the winter of 1990/1991, abnormally heavy snowfall between 1-3 January 1991 triggered an avalanche that killed 17 climbers in south-eastern Tibet. The cause of the heavy snowfall was determined as cyclonic WD propagating as a topographic Rossby wave (TRW) along the southern periphery of the Tibetan Plateau and the Himalayan range (Hara et al., 2004);[ii] A once-in-50-year post-monsoon storm on 9–10 November 1995 spawned a snowstorm in the Khumbu region of Nepal that triggered numerous avalanches; Lian Liu et al. (2021)[iii] inferred from their study using reanalysis data that an abundance of water vapour and the strong orographic uplift of the Himalayas, as well as cold downslope wind convergence, triggered a heavy snowfall event over the Tibetan Plateau in March 2017; In their assessment of the October 2014 snowstorm over the Nepal Annapurna Himalaya, Wang et al. (2015)[iv] argued that such events were the result of a one-off oddity in the coupling of a tropical cyclone with a deepening upper-air trough in a historic tropical–extratropical interaction further accentuated by orographic uplift. They also posited the southward shift of the South Asia jet due to radiative forcing of anthropogenic origin (GHG and aerosols) could wreak havoc on the natural causes of storm initiation and evolution. These past events bore the same synoptic signature of extreme atmospheric dynamics of cold-air outbreaks, moisture convergence, convective instability, and upper jet modulation.

The atmospheric feedback from heavy winter snowfall over the Himalaya and the Tibetan Plateau finds expression in the arrival and strength of the subsequent summer monsoon circulation (Dash et al., 2005; Dey et al., 1985). Hunt et al. (2018) found a significant relation between the position of the subtropical westerly jet stream (SWJ) and the frequency of WDs that increases with the southward shift of the jet suggestive of the predictability of extreme winter precipitations over the Himalaya. Lang and Barros (2004) in their study of observational and reanalysis data from central

Nepal found that snow days were associated with increased cyclonic flow and lower geopotential heights, and an enhanced westerly flow over the north-west Himalayan region. The days of snowfall were also associated with lower temperature, higher relative humidity, and the upward vertical motion of air mass over the western and central ranges. They concluded that heavy snowfall in the central Himalaya is unambiguously related to the presence of orographically captured depressions in the notch formed by the mountain ranges. Hara et al. (2004) noted that the mesoscale cyclonic features of WDs agree well with the theoretical solution of TRW in a stratified quasi-geostrophic fluid.

Temperature determines the type of precipitation in a region with monsoon-dominated snowfall and snowmelt season. Jennings et al. (2018) mapped the air temperature thresholds for rain-snow phase partitioning at an average of 1°C ranging from -0.4 to 2.4°C in the Northern Hemisphere. The spatial variability in the threshold temperature suggested that the snowfall reduction is not expected to be uniform across the region. These findings are consistent with observed decline in snowfall frequency, snow amount and extent in recent decades over the Himalayas and the Tibetan plateau (Mohammed & Thapa, 2022). With the climate trending towards a warmer future, the cryospheric zone is expected to shrink with huge consequences in water resource availability for both ecosystems and mankind as meltwater contribution decreases in groundwater and surface flow. Without seasonal snowfall for replenishment, the water reserve in the snow and ice masses could decline over time. Snowfalls like this event being studied are rare but not unique to our mountain regions (Cannon et al., 2016; Dimri et al., 2015; Hunt et al., 2018; Wang et al., 2015), but whether such anomalous weather events are due to anthropogenically forced climate change or natural climate variability is yet to be resolved conclusively. Our climate in the recent past has seen unprecedented changes impelling us along an unsettling present that foreshadow even more uncertain future. It is possible that we may find some answers in the latest Coupled Model Intercomparison Project (CMIP) model projections considering the incorporation of recent advances in model physics, better representation of socio-economic pathways and the computational resources (Palazzi et al. 2015 , Almazroui et al. 2019).

Event attribution studies based on observed cases were cited in several past studies as imperative to determine the likelihood of observed extremes and detect whether extraordinary snowfall events are expression of natural climate variability or anthropogenic climate change. The meteorological situation and weather contexts of this snowfall event is best demonstrated with a case study over Bhutan in relating the synoptic-scale dynamics and thermodynamics of WDs with actual observations and experiences on the ground, specifically highlighting the rare occurrence of snowfall at lower elevations (~1000 masl) since 1958. Substantial knowledge has been accumulated and synthesized in the successive reviews of scientific literature (Demri et al., 2015; Mooley, 1957; Sharma & Subramaniam, 1983; Lang and Barros, 2004; Roy & Roy Bhowmik, 2005; Kotal et al., 2014) to confirm that orographic forcing is the dominant factor in generating precipitation along the foothills of the Himalayan range, especially in the presence of low-level flow that feed convection with moisture piped from the Bay of Bengal. Despite such effort, understanding the spatial and temporal scales of the dynamical interactions and physical processes even within the troposphere is still a massive challenge. Without a large dataset of WDs, it is challenging to make any assertions about their gross structure or interaction with the large-scale systems other than by theoretical or case-study analysis to understand better the evolution, spatial distribution and seasonality of WDs. Despite the complicated orography and fairly small spatial scale of WDs, they are typically well represented in reanalysis products (Mohanty et al., 1999). They are also shown to exhibit notable surface synoptic conditions like the fall in temperature and pressure (Dimri, 2004). With a simple goal to ascertain the key diagnostic features and inform future prognosis, this study only provides a preliminary assessment of the 2021-22 winter season snowstorm integrating observations, reanalysis and model data freely shared in accessible format requiring minimal preparatory and processing time and resource.

Post-mortem analysis of this rare Bhutan winter snowfall is expected to yield critical information about the atmospheric signatures in detecting extreme events well in advance. However, not all events carrying some semblance of these signatures guarantee extreme event occurrence. Hunt et al. (2018) tracked over 3000 WDs events between March 1979 and June 2013 in the SWJ with a frequency of 6-7 occurrences per month, and the strong ones generally impacting the Himalayas beginning of February. Heavy winter snowfall is not just related to tropical-extratropical systems interaction under orographic influence, but also to storm intensity and jet position. Our introduction and limited review of past works most relevant to this study in this section provides the context for this paper. We present the outline of the input data sources and methods used in the diagnostic study in explaining the extraordinary snowfall event centered on the 4th February 2022 in section 2. The results of our analyses are discussed in section 3 covering the exploration of meteorological fields that describe event initiation, evolution and decay. We also look at the dynamical structure and synoptic features of the weather system in relation to the snow cover and depth on the ground. The observed footprint of the event is then assessed against the propagation of cyclonic trough with the flow of SWJ stream along the Himalayan range. Next, we search for event analogues from the past and in the future using model simulations to detect any causal fingerprint of anthropogenic forcing attributable to climate change, or whether the event is just another anomalous manifestation of natural climate variability. Finally, we delve into identifying dominant atmospheric circulation patterns and processes as sources for predictability of similar events in the future; and how warming climate may shift the SWJ track and the baroclinicity of the WDs. We conclude the discussion in section 4, with the prospect of improving the predictability of winter snowstorms based on the telling characteristics of upper air variables and synoptics of local scale features associated with similar events in the future.

Summary of the first snow event of February 2022 in Bhutan

A particularly heavy spring snowfall occurred over a large part of Bhutan in the first week of February 2022. The intensity of this snowfall event was variable, from light snow in some north-eastern parts to heavy snow seen in the west and north-west districts of Bhutan. Many places reported snowfalls for the first time in more than 60 years, and few that never experienced in a life time nor in the recorded history of the country. The synoptic scale conditions associated with the winter snowfall event are not overly unusual and yet considered remarkable in delivering snow to places like Punakha valley well below climatological snowline elevation (~ 1200 masl). This is suggestive of the complicity in localized mesoscale perturbations at the interface of unstable air parcels with surface topography. There has been reported cases of vortex merger and jet-streak excitation in the events of tropical-extratropical interactions causing moisture advection and anomalous precipitation (Hunt et al. 2021), but these were mainly restricted to post-monsoon periods. The last decade has witnessed a conflation of theories and literature on the WDs that greatly improved our understanding of the winter weather system over the HKH region. These mid-to-upper troposphere cyclonic perturbations and mesoscale vortices are responsible for winter precipitation critical for agriculture, and also greatly feared as the harbinger of disasters (Rangachary and Bandyopadhyay 1987; Houze et al. 2017; Hunt et al. 2018c). But what triggered the unusual snowfall of winter 2021-22 turn out to be an intricate co-mingling, coincidental and rare juxtaposition of several atmospheric features fostering an ideal condition for such weather manifestation. We explored and analyzed a number of key variables and parameters as proxies for characterizing and quantifying the state and dynamics of the meteorology steering the event weather system.

At the regional level, this snow-belt was about 1500 km long and 123 km wide along the Himalayan range. Heavy snowfall moved to the eastern end of the Himalayas on February 6 but weakened to light snow on February 7. For February 1 to 7 the heavy snowfall moved from west to east along the mountain lateral axis, with maximum daily snow depth recorded at several observational sites on the ground in Nepal, Bhutan, Arunachal Pradesh as far as north western parts of Myanmar. To provide a monthly and seasonal context for the snow event study, we briefly provide an assessed account of anomalies in the meteorological variables relevant to the information and understanding we seek to uncover from this case analysis. The surface temperature in February 2022, and throughout DJFM winter season in the HKH region has generally been cooler than monthly average of the 1991-2020 reference period, associated with below-average precipitation along the north to north-west quadrants of the region; but wetter than reference period along the Himalayan belt and extending further south into Ganga plain and east into Hengduan mountains (Data: ERA5. Reference period: 1991-2020. Credit: C3S/ECMWF). The general pattern of anomalies described for February are also reflected in the cold and wet conditions for HKH winter season of DJFM, 2021-22.

The snowfall that arrived in the early morning of 4th February in Bhutan was unprecedented in more than six preceding decades bringing lots of snow in anomalously low elevations. Power generation spiked for the next 5-6 days in row in Bhutan bringing additional revenue in power export (Kuensel). However, the damage to primary sector was devastating as 100s of greenhouses for winter produces were damaged in Haa (snow-depth: 25-50cm), Paro (20-40 cm) and Trongsa (5-7cm) districts worth millions. Heavy snowfall accompanied by rain, hail and gusty wind impacted highlanders due to the loss of yaks to cold and hunger, and Merak in far east of the country received the heaviest snowfall since 1991. Tashi Yangtse got its first snow after almost a decade since the last. Punakha situated at 1242m elevation saw its first snowfall in more than 64 years (5 cm) since 1958. Dagana also got its first snow after 16 years, the last two being in 1990 and 2005 (5-7 cm). The number of locations (Gasa & Chukha: 50cm; Wangdue: 7cm; Thrumshingla: 63cm; Thimphu: 15-30cm; Dochula: 60cm) reporting unexpected snow clearly distinguished this event as a remarkable occurrence despite the mainstream notion of a warming world. As the herders and animals were stranded in isolated grazing ground, the fodder scarcity took a toll on their livelihood assets and productivity. Communication facilities broke down making it impossible for emergency search and rescue work to reach out to affected people and communities. Sub-tropical vegetations were devastated without the adaptive capacity to withstand cold and snowy weather conditions, and recovery from the shock and damage is likely going to take long and painful process.

Data and methodology

The objective of our present work is to diagnose our case study looking at the recent winter snow storms and snowfall events across the Himalayan region in general and investigate in detail its singularity over Bhutan at least in the last 65 years. A select list of dynamic atmospheric parameters was employed based on past study literature around the WDs, the concurrent heat and moisture advection in a dynamic atmosphere to explain the case study event.

The surface observational data were provided by the National Center for Hydrology and Meteorology (NCHM); the data were collected on a sub-daily and daily basis at the NCHM's manual and automatic weather stations. These stations had been selected considering an evenly spaced lateral and altitudinal distribution. In situ observations are augmented by calibrated satellite-derived observations, and hybrid precipitation products on sub-daily, near real-time basis, especially for upper air estimates for the key weather variables. As for the meteorological satellite data, they were accessed from various online sources. The Half-hourly Integrated Multi-satellitE Retrievals for GPM-Late (IMERGHHLv06[v]) provided precipitation estimates at 0.1 degrees using the IMERG algorithm (Huffman et al., 2014). IMERG is intended to inter-calibrate, merge, and interpolate satellite microwave precipitation estimates, together with microwave-calibrated infrared (IR) satellite estimates, as well as precipitation gauge analyses. Patel et al. (2022) in their evaluation of four precipitation products had found that GPM-IMERG was the least accurate in forcing a flood simulation study. This dataset was used here only as a complementary source of situational information to the other multi-source merging precipitation and ERA5 products. The Multi-Source Weighted-Ensemble Precipitation (MSWEP v2.1[vi]), released on 20 November 2017, is a fully global, historic precipitation dataset (1979–2016) with a 3-hourly temporal and 0.1° spatial resolution. It takes advantage of the complementary strengths of gauge-, satellite-, and reanalysis-based data to provide reliable precipitation estimates over the entire globe. The station observations, MSWEP and IMERG precipitation products were used solely for evaluation of the ERA5 reanalysis dataset in accurately capturing the pattern and phasing of snowfall over complex terrain. In the present context, maps of the daily snow cover over the region just before and after a snowfall event were extracted from the improved snow-cover data set published by Muhammad & Thapa (2020) readily accessible at https://rds.icimod.org/TemporalTIff?id=snow. The subset is only used for visual assessment of the extent of snow cover affected by the event to get a sense of its magnitude and corroborate other information sources.

The hourly ERA5 (Hersbach et al., 2018)[vii] reanalysis data sets of relevant atmospheric variables at appropriate pressure levels from 1979 to the time of the study, published on the Copernicus Climate Change Services-Climate Data Store (C3S-CDS),[viii] were used for the diagnostic analysis of the synoptic-scale flow and circulation. ERA5 provided the best estimate of the state of atmosphere through a blend of observations and retrospective, dynamical forecasts. This C3S-CDS subset used in the study is native ERA5 re-gridded to a regular latitude-longitude grid of 0.25 degrees, 37 vertical levels from the surface to 0.1 hPa, and updated with a latency of about five days. A Bhutan-focused comparative study evaluating the different precipitation products identified that the ERA5 reanalysis precipitation data corresponded better than others with station observations (Power, 2021)[ix], and thus was selected as an appropriate data set to investigate this winter snowfall event in Bhutan. The variables at play were the horizontal wind components, temperature, the specific snow-water content, humidity, divergence, relative and potential vorticity, vertical velocity, and geopotential height at five isobaric levels. The data used extend between 0000 GMT at hourly time-step from 1 to 7 February 2022 assuming that the weather system evolved between these dates. The data sets are available at: https://cds.climate.copernicus.eu/cdsapp#!/dataset/reanalysis-era5-pressure-levels?tab=form. The domain of study extends from 35° E to 110° E and from 15° N to 40° N.

There is now a general consensus among the scientific community that WDs are responsible for most of the winter precipitation in the Himalayan region, especially in the north-west. Winter snowfalls are, therefore, the consequences of WD perturbations further excited by mesoscale and local-scale atmospheric anomalies in the troposphere. Deciphering these not-so-obvious meteorological fingerprints is the key to improving forecast skills in anticipating similar events in the future well in advance so as to prepare and respond effectively. We specifically focused our analyses on the WDs because of the intimate connection between the phenomena and local weather prediction. One aspect known with certainty is the topographic influence that forces the orographic uplift to precipitate the moist air entrained in the WDs and propagated eastwards in the SWJ. Topography influences rainfall by locally disturbing the vertical structure of the atmosphere by acting as barriers and causing heat sources to rise or sink (Barros & Lettenmaier, 1994). The airflow over the topographic barriers also causes the rise of water-rich, warm air from lower elevations to higher ones, leading to condensation, cloud formation, and growth thereby controlling the triggering, length, and strength of high-elevation precipitation events (Bookhagen et al., 2005). The Himalayan winter weather is also forced by a variety of upper-tropospheric features that control the low-level baroclinicity and surface cyclonic perturbations. Identifying and investigating these features that led to the snowfall event of 4 February is of major importance in forecasting similar events in the future. For these reasons, the vortical perturbations embedded in the mid-latitude westerlies are often theorized as topographic Rossby wave (TRW) due to vertical oscillation triggered by ascending flow pattern along the southern Himalayan slopes (Hara et al., 2004).

A frequent used approach to assess extratropical cyclonic circulation is to use statistical criteria to tease out atmospheric precursors foreshadowing the occurrence and position of a cyclonic system, combined with feature tracking in gridded reanalysis products (Lakkis et al., 2019). Hoskins et al. (1985) elucidated that the analysis of potential vorticity was an important diagnostic tool to examine and explain the atmospheric mechanism and dynamical aspects of extratropical cyclogenesis. We used the geopotential height, vorticity, and other synoptic fields/features to analyse the near-surface and upper-air co-evolution of temperature, pressure, and moisture patterns to frame the remarkable snowfall event in the context of the prevailing atmospheric dynamical processes and structure. As mentioned earlier, the ERA5 hourly data on pressure levels were used to diagnose and analyse the initiation and evolution of this exceptional snowfall. The snow-related variables were obtained from ERA5-Land, which is a rerun of the land component of the ERA5 climate reanalysis, forced by meteorological fields from ERA5. Synoptic system analysis of the ERA5 family of datasets covered the location of SWJ stream in the westerly flow, detection and evolution of extratropical cyclonic vortices, geopotential orography, flow and thermal dynamics and vector wind fields, and moisture upstream and downstream of the WDs. We also collected and compiled observations from daily in-situ stations across the Himalayas, and multi-source merged precipitation datasets from global-scale producing centres, collocated with the eventful snowstorm track of 1-7 February, 2022, and coinciding with the synoptic scale process representations.

Study area

The domain of the study extended from 35° E to 110° E and from 15° N to 40° N. The outer domain (No.1) was interposed on the area covered by major mountain ranges, and the inner domain (No.2) was nested as a shifting window tracking focus on the passage of the atmospheric features responsible for the snowfall event centered on 4 February 2022 over Bhutan. Figure 1 shows the location and extent of the study area.

Figure 1. Location map of the extended High Asia mountain ranges, including the nested sub-region bounding the focal area of the case study, and where extensive analysis of the atmospheric structure and processes is concentrated. Point locations are for places where snow is reported and observed color-coded into five depth classes (cm) wherever measurement is available (snow depth data from national weather services supplemented with information from mainstream and social media reports). Inset: Bhutan map zoomed out to its location on the regional map.

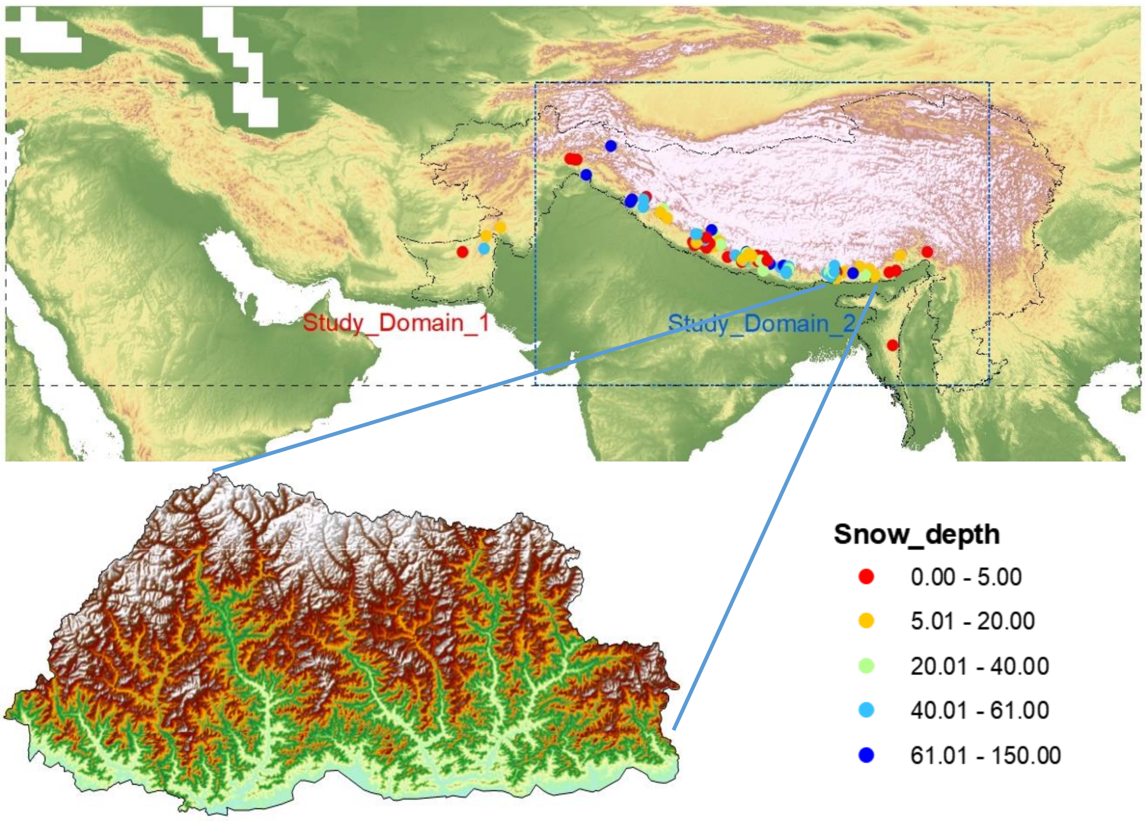

Results and discussion

The bulk of our analysis was based on the hypothesis that WDs had an important role in causing the uncharacteristic snowfall over Bhutan, occurring far below the traditional snowline into subtropical locations like Punakha and Wangdue that had never experienced snowfall since the last snowfall observed in 1958. This case study is focused on drawing the interest and attention of decision makers and socioeconomic operatives who are not only concerned about the adverse impacts but also are exploring the scope of opportunities that such events may present, especially in agriculture and water resource management. This study does not attempt to compare the 2021–22 winter event's snow depth or extent with other notable events from the past, but essentially provides a scientific explanation as to why the snowfall penetrated deep into the low-lying areas where snowfall was unheard of in living memories. The purpose and motivation behind this inquiry is therefore to: elucidate the lived experience of the unsuspecting general public; uncover new insights into weather-forecasting operations; inspire innovations in public weather service practices and procedures to provide reliable and accurate information in support of decision making; and finally, to stimulate resilience and adaptation in ecological, societal, and economic systems while providing a context for future studies.

a - A synoptic evolution

In the study, synoptic charts of geopotential heights at constant pressure levels were used to identify the weather systems of mid-latitude cyclonic WDs, the tropospheric SWJ stream in the westerly flow, the pressure trough and ridges, and surface orography. The synoptic situation at 200 and 300 hPa was particularly interesting as the SWJ moved from north-west India straddling the high Himalayan ridgeline towards Bhutan. In order to investigate the role of circulations in the initialisation and evolution of the heavy snow event, we conducted a composite analysis of the circulation pattern at 200- and 300-hPa levels before and after this snow event, as shown in Figure 2 (A and B respectively). These pressure levels were used to locate the SWJ stream within the westerly flow in the upper troposphere. Further, the zonal, meridional, and vertical wind components were assessed to detect and track the genesis and lysis of the WDs over their passage eastward. The wind was the strongest in the jet core that sat south of the WD centres and its direction was almost parallel to the height contours. Over the duration of the pre-event period, the wind direction was near zonal with maximum speed in excess of 100 m/s located slightly north of the west-central Asia and entering the South Asian region from the north-west and heading towards the south-east. Beyond the trough over the central Himalayas, the westerly jet gathered speed before it exited to the south-east of the Tibetan Plateau. The mid-latitude pressure ridge had weakened due to the reduced Pole-to-Equator temperature gradient, thereby causing the SWJ to meander southward in an omega-shaped blocking. The condition gave rise to cold-air outbreaks from the accelerated intrusion of the polar wind southward which was further supported by the waviness of the jet stream. In a climate change or global warming context, this situation is a paradox in attribution since polar amplification portending winter weather extremes is intuitively inconsistent with reduced frequency of winter snowfalls as rising temperature exceeds phase-partitioning threshold. To present a clearer picture of the prevailing situation, we elaborated on the results by separating the atmospheric processes around two broad tropospheric levels.

b - The upper-tropospheric situation

The SWJ has a maximum speed at around 200 hPa (Fig. 2), as reported in other works and synthesised in several reviews of the WDs cited above. The SWJ is usually not detectable at 300-hPa level in its contiguous structure, but the piped westerly flow concentration was very much evident during this event shifting slightly northward to its position at 200-hPa level. The closer the orographic contours were to each other, the faster the wind speed was, suggesting a steep temperature gradient between the cooler air mass in the trough and the warmer mass in the pressure ridge. The short-wave disturbances also likely affected the wind speed as varying isobaric heights representing spatially different geopotential energy could modify the wind pattern and the resulting weather system. Wind speed generally in excess of 130 km/h were used to examine the position and meander of the jet core, and thus forming strong trough upstream of the positions pummelled by heavy snowfall commencing around 0300 Z and continuing near 2300 Z of 4th February. Although not captured within the study domain, there was clearly no evidence of a split in the westerly jet stream but deflected in its entirety south-east of the Pamir knot that explained the rapid passage of cyclonic perturbations across the southern slopes of the Himalayan range in a matter of 2-3 days. This unusual behaviour in the westerly flow bore the signature of an exceptionally strong, negatively tilted trough with cold-air incursion further south, triggering a strong cyclonic circulation north of the jet stream. This led to the development of short-wave vortices that were associated with extreme precipitation as we see later in a composite analysis of the lower-tropospheric levels in tandem with the moisture advection from the Arabian Sea. The relative vorticity (not shown) is generally higher than 33 x $10^{-5}s^{-1}$ in the cyclonic cells and along the trough axis at 200 hPa level associated with increasing baroclinicity and pronounced frontal surface low located over north-west Bhutan and moving eastward along its northern frontier.

Figure 2. ERA5 fields of geopotential height and wind vector on 200 (A) and 300 (B) hPa isobaric surface centred at the time of peak intensity of snowfall on 4 February at 06z (12 noon, BST). The dash-blue line follows the approximate position of SWJ within a segment of westerly wind over the study region. The position of Bhutan indicated within the yellow box, and the approximate location of Pamir knot within the blue ovoid area.

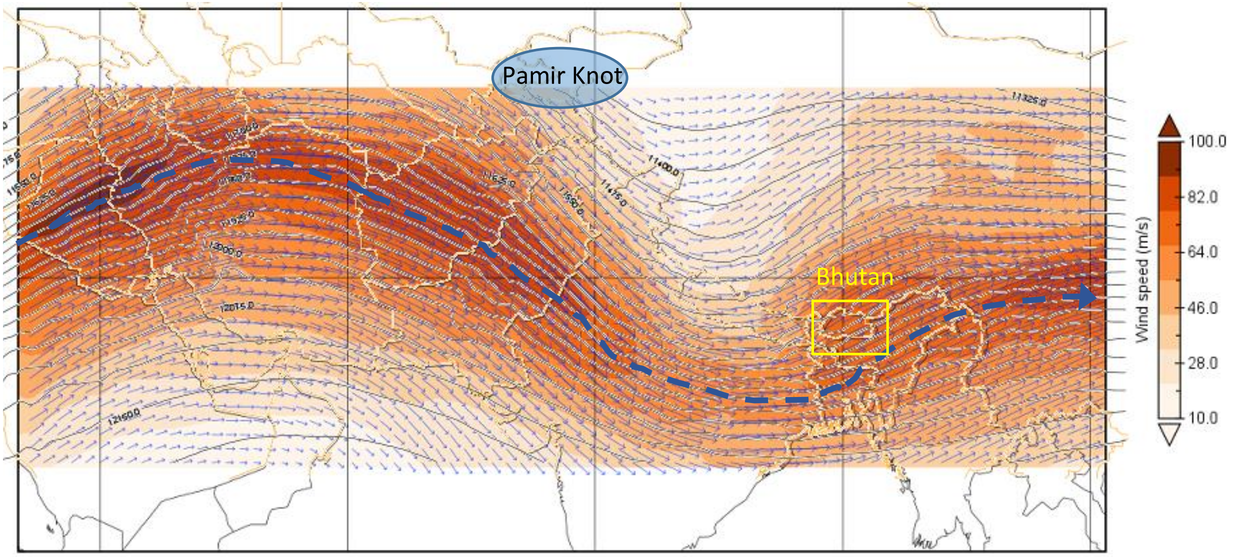

A. 200 hPa level wind vector overlaid on geopotential height on 4 Feb 2022 at 0600 Z corresponding to the peak time of snowfall. SWJ stream central meander denoted by dashed blue line.

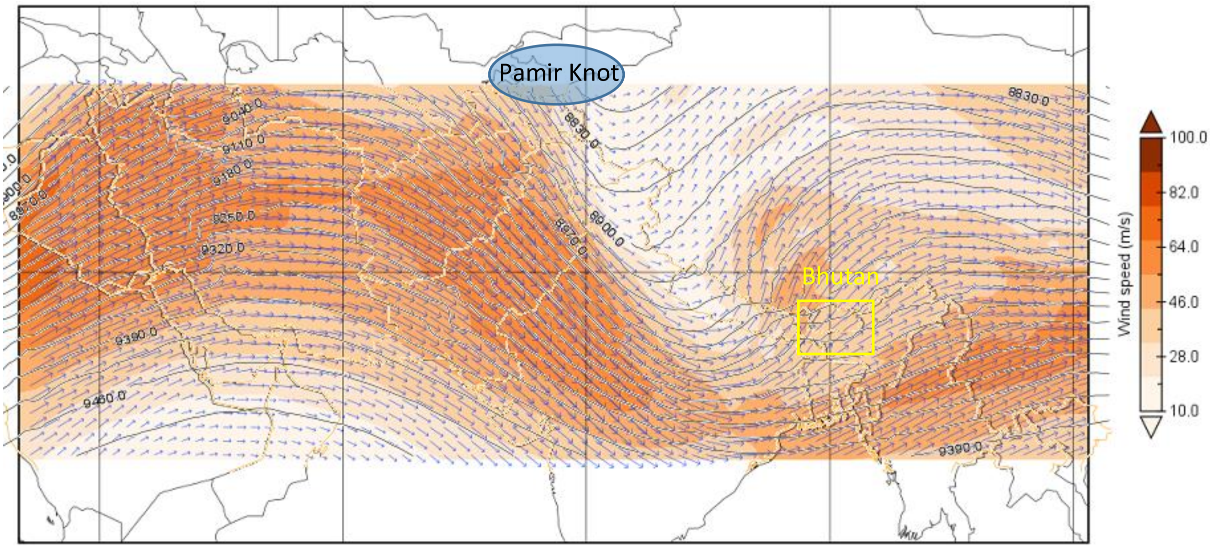

B. 300 hPa level wind vector overlaid on geopotential height on 4 Feb 2022 at 0600 Z corresponding to the peak time of snowfall.

In order to investigate the role of the upper jet in this severe snowfall event, the horizontal current and wind speed at 200 hPa were investigated (Fig. 3). The low-pressure trough within the synoptic wave propagated eastward from its position six hours before snowfall, peaking at around 06:00Z, and moving further east six hours later. The transient eddies associated with the synoptic disturbance were conspicuous in the height contours as depicted by the shortwaves embedded within the ascending branch of the jet meander (indicated by blue lines in Figure 3). The zonal wind flowing parallel to the latitude, usually bounded by the positive and negative tilted trough, tended to weaken behind the WD eddies and strengthen ahead of them. The places where the height contours are closely packed indicate steeper temperature and thus are associated with faster wind speed. Although not specifically investigated at this level but diagnosed further at the lower tropospheric level (500, 700, and 850 hPa), the non-linear coupling of WD and the SWJ stream exhibited a strong ascent ahead of the WD, which was matched by a similar descent behind it. Similarly, an expanded area of flow divergence sat ahead of the WD low-pressure troughs, as mirrored by the equivalent flow convergence behind them. The westerly flow over a large-scale barrier ridge sitting over Iran resulted in a cyclonic flow pattern immediately east of the barrier, thereby creating a leeside trough, perhaps followed by alternating series of ridges and troughs downstream. Over the event-decay period, the SWJ moved further east with normal conditions prevailing over Bhutan in terms of speed and direction.

Figure 3. Evolution of SWJ stream in the westerly wind (A) and the approximate location of synoptic and α-mesoscale troughs (B) on the passage eastward over time where clouds develop and precipitation takes place along the ascending limb of the jet stream (“z”= 24-hour UTC as Zulu time).

A. Location of SWJ stream in the westerly

B. Geopotential trough (blue line) and ridge (red-dash line)

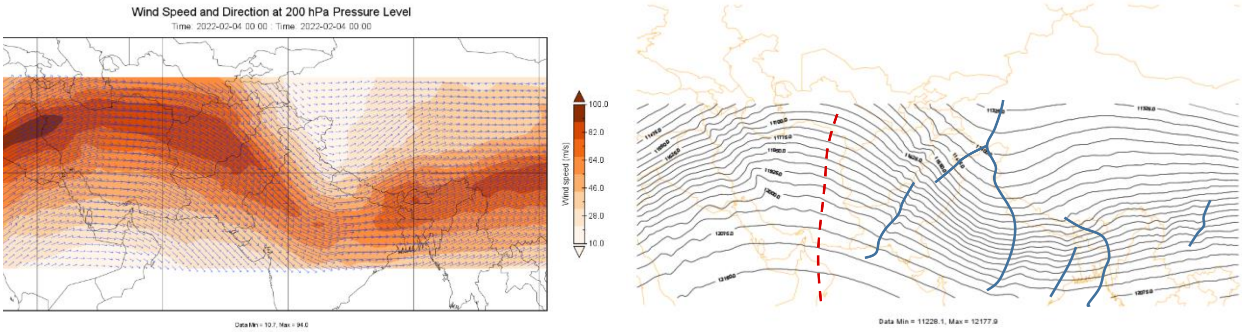

00: 00Z, 4 February 2022

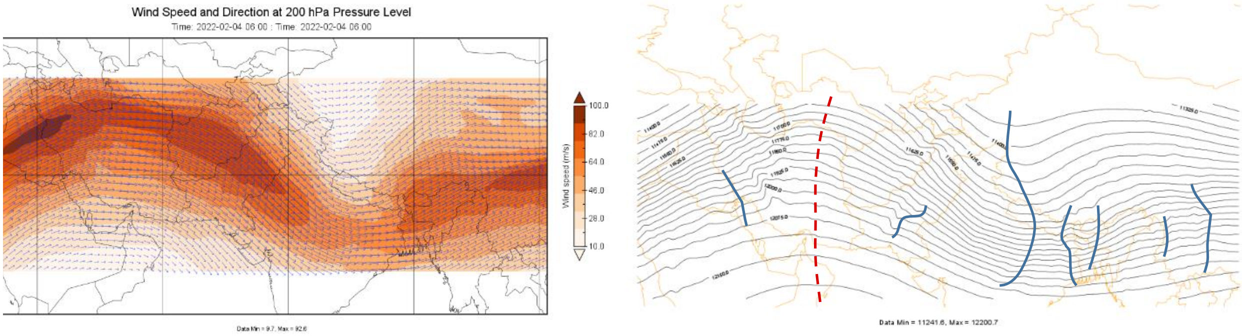

06:00Z, 4 February 2022

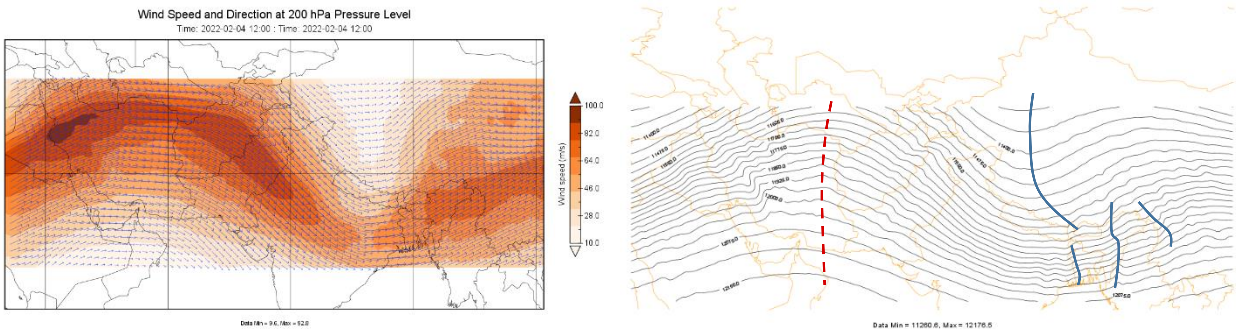

12:00Z, 4 February 2022

The day of 4 February represented the height of anomalies in several atmospheric variables which heralded a level of instability conducive for an atypical snowfall event. As evident from the analysis (Fig. 3 B), the length of a coherent, unbroken SWJ stream signals an impending event. The zonal wind (the ‘u’ component) was the strongest near 200 hPa and weakened behind the WD and strengthened ahead of it to a mean wind speed of above 40 m/s. The meridional wind comingled with the strong cyclonic circulation in the upper troposphere. The WD–SWJ coupling was non-linear with a strong ascent ahead of WD and a matching descent behind it, which was further accentuated by a strong upper divergence ahead of the perturbed weather system, as similarly mirrored by an equivalent convergence behind it.

c - The mid- and lower-tropospheric situation

The 500-hPa constant pressure level is important in synoptic meteorology for the analysis of weather patterns that we experience at the surface. This isobaric level is therefore often referred to as the ‘steering level’ as the mid-latitude westerly wind governs the region’s weather pattern and is generally detected within an elevation range of 4980–6000 masl, overlapping with the dominant

Himalayan topography. Here, the land-surface differential heating and the barrier effect of the physical orography were most pronounced which persuaded this study to consider it as central to the composite analysis of weather elements and so assess the structure and physics of the cyclonic perturbations associated with WD driving the weather conditions at the surface. At the regional scale, the analysis covered the full seven days from the naissance to the demise of the mid-tropospheric disturbances. The period was divided into event genesis (Day 1 to Day 2), event peaking (Day 3 to Day 5), and finally, event lysis (Day 6 to Day 7), as the weather system steadily stabilised over the event decay period of 6–7 February, and rapidly dissipated beyond the eastern end of the Himalayan range as the system drifted out of the study domain. The results are not reported here but provided as supplementary material to this report. Figure 4A partially shows the 500-hPa composite analysis only for 4 February, centred on the snow-event maxima from 00Z to 23:00Z. For clarity and to narrow down the focus on the key drivers of weather development, evolution, and decay, only snapshots of the synoptic features six hours before to 6 hours after the reported duration of the peak snowfall from 06:00–12:00Z of 4 February are presented. From 1–3 February, a low-pressure centre propagated from the west to east following the high Himalayan arc as a baroclinic upper-air trough. The positions of the alternating pressure ridges and troughs were obvious at the 500-hPa level and propagated eastward before the atmospheric conditions normalised by 7 February. At 00Z on 4 February, a cut-off low appeared over northern India forming a cold vortex poleward from the negatively tilted trough with an elongated band of cyclonic circulation extending south-eastward embedded in it. And within six hours, it aligned with the height contour and merged with the weakening mesoscale disturbances.

The evolution of the vorticity field in the mid- and lower troposphere was investigated in terms of its isobaric distribution at 500- and 850-hPa levels. The relative vorticity at 500 hPa with the centre of maximum values appeared to follow the tilted synoptic trough and the cyclonic cells that coincided with strong ascending/descending motion and the respective vorticity advection at the peak of the event. Thereafter, the value of positive vorticity decreased gradually to reach its smallest area and lowest values by 6 February as the event subsided over Bhutan. Then a quasi-stationary synoptic-to-mesoscale wave was evident along the trajectory of the vertical perturbations. As the atmospheric system advanced towards event culmination, several features manifested anomalous developments in terms of vorticity advection, ascending motion, deepening of upper trough, and vortical intensification. The analysis in this study of the isobaric relative vorticity was designed to assess the significance of upper-level dynamics in the induction of cyclonic circulation leading up to the realisation of the snow event. It is evident that the areas of highest vorticity coincided with the pressure trough and cyclonic cells associated with the upward motion over the rising terrain and sank on the other side with negative vorticity. The result was an alternating series of positive (negative) vorticity producing unsettled (fair) weather at lower levels respectively. The cyclonic disturbances developed almost exclusively between the trough and the downstream ridge where the greatest rate of increase in vorticity was found, as well as towards the north of the SWJ core with its dominant shear component. This implies convergent flow at the lower level, possibly leading to unsettled weather and precipitation. On the other hand, the upstream of the trough saw the greatest rate of decrease in vorticity where the air sank and diverged at the lower level, leading to fair weather. We verified with ground observations that at 06:00Z, these areas of greatest rate of increase in vorticity lying directly above surface locations like Punakha-Wangdi Valley received its first snow in more than 64 years, as recalled by elderly locals.

The densely packed vorticity isolines indicate a high gradient leading to enhanced vorticity advection, and a discontinuous snowbelt was reported from discrete locations in Nepal and the Indian states of Sikkim and Arunachal Pradesh. In this study, the relative vorticity parameter proved useful in the detection and evolution of the WDs embedded in the SWJ stream.

The upper-level dynamics of the synoptic features were significant in the investigation of atmospheric instabilities in this case study. Figure 4 B shows the vertical profile of vorticity and vertical velocity along the proximal latitude and longitude belts roughly intersecting close to the locations in Punakha which experienced its rare snowfall. In the same period of the study centred on the time-slice between 00Z and 18Z of 4 February, the alternating positive and negative vorticity cells were found to be dynamically arrayed along the snowbelt spanning the entire length of the Himalayan range. The cells of maximum relative vorticity gradually moved eastward undergoing rapid changes in position and magnitude, intensifying and dampening in their passage and instigating episodic snowfalls in unexpected places as far as north-east Myanmar and finally dissipating by 7 February. Analyses at other steering isobaric levels point to dynamical evolution of the atmospheric structure, circulation pattern and orientation, moisture advection, convection, and orographic lift characteristic of meteorological features conducive for extreme weather events. The surface low-pressure system deepened with a significant north-westward tilt with height, indicating a strong baroclinic environment. The maximum value of the relative vorticity was above $4.55 \times 10^{-4}\ s^{-1}$ at 500 hPa taken as a zonal average of the study domain, and a meridional locus located over the 28-N latitude. Poleward up to 26-N latitude was generally dominated by negative vorticity as expected since this area lies equator-ward of the SWJ stream. From 06:00Z on 1 February to 06:00Z on 7 February, the positive/negative vorticity advections were centred in the 500/700-hPa isobaric levels. Interestingly, the positive vorticity oscillated in its ascent pattern between 600–300-hPa levels nearly every two days before being completely cut off from the system at the end of the study period on 7 February. Near the surface, places in and around Punakha by then would have experienced relatively fair and calm weather due to the weak anticyclonic condition prevailing near the surface in the study-time window. In the mid-troposphere, vertical motions, over time, tended to lead the passage of vorticity eastward, peaking at 2.34 Pa s^{-1} at 16:00Z on 4 February for ascent and 1.9 Pa s^{-1} for descent at 22:00Z the next day (5 February) at 500 hPa, corresponding with the period of the heaviest snowfall and the onset of atmospheric stability. Just before the longest episode of this snowfall event, the relative vorticity weakened before the vertical ascending motion was sustained for the next 18 hours. The system became cut off at all isobaric levels within 24 hours after the main snowfall episode; however, the persistent vertical tilt with height implies that the system continued growing near barotropically. In the hours preceding this period, the vortical anomaly peaked at $3.35 \times 10^{-4} s^{-1}$, favouring convergence at low level for moisture transport from the Indian Ocean. The tilt increased as the trough weakened to cause the cyclonic strip to weaken and shift north of the westerly flow in its eastward passage out to 18Z. The alternating cyclonic and anticyclonic rotations over the eastern Himalaya represent the transient eddies associated with α-mesoscale disturbances and Rossby wave breaking that marked the exit region of the SWJ stream. These transverse short-waves perturbations characterize the uplift and lee-side descend over the topographic barriers that result in copious precipitation. Just hours before the event onset, the centres of the low entered over the north-western part of Bhutan and deepened to about 5400 geopotential metres (gpm). At 06:00Z on 4 February, another secondary trough centred at 5460 gpm was observed over Bhutan which rapidly collapsed into zonal instabilities over the next six to 12 hours before its slow passage further east.

Figure 4. Left-hand column shows the geopotential height (m) in black isoline and (relative) vorticity (spins per second) as contoured and shaded respectively at 500 hPa at 00z (a), 06z (b), 12z (c), and 18z (d) on 4 February 2022. Right-hand column shows the divergence as solid contour and convergence as dotted contour overlaid on the vertical velocity map (shaded) on 500 hPa at 00z (e), 06z (f), 12z (g), and 18z (h) on 4 February 2022

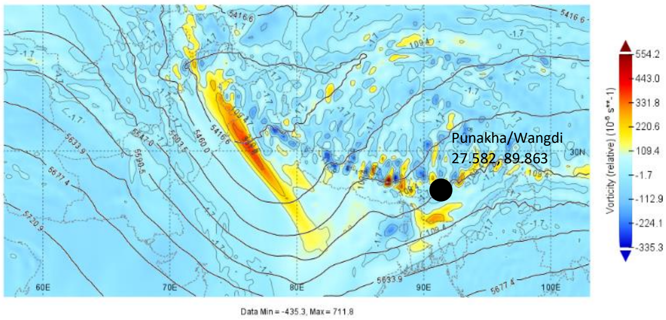

a. 00Z, 4 February, geopotential and vorticity

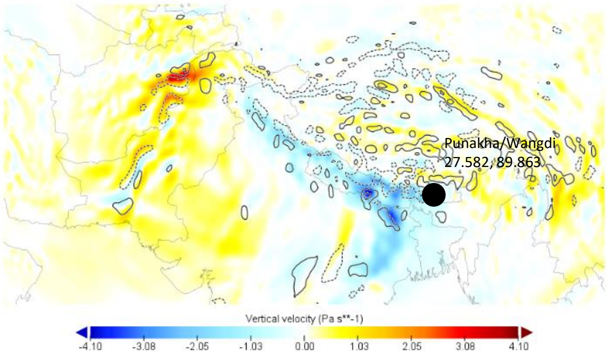

e. 00Z, 4 February, vertical velocity and divergence

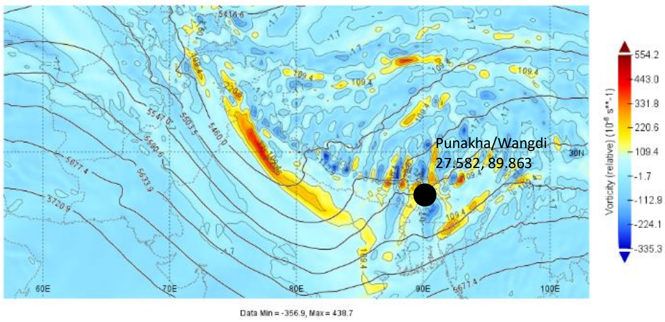

b. 06:00Z, 4 February, geopotential and vorticity

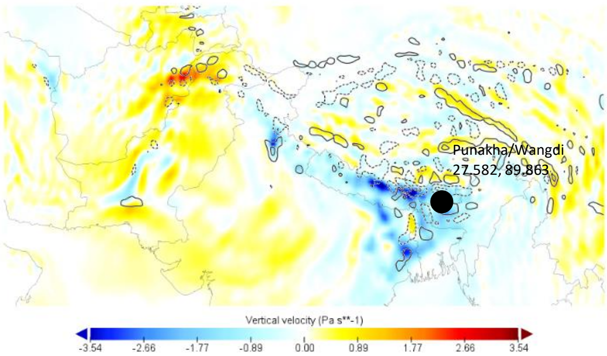

f. 06:00Z, 4 February, vertical velocity and divergence

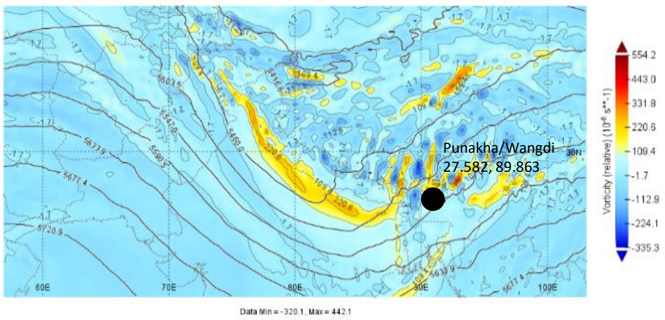

c. 12:00Z, 4 February, geopotential and vorticity

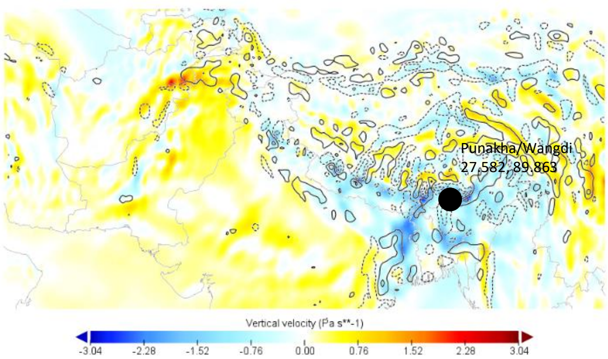

g. 12:00Z, 4 February, vertical velocity and divergence

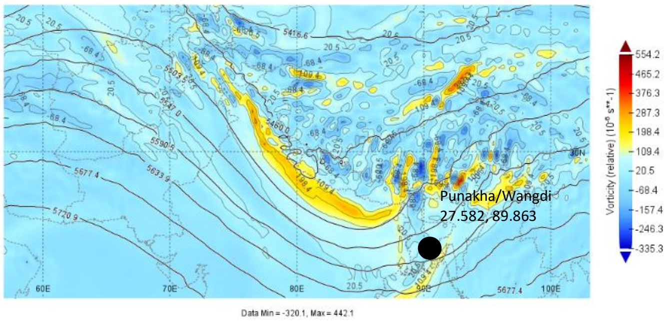

d. 18:00Z, 4 February, geopotential and vorticity

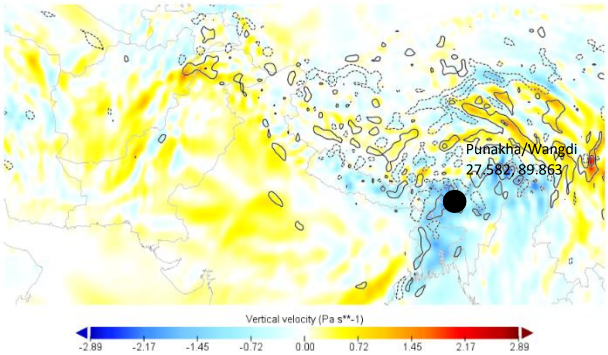

h. 18:00Z, 4 February, vertical velocity and divergence

The vertical velocity explains the vertical motion of the wind in generating geopotential differentials aloft and centres of high- and low-surface pressure areas. The alternating divergence and convergence over a short distance over Bhutan and adjacent regions was an important signal towards the impending snow event. As mapped in Figure 4 (right column), the higher vertical velocity of rising air is associated with divergent flow as the air mass spread out and carried forth in the geostrophic wind. In contrast, the sinking motion tends to coincide with both divergent and convergent flows and the dynamic link was not so obvious. This has implication in terms of the generation of vorticity and the strength of cyclonic circulation which dictated the kind of weather we observed on the ground. The water-vapour content of the air mass and the topographic roughness of the mountain terrain can exercise a significant effect on the level of diffluent and the speed of inflow and outflow from positions of divergence or convergence. The orographic uplift and convection due to the steep thermal gradient favored rapid vertical ascent up the mountain slope and the pressure ridge to force the atmospheric moisture to precipitate as snow under ideal thermal stratification. In addition, the tight coupling of upper divergence and lower convergence initiated a strong ascending motion of moist air mass to also precipitate as either snow or rain, depending on the thermal structure of the atmosphere. Conversely, upper convergence and lower-level divergence induced cold air to sink, warm, and evaporate to usher in a clear sky. The exit of this downward flow generated strong wind at the surface, thus initiating the cold wave that swamped most of the adjacent Indian plains. At 00Z, the ascending motion ahead of the pressure trough over the southern slopes of central Nepal opened up an exit for flow divergence at the 500hPa level and advected east in the westerly jet. The area of convergence sat over Sikkim and western Bhutan and shifted further east followed by a train of alternating vertical motions closely following the terrain profile. Moist air from the south merged with the rising air along the slope in amplifying the disturbance further creating a cyclonic situation along the south-west foothill of Bhutan and bringing snow over the mountains in the north. Therefore, positive vorticity advection, lower-level convergence, and upper-level divergence all operated in tandem to generate ascending motion and bringing snow to locations directly below the rising limb of the geopotential ridge shallowing off towards the east. Figure 5 portrays the interaction and evolution of the vertical motion with other dynamic features of the atmosphere in the vertical cross-section positioned over 27.25N latitude that closely aligned with the transverse snowbelt intersecting the places that reported record-setting snowfalls. It also depicted the co-evolution of the alternating composite vorticity-divergence field against the backdrop of vertically integrated zonal wind vector in reproducing the atmospheric disturbances that instigated the rare episodic snow. One prominent signature of such an event as this study found was not so much to do with scalar and integral values of the atmospheric elements or features, but with their rate of change and gradient across three-dimensional space–time context. These results were consistent with past findings that synoptic-scale wind system and the mesoscale transverse circulations are key to the prediction of all atmospheric elements and weather features.

Six hours before the major episode of the snow event that continued from 06:00–12:00Z on 4 February, a vertical column of convergent flow lay downstream of the area of maximum vorticity centred on the 85E longitude associated with a weak cyclonic ascend. At 06:00Z, the event intensified with convergence elongated from the 500-hPa level to a lower level and the ascending vertical velocity slightly increasing along with intensifying upstream vorticity. The divergent flow at the upper level got piped into the southward bend of the SWJ stream aloft and carried eastward in the westerly wind. The situation endured out to 18:00Z with sustained vorticity, but the vertical velocity slowed slightly although the vorticity of the air was conserved, and later developed another vortical column behind the active system located over 80-E longitude centred at 500-hPa level. Over the remaining part of the day, this new cell shifted slightly downward and east and likely initiated another episode of snow, while the prior snow-making system collapsed in place. Few upper-convergent entrances and lower-surface divergent exits started to form mainly on the east side of the study area. In general, the vertical motion component was weak compared to the depth of the westerly wind, and calm at the surface other than the isolated vortical cells.

Figure 5. Composite fields of relative vorticity, divergence, and vertically integrated horizontal wind vector on a vertical plane at 27.5-N latitude and zonally covering the whole west–east extent of the study area. Maps show the vertical profiles on 4 February (the day of the peak snow episode) at 00Z (a), 06:00Z (b), 12:00Z (c), 18:00Z (d), and 24:00Z (e).

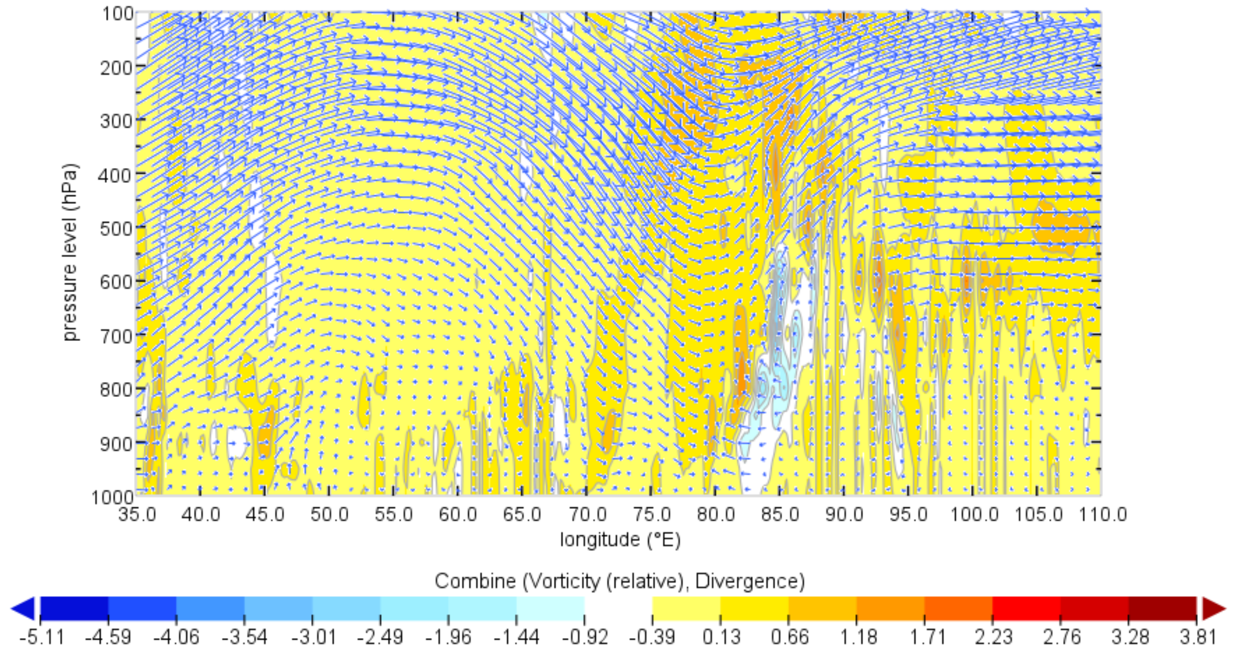

00Z, 4 February

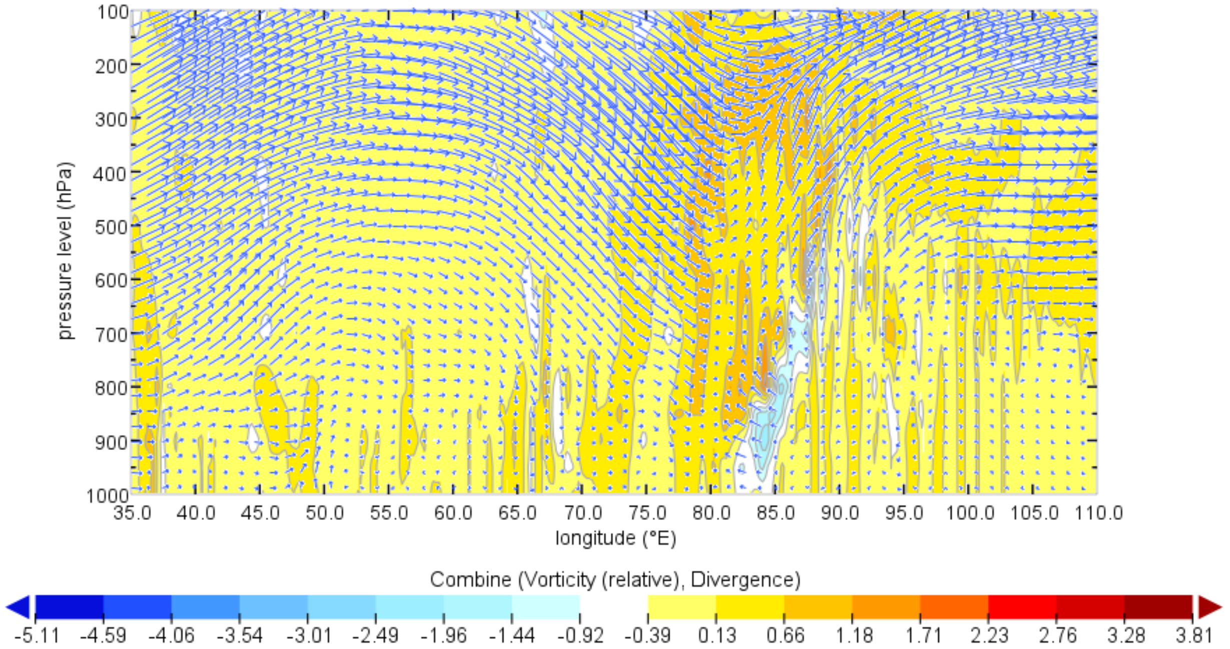

06:00Z, 4 February

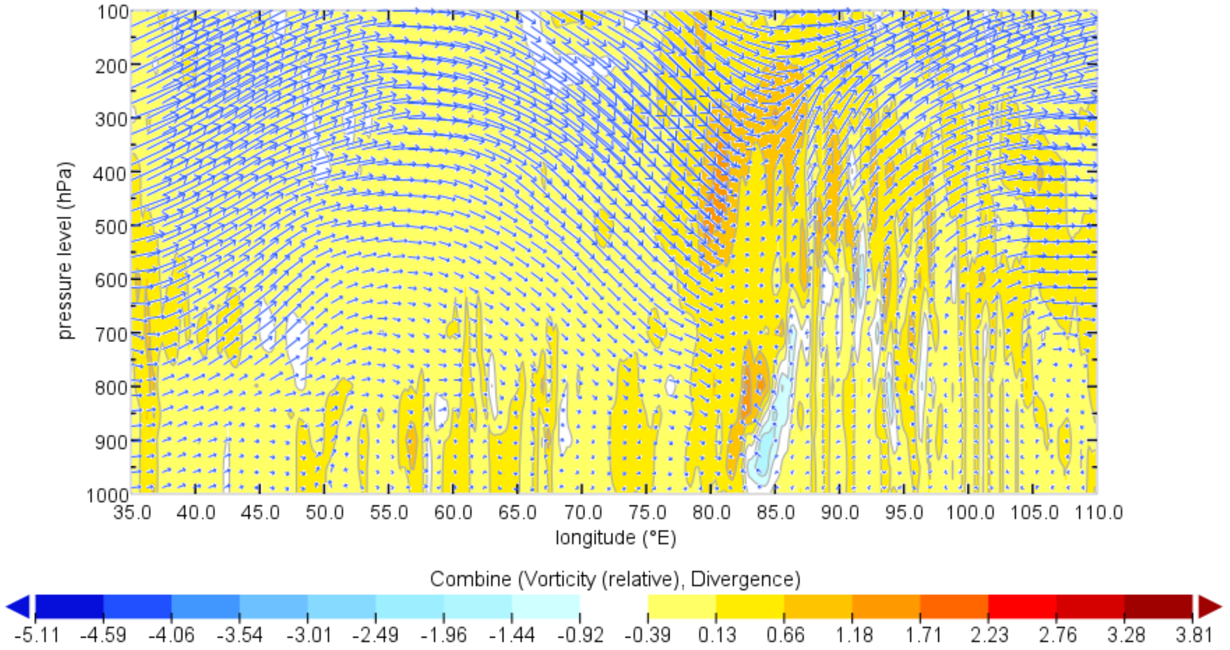

12:00Z

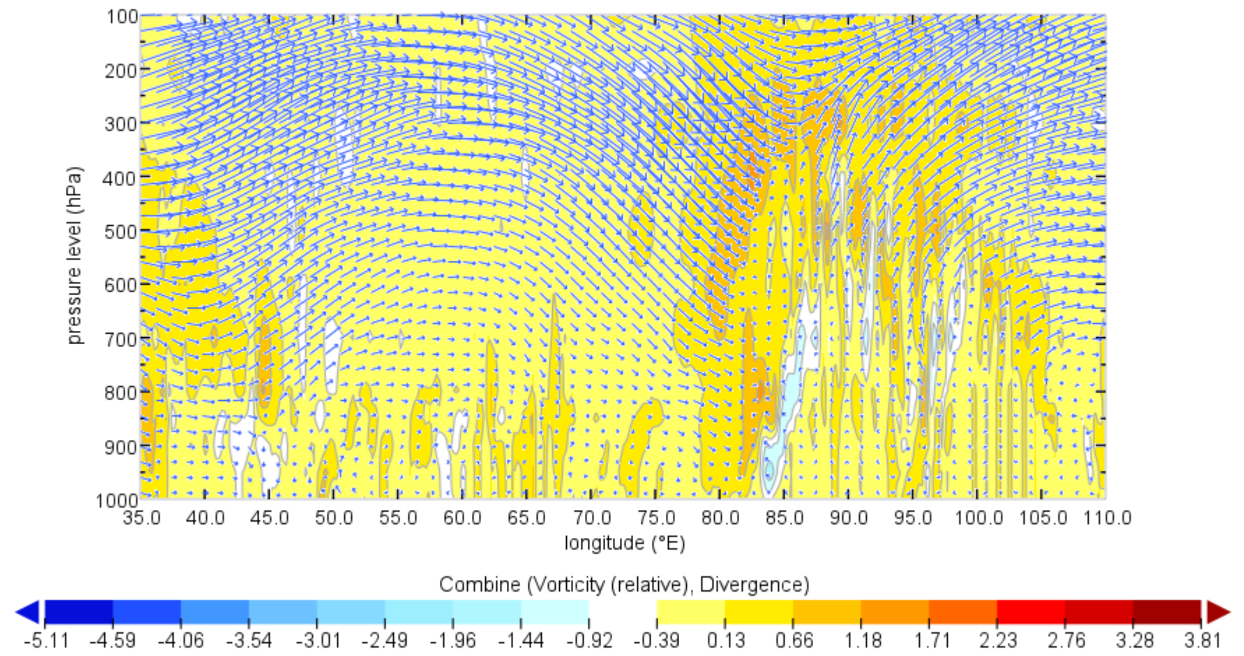

18:00Z

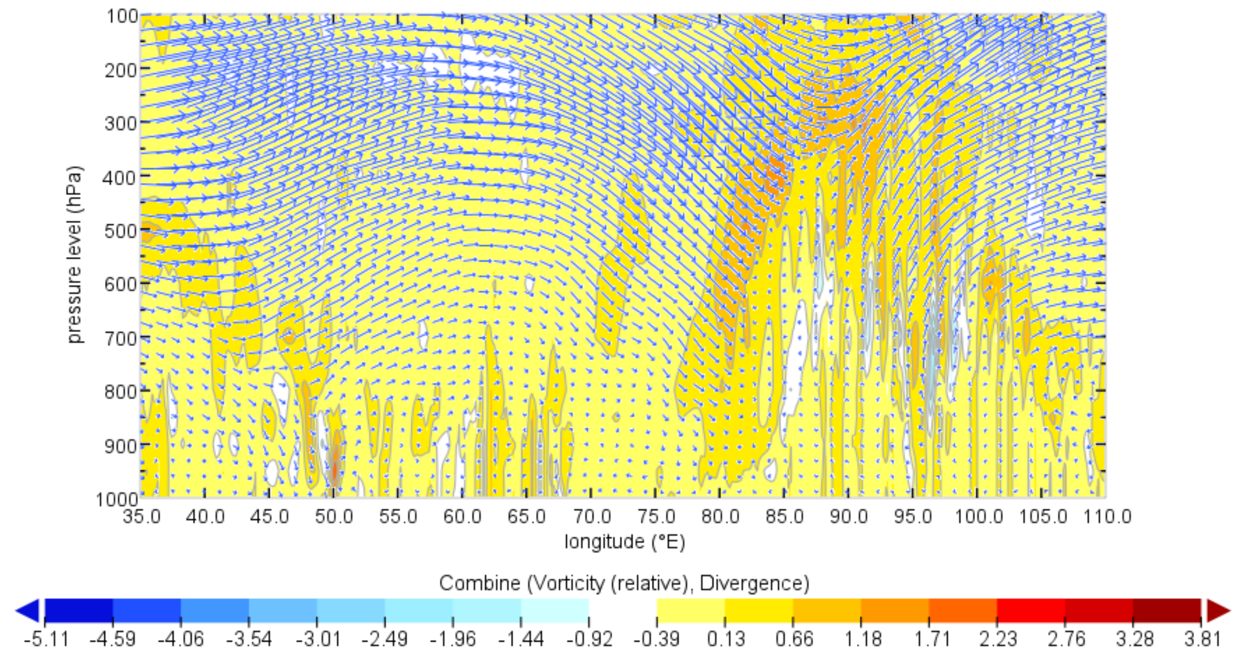

00Z, 5 February

In the days and weeks preceding the historic snowfall event over the Himalaya, the seed of WDs had been sown in the sea regions of the Mediterranean basin in the form of the extratropical storm Elpida in the last week of January 2022 (Reuters & CNN Weather, 2022)[x]. The higher-than-normal temperature in the Black Sea region provided additional heat and moisture to sustain the storm in the SWJ stream eastward to the Himalayan region. The hurricane-like atmospheric systems called 'Medicane' (Miglietta, 2019) were the early precursors of the WD that propagated eastward carried in the mid-latitude westerlies and the SWJ stream at its core. The baroclinic and diabatic processes to Medicane development was similar to the transient eddies (Rossby wave breaking) of the WDs. The baroclinic instability was expected to be less intensified by the diabatic processes, but this particular snow-making weather system was perturbed by a sizeable convection in the west and south-west of Bhutan from the warm, moist airstreams pulled in from the Indian Ocean to interact with the upper-level pressure trough over eastern Nepal, Sikkim, and the Bhutan Himalayas. There was abundant moisture piped in from the Mediterranean region embedded in the warm current of the SWJ stream. The amplification of the upper-level winds, the deepening of the WD trough, and the strengthening of the vorticity over the region in concert acted as a massive suction pump for moisture from the Bay of Bengal and the Indian Ocean in general. The moisture-laden air mass underwent an uplift from the frontal winds, the pressure gradient force, and the orographic lift, which cooled the moist air mass in its vertical ascent to form a cold cloud and ultimately precipitating to the ground as snow where the near-surface temperature was cold and deep enough to form ice crystals. The cold waves engulfing the plains south of the Himalayan range magnified the convective gradient with warm air above the land and ocean further south, forcing the warmer air to rise above the diverging cold-air mass southward. The moisture-laden air mass was advected in the convergent flow at the surface low-pressure centres upstream behind the cyclonic ascent of the jet stream and amplified by the topographic uplift to produce intense precipitation ahead of the baroclinic disturbance. Deep convection transported water vapour to the high tropospheric level. Moisture plume in the satellite images confirmed their zonal transport and phasing with the convective plume from the Bay of Bengal (not shown). The cold-air incursion from the north also created a frontal lift further amplified by the orographic ascent against the backdrop of strong meridional variation in temperature. Besides these interactions and exchanges, a diabatic process appeared to also play an important role in the causation of the event in relation to the geographic positioning and topographic characteristics of Bhutan.

For precipitation to occur and fall as snow on the ground, the atmosphere must contain sufficient water vapour and have a conducive vertical temperature profile. Figure 6 presents the vertical profiles of temperature (a); specific humidity (b); fractional cloud cover (c); specific cloud ice water content (d) as atmospheric quantities to determine where precipitation will or will not occur; and how water-phase partitioning is influenced by the thermal structure and the wind system. The vertical slices were made to intersect at the geographic coordinates closest to our case location in Punakha, considering the 0.25º resolution of the ERA5 reanalysis. Figure 6-A provides the cross-section through the 27.5-N latitude and Figure 6-B gives the cross-section through the 90-E longitude of the atmospheric elements in the tropospheric layer (1000–100 hPa). The spatial extent of this analytical sub-domain is confined between 20-40N latitude and 80-100E longitude, and at the crucial point in time (06z, 4 February) when the event snowfall reached maximum intensity; all to assess whether atmospheric conditions were conducive for anomalous snowfalls in least expected places.

The vertical cross-section along the east–west (27.5N) and north–south (90E) transects at 06:00Z on 4 February reveals quite interesting aspects of the meteorological fields that controlled the weather event culminating at the surface despite these charts representing only a single snapshot in time. The entire atmosphere was below freezing, down to 950 hPa, with a gradual rise eastward up to 850 hPa, but interposed with localised lows (Figure 6 A-a). The meridional structure of the temperature featured a dip at the 27.5-N position extending upward to at least 500 hPa. It’s likely that all areas higher than 1200 masl and west of 90E would have experienced below-freezing temperature, thus satisfying one critical condition for snowfall. The water-vapour mass measured by specific humidity showed substantial lower tropospheric moistness (2.6 – 5.2 x 10^{-3} kg kg^{**-1}), although the zone extending the Bhutan border indicated comparatively drier air at the surface; however, the vapour column aloft was deeper and thus held more moisture to precipitate. The meridional structure clearly captures the moisture cutoff at around 28N since the high Himalayan ridge blocked the available water vapour from moving further north, and the orographic and convective lift could carry it only as high as 450 hPa. This constituted a situation akin to a dry line with a west–east orientation perhaps following the highest Himalayan ridges that separate the wet southern slopes from the dry Tibetan Plateau. At that point in time, the cloud cover was complete from the ground to near the 200-hPa level, thus extending higher than the moist air layer and primarily feeding the snowfall (Figure 6-c). The lower-level clouds were generally confined to the south-western part of the analysis area corresponding with the centre of the intense convective precipitation, as explained later while dissecting the observational data. The meridional slices picked up the boundary between the warm, moist air mass and the cold dry air mass to the north. The band of cloud in the upper troposphere is associated with water-vapour advection in the westerly flow. The highest fractional cloud cover was centered around 400 hPa and was found to be decreasing above 300 hPa and below 500 hPa, consistent with an earlier study which observed that WDs exhibit maximum vorticity in this band of pressure levels (Hunt et al., 2018). The 200-hPa height marked the cloud top. The orographically generated cloudiness merged with the upper-level cloud and continued spreading north-east across the Tibetan Plateau, but the water vapour-content of any precipitable consequence was not detected beyond 35^{o}N. The centre of the maximum specific cloud-ice water content was located at 400 hPa, directly above the areas experiencing the intense snowfall. The north–south profile through 90E exposed the abrupt reduction in ice particles which once again explains the prevailing dryness north of the 28-N latitude. The optimal juxtaposition of wind, moisture, and temperature patterns over the Bhutan sector of the Himalayan range, and the dynamic interactions among other meteorological fields conducive for formation of ice particles, phase transition and aggregation all pointed to a probable signature for heavy and prolonged snowfall. The dendritic growth zone for snow production (-12 to -16^{o}C) was approximately located between 600 hPa and 550 hPa, overlapping with a band holding 1.3-2.6 x 10^{-3} kg kg^{**-1} of water vapour. The snow particles falling through the below-freezing cloud cover layer extended to the ground level (Punakha, roughly positioned around 850 hPa level), thereby ensuring crystal growth by accretion and precipitation as snow at the surface.

Figure 6. Vertical composites of upper-air meteorological fields over the Eastern Himalaya.

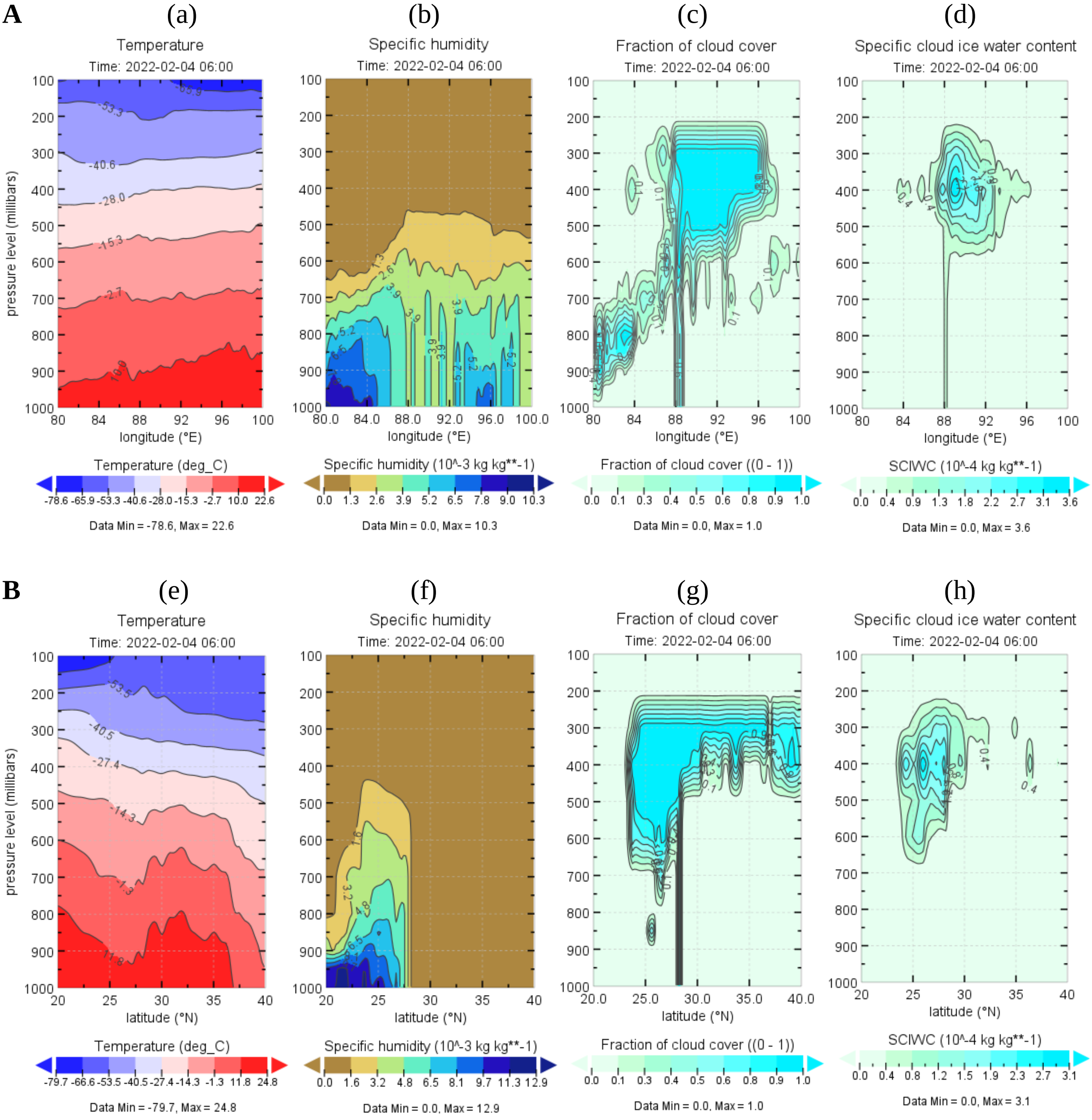

Finally, we analysed the elevational difference between the 1000-hPA and 500-hPA constant pressure levels to identify frontal activities and investigated the transition line in the precipitation-phase partitioning to expect rain or snow. The thickness value of 5400 meters height difference was taken as the traditional line to determine rain or snow, which was a good first guess, as it closely followed the surface freezing temperature (0°C). Figure 7-A describes the thickness isoline (blue) overlaid with surface pressure, precipitation, temperature, and wind vector in an attempt to summarise their composite expression in terms of the state of the surface weather at our particular time of interest (here we used the time of 06:00Z on 4 February throughout). The 5400-m thickness contour was checked against the corresponding 0-degree level (green line), which is the height above the surface where temperature passes from positive to negative at a specified time. The 5400-m thickness contour closely followed the 0°C isotherm (red contours) of the surface temperature in the mountain terrain. However, they diverged considerably in the northern plains of Pakistan and India with the 5400-m line shifting further south from the 0ºC isotherm before returning to its expected position through the lower Mustang Valley separating the Dhaulagiri and Annapurna ranges. It is not clear what caused this shift, but certainly the upstream pressure ridge aloft the region in the upper troposphere could structurally have influenced the expression and evolution of the lower atmospheric fields. A cold front located to the north-west penetrated deep into the adjacent plain unleashing a cold air outbreak engulfing the surrounding area for an extended period of time. Then the temperature plummeted to a near-record low, and in concert with the cold-air pool in the lee-side trough, which might explain the deviation seen in the thickness line. The 0º-level (green line) has a good fit with the 0ºC isotherm of the near surface 2m temperature although like the thickness contour it is expressed in height above land surface. All the snow episodes at that particular hour of the day were observed poleward from the transition lines. Heavy snowfalls were detected in Himachal, the Everest area, Sikkim, and in the north-western parts of Bhutan. Any precipitation occurring on the equator side of the lines would have fallen as rain, which was validated by media reports of unseasonal short-fused showers in north-west Bengal, the Terai region, and the eastern foothills. Figure 7-B shows the 850-hPa-level wind vector overlaid onto the surface isobars that recognisably depicts the depression over North India and a shallow low over south-east Bangladesh. Wind condition is gustiest where the 5400 isoline crosses the isobars at right angle and light wind decreasing to near still-air when aligned parallel to each other. Instances of such conditions prevailed over the ocean, near mountain and in positions of strong positive or negative divergence coupled with strong vertical motions. As expected, the wind was calm along the snowbelt, with its direction conspicuously opposite to the bearings observed at the upper tropospheric levels due to the vortical extensions (as explained earlier) and the alternating curls of wind fields powered by the surface-pressure gradient. The general outline of the key atmospheric parameters and the controlling weather elements associated with the snow event were not unique but they manifested at an amplitude that had been rarely achieved or fulfilled in the recent past.

Figure 7. A: Determination of precipitation-phase partitioning with 5400-m thickness contour (blue line), 0º-level line (green), and isotherms of surface temperature (red). The blue shades show the occurrence and intensity (dark to light represents decreasing intensity) of the snowfall at 06:00Z on 4 February. B: Surface isobars and isotachs showing pressure changes driving the surface-wind conditions;

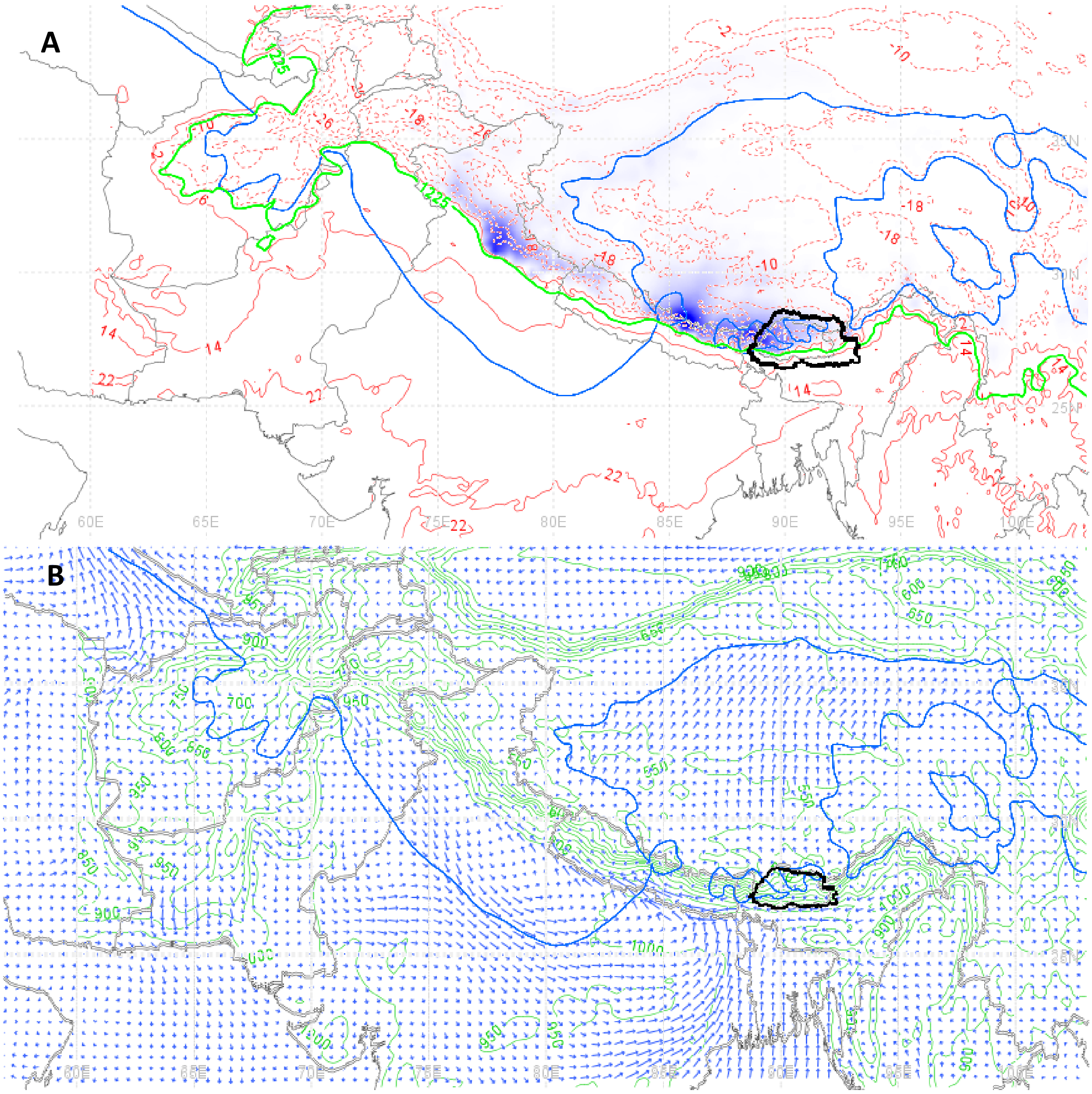

d - Surface precipitation footprints of atmospheric dynamics

To examine and accurately locate the ground-level footprints of precipitation, we used the observations and multi-source merged datasets (IMERG, MSWEP) together with the cloud-cover extent from the ERA5 reanalysis data. The gage-based daily observational data unfortunately lacked the spatiotemporal resolution and snowfall details that we required for a meaningful analysis. Alternatively, we explored and considered the ERA5-Land reanalysis to provide realistic estimates of snow-related parameters in validating of the results from our composite analysis of upper-air features in event detection and evolution. The uncertainty in observations for 7 days case study was considered to be greater than that of the ERA5-Land dataset as the latter is derived from lapse-rate corrected atmospheric forcing, applying robust checks for usability and reliability. Figure 8 shows the spatial pattern of event precipitation at the surface during the peak snowfall episode from 06z – 12z on 4 February.

The surface precipitation from MSWEP28-NRT and IMERG-Late constructions were comparable with 327.38 mm and 406.68 mm respectively in daily maximum accumulated totals, while the total maximum precipitation from ERA5-Land reanalysis was more than twice the value obtained with multi-source-gridded dataset using the previous two methods (Figure 8-B). Since the MSWEP product is based on a state-of-the-art gage, satellite, and reanalysis data sources, and assessed to exhibit better performance than other similar multi-source products (Beck et al., 2019), we used it here as a reference for diagnosing the significance of upper-air synoptic features in controlling the spatiotemporal patterns of occurrence, duration, and intensity of the snowfall. The IMERG-based precipitation indicated a slight overestimation compared to that derived from MSWEP-NRT. However, the distributions were similar, with the highest one-day intense precipitation concentrated in the foothills of north-west Bengal, bordering Nepal and Bhutan. Much of the area under the precipitation footprint received no less than 50 mm/day of precipitation, which is considered extreme according to the World Meteorological Organization (WMO) classification guide. The heavy precipitation corridor extended south to the Bay of Bengal, indicating a surfeit moisture flux that fed the extreme event, while its distribution pattern was also mirrored in the total column of vertically integrated water vapour and specific and relative humidity (not shown). The convective feature and shallow convection cells certainly did contribute to the increase in precipitable water to feed the snow-spawning system. As displayed in Figure 8 (A:a–d), the system shifted eastward by about 300 km between 00Z and 18:00Z, and evaporated over the far-eastern end of the Himalayan range. Upstream pockets of discontinuous precipitation over central Nepal also evaporated as the WD got cut off as atmospheric structure rapidly returned to stable stratification. However, the centre of maximum precipitation was spatially confined to the south-western border of Bhutan, and considerably weakened by the end of the day. The overall effect of the disturbance was widespread snowfall over greater part of the Himalayas and Bhutan, recognisable from the MODIS-based improved daily snow-cover products (Thapa & Mohammad, 2021) provided in the supplementary material.

Figure 8. The left-hand column shows the evolution of three-hour surface precipitation from MSWEP-NRT from 00Z to 18:00Z on 4 February. The right-hand column provides a visual comparison between the precipitation estimates derived from different products (a – CPC, b – ERA5-Land, c – IMERG, d – MSWEP-NRT).

A. Sequence of MSWEP-NRT 3-hour accumulated precipitation in a 6-hour time step on 4 February

B. Estimates of daily total precipitation from state-of-the-art sources of harmonised data sets (CPC, ERA5-Land, IMERG, MSWEP)

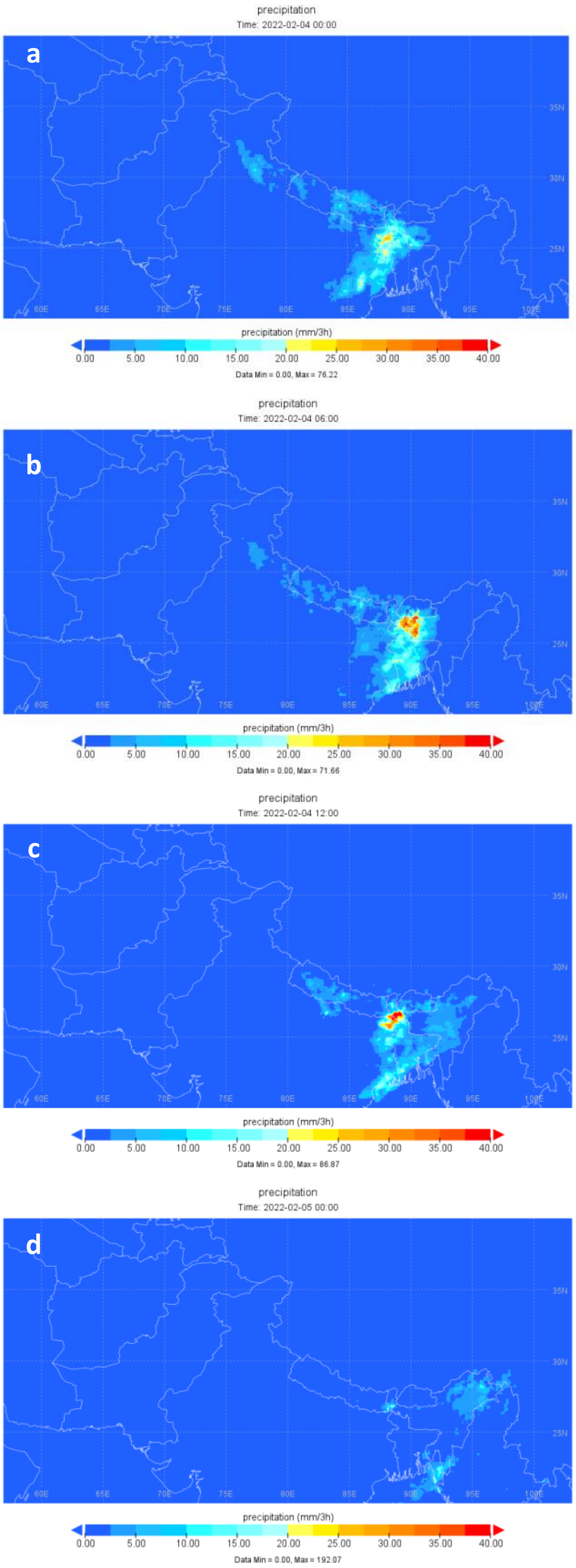

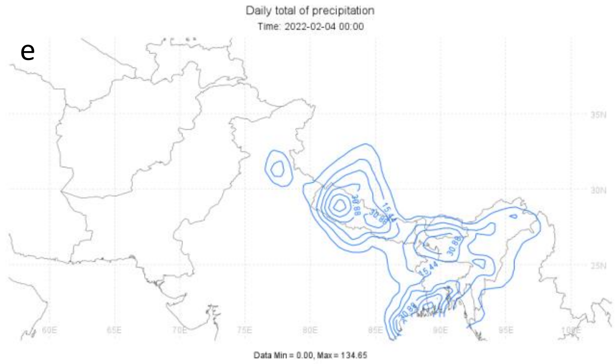

e. CPC GLOBAL PRCP V1.0 RT daily total precipitation (mm) on 4 February

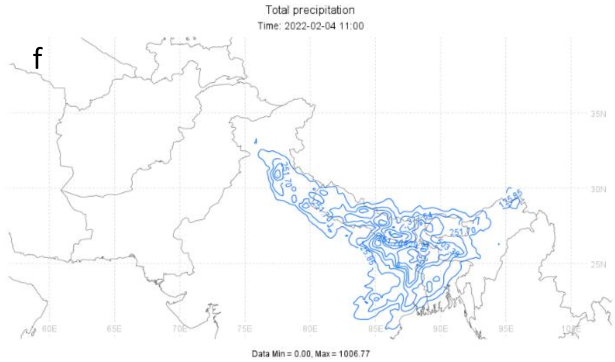

f. ERA5-Land daily total precipitation (mm) on 4 February

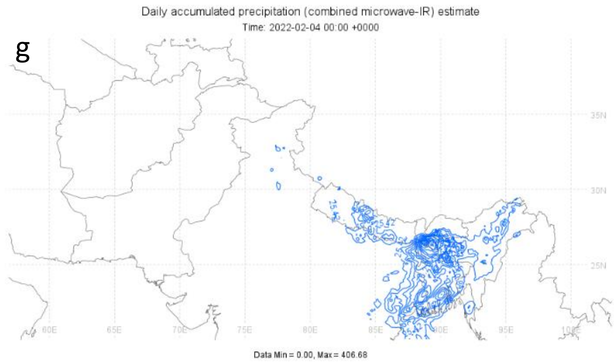

g. IMERG-Late daily total precipitation (mm) on 4 February

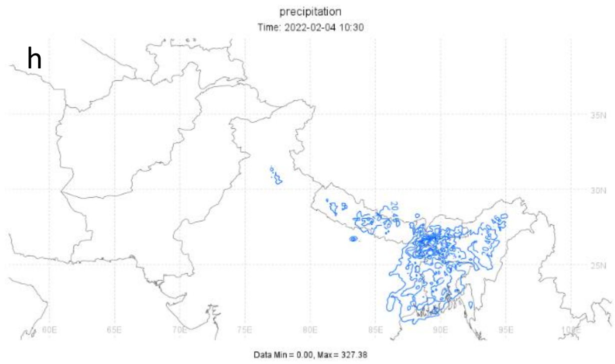

h. MSWEP-NRT daily total precipitation (mm) on 4 February

e - Mesoscale perspective on synoptic structure and dynamics

Embedded in the synoptic motion is the mesoscale motion driven by local temperature and pressure gradients, frontal activities, convection, etc. The mesoscale precipitation along the mountain range fed by the westerly aloft and easterly beneath played an important role in bringing rain and snow to the north-eastern part of the Himalayas, especially at lower elevation and along the foothills. Their characterisation is only possible through the use of highly resolved datasets such as those generated by weather models, ground radar, and the dense network of upper-air-sounding stations. Setting up and running such a numerical weather prediction (NWP) model in a hindcast mode is beyond the scope of this study. The analysis and evaluation of mesoscale features simulated by such NWP during the study period would have revealed more details about the mesoscale transverse circulation about the SWJ, with a large magnitude lift steering the weather system to generate copious snow. Local-scale land–atmosphere interactions often create situations quite distinct from the synoptic-scale weather with transient and insular elements, as well as features and processes that are important red flags for operational forecasters to weigh the potential and anticipate extreme events from the clues in the mesoscale patterns. Cannon et al. (2014) found that the magnitude and frequency of WDs were greatest in the north-west of the Indian Subcontinent and decreased as they progressed eastward. However, there were significant uncertainties in synoptic-scale investigations, which can only be resolved through full-physics, limited-area modelling experiments. Archives of NWP products for the study area are not available as the model outputs (especially the upper air simulations at crucial diagnostic heights) from operational modes were not maintained due to poor computing infrastructure, and event-based reruns for research purposes were generally not implemented in the region. Therefore, local-level verification of the synoptic diagnosis was not possible within the frame of this study. Despite this study uncovering the key synoptic-scale features responsible for the bizarre snowfall event, the actual mechanism was difficult to determine without the mesoscale observations or high-resolution NWP outputs.

Discussion on the results

It has been demonstrated that excessive snowfall over the eastern Himalaya in general, and over Bhutan in particular, typically originates under conditions of deep geopotential trough, intensified westerly jet, and ascending motion due to orographic forcing and topographic uplift, together with the abundance of moisture supplied from the Bay of Bengal and the Arabian Sea (Zhang et al., 2004). This study has provided a diagnostic analysis of a heavy snowfall event that brought snow to locations that had never experienced it in the last 66–72 years. The key meteorological elements on a synoptic scale were examined to uncover the antecedent atmospheric features that induced the exceptional snowfall event last winter. The evolution of dynamic and thermodynamic processes, as well as wind and moisture fluxes were assessed against the weather conditions on the ground to identify the favourable synoptic and mesoscale conditions that initiated this unexpected weather occurrence. The striking geopotential features, the vertical motion framed within the diverging tendencies, and the associated vortical perturbations in concert have a defining influence on local weather manifestation. There has to be abundant moisture to produce precipitation and optimal stratification of the vertical temperature gradient to phase it as snow on the ground. In the present case, that condition was fulfilled by the moisture carried from the far-western waterbodies in the westerly flow and the entrainment of the convective flow from the low-pressure area over the Bay of Bengal, and also by the moisture fluxes from the south-west. At the time of this remarkable snowfall over Bhutan, moisture advection coincided with the location of warm advection, thereby favouring the occurrence of this snowfall event.

The dynamics of the case of an unusual snowstorm event that pummelled the length of the Himalayan range and delivered a historic snowfall over Bhutan centred on 4 February 2022 was investigated in the context of initiation, evolution, and decay of anomalous meteorological perturbances at isobaric levels. All the parameters employed in the study describe the same set of atmospheric features characteristic of a winter snowstorm. The isobaric vorticity analyses were able to describe the upper- and near-surface-level dynamic and thermodynamic processes together with the structural instabilities that primed the weather system for this eventful snowfall. The key fingerprints were the interaction of a region of positive relative vorticity advection ahead of a 500-hPa trough with a shallow frontal system, and the upper-level potential vorticity anomaly associated with the lower-level baroclinic zone, as well as with the shallow frontal system.

The synoptic conditions that favour deep, low-valley-penetrating snowfall events are dynamically very different from the normal winter season conditions. The multi-field analysis conducted in this study to uncover the meteorological conditions that triggered the snowfall event is considered justified although the inclusion of other variables may have yielded a greater insight into the synoptic features of interest in terms of operational forecasts. Definitely, a more elaborate analyses is desirable for a detailed reconstruction of the coupled land-sea-air thermodynamics of the weather system at scale to enable a physical interpretation of the event. But this entails a bigger and broader study of a longer-term nature in a collaborative teamwork of specialist earth scientists. With the comprehension afforded through our analysis as explained in the Results section, we have presented a model of the key synoptic features responsible for the interaction and coincidence of different dynamical processes, along with the coevolution of wind and moisture patterns. This study will further improve our knowledge and understanding about the occurrence, development, and evolution of such rare snowfall events in the future. We believe this study will surely contribute to deepening our insight into uncharacteristic snowfalls that we could expect under changing climate and provide robust predictions for preparedness and effective response against extreme weather conditions. The preliminary analysis of a significant snowfall over the Himalaya and its extraordinary occurrence over Bhutan described above has outlined many aspects of the dynamical interactions between the mountain range and the westerly flow. An integration of different sources of data is essential for a more complete description of the mechanism of the event, beyond the usual integration of gage, EO, and simulated and reanalysed data products. An increased cyclonic westerly flow in February, depressed geopotentials, below-freezing temperature throughout the vertical column of the atmosphere, higher relative humidity, and strong ascending motions are some of the key highlights of this abridged regional overview and expanded localised case study about this uncommon snowfall event.

Summary and conclusion

Explaining the unusual snowfall of last winter (DJFM, 2021–22) involved a complex meteorological study. Several weather fields and thermodynamic features interacted with each other as well as the land surface in creating the right environment for seeding the precursory ice crystals and super-cooled water droplets and, again under the right condition, fell to the ground as snow in least expected locations. As mentioned in the preceding sections, the object and focus of this study was not to dwell on the conventional measurements of extreme events in terms of depth and extent, but specifically to take a synoptic snapshot (ERA5 also resolved meso-α-scale details) of the three-dimensional view of the key meteorological variables and fields to uncover the then prevailing atmospheric dynamics and structure over the event period assessed at a short-(hourly)-to-medium (seven days) range. Accordingly, the study implemented a composite analysis approach rather than a comparative analysis, with the underlying purpose to address the question of why many places, especially in the eastern Himalayas, witnessed rare, once-in-a-lifetime (e.g. Punakha and the Wangdi Valley in Bhutan) snowfalls despite the common narrative of a rapidly warming world. We believe the answer lies in understanding the synoptic and mesoscale dynamics associated with the event and not in merely characterising its anomaly with extreme statistics based on standard measurements of snowfall or providing historical or future contexts.

In this study, we have utilised the weather observation tools (ground and satellite), the ERA5 reanalysis products, and research data sets from past studies to present a synoptic overview of the prevailing meteorological conditions from the ground to the upper atmosphere during the snowfall event of the 2021–22 winter season, specifically focusing on such a rare event in Bhutan. The objective was to investigate the atmospheric anomalies in its fields and features that provided the right structural and dynamical context in three-dimensional space and evolution over time for the event to transpire as it did on 4 February 2022. The results obtained from the analysis of meteorological parameters at selected layers of the upper atmosphere on pressure levels indicated the concurrence of several short-range weather phenomena triggered by an intense bout of WD, strong westerly flow, cold wave in the foothills and plains of northern India, moisture convergence piped in from the Bay of Bengal, and a vertical temperature profile favouring snow over other forms of precipitation. The findings contribute to a greater understanding of the mechanism and processes involved at synoptic scale in the elucidation of the snow weather pattern. The findings also strengthen the forecasting procedure in operational meteorology for accurate and timely prediction of rare and extreme events. More than ever before, national weather services now have access to more situational intelligence, guidance materials, and tools to explore broader fields in atmospheric dynamics and prognostic features beyond the traditional practice of drawing insights from meteograms and pressure charts. The ultimate objective recognisably was to improve forecast reliability and skill and accuracy in order to inform decisions and actionable solutions that can enhance safety and socioeconomic security, as well as reduce risks and reap benefits.

WDs are extratropical systems embedded in the SWJ responsible for winter rainfall at lower elevations and snowfall at higher elevations in the western Himalaya. Here, winter precipitation is critical for agriculture and for replenishing glaciers and snowpack, which are vital for water security. WDs are also associated with hydrometeorological hazards like floods, landslides, and avalanches which cause disasters across the Himalayas. The WDs are embedded features of the SWJ interacting with the mountain ranges, which presents an opportunity for seasonal predictability through global teleconnections, such as the NAO and ENSO that influence the position, frequency and intensity of the SWJ (Hunt et al., 2018), and hence the baroclinic instability of WDs. WDs are therefore fundamental atmospheric features that redistribute energy, momentum, and moisture at a regional scale. So, the understanding of WD activities and their interactions with the Himalayan ranges is fundamental to any snow-related study in the region.

The causal clues to the meteorological drivers of the snowfall event were diagnosed and inferred from the assessment of the atmospheric structure and dynamics controlling the region’s weather system from 1–7 February 2022. The investigation at 13 vertical levels in the troposphere over the study area was adequate to uncover the key weather fields and thermodynamic features characterising the event. Upper-air pressure, geopotential height, moisture, wind, vorticity, and velocity fields, as well as temperature and precipitation at the surface level were analysed to detect the parametric signatures and event footprint on the ground. The SWJ in the westerly wind is a prominent feature at 200- and 300-hPa levels, although the streamline velocity is slightly reduced and shifted poleward at 300 hPa since geopotential heights decrease from the equator to the poles. Under normal climatology, the alternating pressure troughs and ridges in the SWJ shifting from a negative (westward) tilt to a positive one suggests the weakening of WDs to complete dissipation on their passage eastward, and consequently, less snow in terms of frequency and intensity. However, in this case event, the pressure trough sustained its negative tilt during the course of its life cycle, which was suggestive of a stronger westerly than in a normal season. The orographic uplift forced by the Himalayas further accentuated the cyclonic flow pattern, thereby generating a wave-train of intense positive vorticity which when juxtaposed with low-level moisture incursion led to the episodic precipitation along the southern slopes of the range. Further, a vorticity of the most intense kind overlapped with the trough at its greatest geopotential gradient and consistently north of the SWJ core. But the places that reported snowfall were downstream (east) of the vorticity maxima associated with flow convergence and ascending vertical motion. Therefore, we infer that the rate of change in vortical intensity may be more important than the absolute vorticity value in determining the magnitude and duration of a WD governing snow weather in the Himalayas. Temperatures in the lower troposphere dictate whether precipitation will fall as rain, snow, or something in between (sleet). The phase of precipitation is not always easy to predict; snowfall is commonly recorded at near-surface temperatures well above 0°C, while rain can occur at temperatures below 0°C. This depends on the temperature structure in the atmospheric boundary layer, the initial size of the precipitation particle, and the transit time (height, speed, and path) of the precipitation. The ERA5 reanalysis data was able to represent explicitly the precipitation processes and the phase of precipitation on the temporal and spatial scales needed for a detailed evolution of weather systems.

As long as sufficient moisture is available in a cloud, ice crystals (snowflakes) will continue to grow until they become heavy enough to drift to the ground. Snowfall is associated with two main mechanisms of precipitation: an orographic uplift of moist air masses; and air-mass mixing/frontal precipitation. Both mechanisms were at work in the case of the snowfall along the southern slopes of the Bhutan Himalayan range, where inland advection of moist air masses led to an uplift, and the warm front from the Bay of Bengal interacting with the WDs embedded in the westerly streamline pushed southward due to the cold-air intrusion, thereby forcing the warm air to gradually rise. This led to stratiform cloudiness and precipitation north of the front, as well as a transition from rainfall at low altitudes to snowfall at higher elevations. Since the 5400-m thickness contour sat south of the foothills of the Bhutan Himalaya on 4 February, the low-lying areas north, particularly along the western-central belt, received snow of varying amounts, including in the interior, subtropical valleys of Punakha and Wangdi. In this rare event, the orographic and frontal precipitation processes acted in concert to deliver more moisture than possible under the control of only a single mechanism. However, the exact, local-scale driving mechanism that brought snow to the subtropical altitudes as low as 1000 masl was difficult to determine due to the lack of - intensive mesoscale observations; more granular reanalysis products; numerical weather prediction (NWP) outputs; upper air soundings; and radar imageries. Future studies purposed around similar issues could deepen as well as broaden the knowledge and insights into the governing physics of atmospheric dynamics and thermodynamical forcing by focusing in-depth on: regional wind circulations; teleconnections between pressure centres; the deep convection associated with WDs and extratropical lows of monsoonal origin; moisture advection and convergence along the Himalayan foothills; linkages between SWJ meanders amplifying or shallowing; the intensity of WDs; and cold-air intrusion southward into the Indo-Gangetic plains of North India.

By investigating an inclusive perspective of WDs and how they interact with the background atmosphere, we have further improved our understanding of the factors that influence winter precipitation over Bhutan. Moving forward, this provides a basis on which we may better comprehend how a changing climate will affect WDs and the winter precipitation in the HKH region and thus improve our ability to project into future decades while minimising uncertainty with respect to potential disruptions and risks in the mountain hydrological cycle and water resources. To conclude, a few points from the study are worth reiteration:

- The upper- and mid-tropospheric depressions set up a favourable large-scale environment for snowfall in the Himalayas through the establishment of SWJ flow against topographic barriers, local mesoscale factors, cross-barrier flow, and the moisture flux entrained within and advected/convected en route during its west–east passage.
- Snowfall is unambiguously related to the presence of orographically captured depressions like WDs, which are westerly waves trapped and intensified by the unique large-scale topographic feature of the Himalayan mountains.
- Based on the correspondence between low-average geopotentials and temperatures, along with the high number of cold and depression events, the future years that are most likely to feature a similar snowfall event like the one in 2022 are those that will see abundant atmospheric water vapour and moisture fluxes and exchanges with other systems like tropical depressions and low-pressure areas.
- Strong westerlies over South Asia continue blowing against the Himalayas, suggesting that orographic lifting plays an important role in the regional circulation, particularly at > 500 hPa where the winds are less susceptible to blocking and where its ascending vertical motion is at its maximum.
- Clouds are either isentropically, diabatically, or orographically generated, as their creation regions are fixed in space along the mountains given a favourable geometry.
- The unusual dynamic coupling of an upper trough in the westerly streamline with the remnants of a low-pressure system over the Bhutan Himalayas could enhance lifting and moisture pooling, causing heavy snowfall that could occur even at low-elevation areas, especially in valleys oriented to facilitate deep moisture intrusion from the south.
- Climate diagnostics indicate greater tendency for development and sustained troughs in the mid- and upper tropospheric westerlies in their passage eastward; and the tropical disturbances becoming stronger and shifting northward with increasing SST; SWJ stream nudging equator-ward under changing synoptic regime for heightened probability of similar event in the future.

References

Almazroui, M., Saeed, S., and Saeed, F. et al. (2020). Projections of precipitation and temperature over the South Asian Countries in CMIP6. *Earth Systems and Environment*, 4, 297–320. https://doi.org/10.1007/s41748-020-00157-7.

Barnes, E.A., and Polvani, L. (2013). Response of the midlatitude jets, and of their variability, to increased greenhouse gases in the CMIP5 models. *Journal of Climate*, 26, 7117–7135. https://doi.org/10.1175/JCLI-D-12-00536.1.

Barros, A. P., and Lettenmaier, D. P. (1994). Dynamic modeling of orographically induced precipitation. *Reviews of Geophysics*, *32*(3):265–284.

Beck, H. E., Wood, E. F., Pan, M., Fisher, C. K., Miralles, D. M., van Dijk, A. I. J. M., McVicar, T. R., and Adler, R. F. (2019). MSWEP V2 global 3-hourly 0.1° precipitation: Methodology and quantitative assessment. *Bulletin of the American Meteorological Society*, *100*(3), 473–500.

Bookhagen, B., Thiede, R. C., and Strecker, M. R. (2005). Abnormal monsoon years and their control on erosion and sediment flux in the high, arid northwest Himalaya. *Earth and Planetary Science Letters*, *231*(1–2):131–146.

Cannon, F., Carvalho, L. M. V., and Jones, C. et al. (2014). Multi-annual variations in winter westerly disturbance activity affecting the Himalaya. *Climate Dynamics*, 44, 441–455. doi:10.1007/s00382-014-2248-8.

Cannon, F., Carvalho, L. M. V., Jones, C., and Norris, J. (2016). Winter westerly disturbance dynamics and precipitation in the western Himalaya and Karakoram: A wave-tracking approach. *Theoretical and Applied Climatology*, *125*(1–2). doi:1007/s00704-015-1489-8.

Chang, E. K. M., Guo, Y. J., and Xia, X. M. (2012). CMIP5 multimodel ensemble projection of storm track change under global warming. Journal of Geophysical Research, 117, D23118. https://doi.org/10.1029/2012JD018578.

Dimri, A. P., and Chevuturi, A. (2016). *Western Disturbances – An Indian Meteorological Perspective*. Springer, pp. 5–7. ISBN: 978-3319267371.

Viste, E., and Sorteberg, A. (2015): Snowfall in the Himalayas: An uncertain future from a little-known past. *The Cryosphere*, 9, 1147–1167. www.the-cryosphere.net/9/1147/2015/.

Hansen, C., Kaplan, M. L., Mensing, S. A., Underwood, S. J., Lewis, J. M.,. King, K. C, and Haugland, J. E. (2013). They just don't make storms like this one anymore: Analyzing the anomalous record snowfall event of 1959. Journal of Operational Meteorology, *1*(5), 52–65. doi:http://dx.doi.org/10.15191/nwajom.2013.0105.

Hara, M., Kimura, F., and Yasunari, T. (2004). The generation mechanism of the western disturbances over the Himalayas. In Sixth International GAME Conference, 3–5 December 2004, Kyoto, Japan. http://hyarc.nagoya-u.ac.jp/game/6thconf/html/abs_html/pdfs/T4HM09Aug04145134.pdf.

Harvey, B. J., Shaffrey, L. C., and Woollings, T. J. (2014). Equator-to-pole temperature differences and the extra-tropical storm track responses of the CMIP5 climate models. *Climate Dynamics*, 43, 1171–1182. https://doi.org/10.1007/s00382-013-1883-9.

Herring, S. C., Hoerling, M. P., Kossin, J. P., Peterson, T. C., and Stott, P. A.. (2015). Explaining extreme events of 2014 from a climate perspective. Bulletin of the American Meteorological Society, *96*(12), S1–S172.

Hersbach, H., Bell, B., Berrisford, P., Biavati, G., Horányi, A., Muñoz Sabater, J., Nicolas, J., Peubey, C., Radu, R., Rozum, I., Schepers, D., Simmons, A., Soci, C., Dee, D., and Thépaut, JN. (2018). ERA5 hourly data on single levels from 1979 to present. Copernicus Climate Change Service (C3S) Climate Data Store (CDS). doi: 10.24381/cds.adbb2d47. (Accessed on 14 April 2021).

Houze, R. A., McMurdie, L. A., Rasmussen, K. L., Kumar, A., and Chaplin, M. M. (2017). Multiscale aspects of the storm producing the June 2013 flooding in Uttarakhand, India. *Monthly Weather Review*, 145, 4447–4466. https://doi.org/10.1175/MWR-D-17-0004.1.

Huffman, G. J., Adler, R. F., Rudolf, B., Schneider, U., and Keehn, P. R. (1995). Global precipitation estimates based on a technique for combining satellite-based estimates, rain gauge analysis, and NWP model precipitation information. *Journal of Climate*, 8, 1284–1295. https://doi.org/10.1175/1520-0442(1995)008<1284:GPEBOA>2.0.CO;2.

Huffman, G. J., Bolvin, D. T., Braithwaite, D., Hsu, K. L., Joyce, R. J., Kidd, C., Nelkin, E. J., Sorooshian, S., Stocker, E. F., and Tan, J. (2020). Integrated Multi-Satellite Retrievals for the Global Precipitation Measurement (GPM) Mission (IMERG). In *Satellite Precipitation Measurement*. Berlin, Germany: Springer, pp. 343–353.

Hunt, K. M. R., Turner, A. G., and Shaffrey, L. C. (2019). Falling trend of western disturbances in future climate simulations. *Journal of Climate*, 32. doi:10.1175/JCLI-D-18-0601.1.

Hunt, K. M. R., Turner, A. G., and Shaffrey, L. C. (2018). Extreme daily rainfall in Pakistan and north India: Scale interactions, mechanisms, and precursors. Monthly Weather Review, 146, 1005–1022. https://doi.org/10.1175/MWR-D-17-0258.1.

Hunt, K. M. R., Turner, A. G., and Shaffrey, L. C. (2018). The evolution, seasonality and impacts of western disturbances. *Quarterly Journal of the Royal Meteorological Society*, 144, 278–290. doi:10.1002/qj.3200.

Hunt, K. M. R., Turner, A. G., and Shaffrey, L. C. (2019). Representation of western disturbances in CMIP5 models. *Journal of Climate*, *32*(7), 1997–2011. Retrieved on 19 June 2022 from: https://journals.ametsoc.org/view/journals/clim/32/7/jcli-d-18-0420.1.xml.

ICIMOD. (2019). Summary of the Hindu Kush Himalaya Assessment Report. HMAP.

Jennings, K. S., Winchell, T. S., and Livneh, B. et al. (2018). Spatial variation of the rain–snow temperature threshold across the Northern Hemisphere. *Nature Communications*, 9, 1148. https://doi.org/10.1038/s41467-018-03629-7.

Kotal, S. D., Roy, S. S., and Bhowmik, S. K. R. (2014). Catastrophic heavy rainfall episode over Uttarakhand during 16–18 June 2013 – Observational aspects. Current Science, 107, 234–245.

Kumar, N., Yadav, B. P., Gahlot, S., and Singh, M. (2015). Winter frequency of western disturbances and precipitation indices over Himachal Pradesh, India: 1977–2007. *Atmósfera*, 28, 63–70. https://doi.org/10.20937/ATM.2015.28.01.06.

Lakkis, S. G., Canziani, P., and Rocamora, L. et al. (2019). A 4D feature-tracking algorithm: A multidimensional view of cyclone systems. *Quarterly Journal of the Royal Meteorological Society*, 1–23. https://doi.org/10.1002/qj.3436.

Lang, T. J., and Barros, A. P. (2004). Winter storms in the central Himalayas. *Journal of the Meteorological Society of Japan*, 82,829–844.

Li, L., Lin, P., Yu, Y. et al. The flexible global ocean-atmosphere-land system model, Grid-point Version 2: FGOALS-g2. Adv. Atmos. Sci. 30, 543–560 (2013). https://doi.org/10.1007/s00376-012-2140-6.

Liu, L., Ma, Y., Yao, N., and Ma, W. (2021). Diagnostic analysis of a regional heavy snowfall event over the Tibetan Plateau using NCEP reanalysis data and WRF. *Climate Dynamics*, 56, 2451–2467. https://doi.org/10.1007/s00382-020-05598-4.

Miglietta, M. M. (2019). Mediterranean tropical-like cyclones (Medicanes). *Atmosphere*, 10, 206. doi:10.3390/atmos10040206.

Mishra, V., Bhatia, U., and Tiwari, A. D. (2020). Bias corrected climate projections from CMIP6 models for South Asia. Zenodo. https://doi.org/10.5281/zenodo.3987736.

Mooley, D. A. (1957). The role of western disturbances in the production of weather over India during different seasons. *Indian Journal of Meteorology and Geophysics*, 8, 253–260.

Muhammad, S., and Thapa, A. (2020). An improved Terra–Aqua MODIS snow cover and Randolph Glacier Inventory 6.0 combined product (MOYDGL06*) for high-mountain Asia between 2002 and 2018. *Earth System Science Data*, *12*(1), 345–356.

Palazzi, E., Hardenberg, J., and Provenzale, A. (2013). Precipitation in the Hindu-Kush Karakoram Himalaya: Observations and future scenarios. *JGR Atmospheres*, 118, 85–100. https://doi.org/10.1029/2012JD018697.

Power, K. (2021). Regional and local impacts of ENSO and IOD events of 2015 and 2016 on the Indian Summer Monsoon – A Bhutan case study. Thesis report. Stockholm University.

Roy, S. S., and Bhowmik, S. K. R. (2005). Analysis of thermodynamics of the atmosphere over northwest India during the passage of a western disturbance as revealed by model analysis field. *Current Science*, 88, 947–951.

Seidel, D. J., Fu, Q., Randel, W. J., and Reichler, T. J. (2008). Widening of the tropical belt in a changing climate. Nature Geoscience, 1, 21–24. https://doi.org/10.1038/ngeo.2007.38.

Seneviratne, S. I., Zhang, X., Adnan, M., Badi, W., Dereczynski, C., Di Luca, A., Ghosh, S., Iskandar, I., Kossin, J., Lewis, S., Otto, F., Pinto, I., Satoh, M., Vicente-Serrano, S. M., Wehner, M., and Zhou, B. (2021). Weather and climate extreme events in a changing climate. In Climate Change 2021: The Physical Science Basis. Contribution of Working Group I to the Sixth Assessment Report of the Intergovernmental Panel on Climate Change (V. Masson-Delmotte, P. Zhai, A. Pirani, S. L. Connors, C. Péan, S. Berger, N. Caud, Y. Chen, L. Goldfarb, M. I. Gomis, M. Huang, K. Leitzell, E. Lonnoy, J. B. R. Matthews, T. K. Maycock, T. Waterfield, O. Yelekçi, R. Yu, and B. Zhou – eds.). Cambridge, UK and USA: Cambridge University Press, pp. 1513–1766. doi:10.1017/9781009157896.013.

Sharma, R., and Subramaniam, D. (1983). The western disturbance of 22 December 1980: A case study. *MAUSAM*, 34, 117–120.

Shekhar, M. S., Chand, H., Kumar, S., Srinivasan, K., and Ganju, A. (2010). Climate-change studies in the western Himalaya. *Annals of Glaciology*, 51, 105–112. https://doi.org/10.3189/172756410791386508.

Stott, P. A., and Walton, P. (2013). Attribution of climate-related events: Understanding stakeholder needs. *Weather*, 68, 274–279. doi:10.1002/wea.2141.

TianJun, Z., Bin, W., and YongQiang, Y. et al. (2018). The FGOALS climate system model as a modeling tool for supporting climate sciences: An overview. *Earth and Planetary Physics*, 2, 276–291. http://doi.org/10.26464/epp2018026.

Turner, A. G., and Hunt, K. (2019). BITMAP: Tracks of western disturbances (1979–2015). Centre for Environmental Data Analysis. http://catalogue.ceda.ac.uk/uuid/b1f266c25cf2445f8b87d874f6ac830a.

Wang, D., Liu, J., Wang, H., Shao, W., Mei, C., and Ding, X. (2022). Performance evaluations of CMIP6 and CMIP5 models for precipitation simulation over the Hanjiang River Basin, China. *Journal of Water and Climate Change*, *13*(5): 2089–2106. https://doi.org/10.2166/wcc.2022.402.

Wang, S. -Y. S., Fosu, B., Gillies, R. R., and Singh, P. M. (2015). The deadly Himalayan snowstorm of October 2014: Synoptic conditions and associated trends. *Bulletin of the American Meteorological Society*, *96*(12): S89–S94.doi:10.1175/BAMS-D-15-00113.1.

Wester, P., Mishra, A., Mukherji, A., and Shrestha, A. B. (eds). (2019). *The Hindu Kush Himalaya Assessment – Mountains, Climate Change, Sustainability and People*. Switzerland AG, Cham: Springer Nature. https://doi.org/10.1007/978-3-319-92288-1.

Zhang, Y., Li, T., and Wang, B. (2004). Decadal change of the spring snow depth over the Tibetan Plateau: The associated circulation and influence on the east Asian summer monsoon. Journal of Climate, 17, 2780–2793.

---

[i] Stott, P. A., and Walton, P. (2013). Attribution of climate-related events: Understanding stakeholder needs. *Weather*, 68, 274–279. doi:10.1002/wea.2141.

[ii] Hara, M., Kimura, F., and Yasunari, T. (2004). The generation mechanism of the western disturbances over the Himalayas. In Sixth International GAME Conference, 3–5 December 2004, Kyoto, Japan. http://hyarc.nagoya-u.ac.jp/game/6thconf/html/abs_html/pdfs/T4HM09Aug04145134.pdf.

[iii] Liu, L., Ma, Y., Yao, N., and Ma, W. (2021). Diagnostic analysis of a regional heavy snowfall event over the Tibetan Plateau using NCEP reanalysis data and WRF. *Climate Dynamics*, 56, 2451–2467. https://doi.org/10.1007/s00382-020-05598-4.

[iv] Wang, S. -Y. S., Fosu, B., Gillies, R. R., and Singh, P. M. (2015). The deadly Himalayan snowstorm of October 2014: Synoptic conditions and associated trends. *Bulletin of the American Meteorological Society*, *96*(12): S89–S94.doi:10.1175/BAMS-D-15-00113.1.

[v] Huffman, G. J., Bolvin, D. T., Braithwaite, D., Hsu, K. L., Joyce, R. J., Kidd, C., Nelkin, E.J., Sorooshian, S., Stocker, E. F., and Tan, J. (2020). Integrated Multi-Satellite Retrievals for the Global Precipitation Measurement (GPM) Mission (IMERG). In *Satellite Precipitation Measurement*. Berlin, Germany: Springer, pp. 343–353.

[vi] Beck, H. E., Wood, E. F., Pan, M., Fisher, C. K., Miralles, D. M., van Dijk, A. I. J. M., McVicar, T. R., and Adler, R. F. (2019). MSWEP V2 global 3-hourly 0.1° precipitation: Methodology and quantitative assessment. *Bulletin of the American Meteorological Society*, *100*(3), 473–500.

[vii] Hersbach, H., Bell, B., Berrisford, P., Biavati, G., Horányi, A., Muñoz Sabater, J., Nicolas, J., Peubey, C., Radu, R., Rozum, I., Schepers, D., Simmons, A., Soci, C., Dee, D., and Thépaut, JN. (2018). ERA5 hourly data on single levels from 1979 to present. Copernicus Climate Change Service (C3S) Climate Data Store (CDS). doi: 10.24381/cds.adbb2d47. (Accessed on 14 April 2021).

[viii] https://cds.climate.copernicus.eu/#!/home.

[ix] Power, K. (2021). Regional and local impacts of ENSO and IOD events of 2015 and 2016 on the Indian Summer Monsoon – A Bhutan case study. Thesis report. Stockholm University.

[x] https://edition.cnn.com/2022/01/25/weather/weather-climate-snowstorm-greece-turkey-intl/index.html.

The Efficacy of Kalman Filtering Near-surface Temperature Forecasts in Bhutan

Dechen Lhamo Gyeltshen[1,*], Kiichi Sasaki[2], Singay Dorji[1], and Pema Syldon[1]

[1]National Centre for Hydrology and Meteorology, Bhutan

[2]Japan Meteorological Business Support Center, Japan

[*]Corresponding author: dlgyeltshen@nchm.gov.bt

Abstract

Meteorological data and forecast products have a diverse array of users; the public, the government, and private businesses among others. For all intents and purposes, the quality of data and the accuracy of forecasts is pivotal to making sound decisions. Reliable and accurate weather forecasts can support socio-economic development and essential early warning services. Hence, it is important to actively validate new and better methods to forecast the weather with greater accuracy. This paper aimed to investigate the efficacy of Kalman Filtering near-surface temperature forecasts in Bhutan by comparing its verification scores to other operational methods such as Numerical Weather Prediction models and consensus forecast. The primary score used was root-mean-square error with Pearson correlation coefficient as the secondary metric. This preliminary verification was done at 20 spatial points (corresponding to 20 observation stations) for the months of March and April. The range used was limited due to data unavailability at the time of study. The results showed that for both maximum and minimum temperatures, the integrated WRF4-GSM Kalman Filter temperature guidance performed the best. It had the lowest root-mean-square errors of 1.85 (maximum temperature) and 1.46 (minimum temperature) proving its efficacy over existing methods. A nuanced analysis of point-specific performance revealed that the errors varied considerably across regions with no discernible pattern alluding to a confounding variable or inconsistent observation data.

1 Introduction

Weather forecasts are of high economic and social value, especially in developing countries where critical decisions are made largely based on data. Planning activities on scales ranging from everyday routines to national policies rely on meteorological data and forecasts. Many economic sectors like agriculture, renewable energy, aviation, tourism, and disaster management are highly environment-sensitive and require good quality forecasts. The public is also increasingly dependent on forecasts and early warning services, especially in a changing climate. Meteorological service providers around the world rely on sophisticated computer tools for accurate forecasts. For example, the UK Met Office uses their state-of-the-art Unified Model for both weather and climate forecasts on a range of spatial scales (The Met Office, 2025). The model is also capable of incorporating different data assimilation schemes and ensembles. In Bhutan, as the agency responsible for providing meteorological services, the National Centre for Hydrology and Meteorology (NCHM) employs various tools with differing methodologies to provide daily near-surface temperature forecasts for 20 spatial points. These tools include but are not limited to: global Numerical Weather Prediction (NWP) models, mesoscale NWP models, statistical bias-corrected guidance products, and forecaster consensus (the tools are discussed in more detail in the subsequent sections). However, weather forecasting remains challenging in mountainous topography, hence frequent quality checks and efforts to improve accuracy are important. Currently, NCHM has performed annual verifications on NWP models and consensus forecasts but has yet to quantitatively compare the forecast methods to identify the best-performing tool for product dissemination. This paper aims to instigate such an annual comparative verification routine through this preliminary investigation of the Kalman Filter (KF) temperature guidance.

1.1 Numerical Weather Prediction Models

The modern standard for weather forecasting in most meteorological centres of the world is NWP modelling. NWP models are programs of computer code that solve a mathematical model of the physical atmosphere's initial conditions, dynamics, parameters, and interactions with other earth systems. The first step of NWP, i.e. initialisation, involves the development of a gridded representation of the atmosphere's current state in terms of variables such as temperature, pressure, and humidity, among numerous others.

This is done through grid interpolation of in-situ (surface stations, marine stations, radiosondes, and aircraft observations) and remote (satellites) observations (Thepaut and Andersson, 2010). With this basis, the model then solves a set of nonlinear partial differential equations called the primitive equations for each grid cell (the size of which is determined by the resolution of the model) using finite difference methods or spectral methods (Pielke, 2001). Processes that occur at a scale smaller than the grid's size as well as interactions with other earth systems are resolved using empirical equations, viz. parameterization. The end product of the computation is a forecast value for each variable in each grid cell which is then visualised for interpretation. For example, if we were forecasting temperature for Bhutan at a resolution of 3 km, each 3km by 3km area would have a temperature value which could be mapped as a contour for reference.

With the advent of supercomputers and further advancements in the research of atmospheric physics, current NWP models predict near-surface temperature with great accuracy even at a global scale. For example, in their evaluation of the forecasts from the European Centre for Medium-Range Weather Forecasts (ECMWF), Haiden et al. (2019) found that the 72-hour deterministic two-metre temperature forecasts provided by ECMWF's Integrated Forecast System (IFS) had a Root-Mean-Square Error (RMSE) of 2 K, which is considerably low for a global model. Model accuracy is improved through several approaches such as increasing spatiotemporal coverage of observation data, data assimilation of initial conditions, refining resolution/discretization approach, improving the dynamical core, and fine-tuning parameterization schemes (Schultz et al., 2021). This paper looks at an external method, post-processing, as a prospect for improving temperature forecasts. This revolves around a statistical model that takes NWP forecasts and observation data as inputs to bias-correct the forecast periodically.

1.1.1 Global Models

Based on the domain, i.e. spatial coverage of an NWP model, they can be categorised under global models or regional models. As the name suggests, global models run simulations for the entire globe usually using a spectral method as opposed to finite differences. Regional models, on the other hand, capture a specific local area and account for smaller-scale processes due to their higher resolution. However, regional models are reliant on global models to provide boundary initial conditions, ergo, errors in global models carry over to regional models (Haiden et al., 2019).

At NCHM, several forecast products from global models are used for reference and comparison. Among these, four models are used directly in the form of numeric data: the US's Global Forecast System (GFS), Canada's Global Environmental Multiscale Model (GEM), ECMWF's IFS, and Japan's Global Spectral Model (GSM). The choice of models is largely based on free availability of data and download size/time. This paper focuses on GSM since it is the only global model utilised by the KF guidance at present. The Japan Meteorological Agency's (JMA) GSM model had a horizontal resolution of 20 km before their March 2023 update, after which it was refined to about 13 km (Yonehara et al., 2023). It runs 128 vertical levels and has a forecast range of 132 hours (NCHM only extracts data for the first 72 hours).

1.1.2 Mesoscale Models

Mesoscale models are regional models possessing high enough resolutions (typically 2 to 20 km) to capture mesoscale processes such as vertical circulation caused by convection and topographical factors. One such model is the Weather Research and Forecasting (WRF) model developed by a collaboration between many scientific bodies of the US and currently run operationally at their National Center for Environmental Prediction (UCAR, 2024). It is one of the few open-source models that come with an inbuilt user-friendly customising software, i.e. it allows free installation and modification. The versions installed at NCHM have been configured to cater to Bhutan's meteorological needs in terms of spatial domain and weather pattern schemes. NCHM currently runs two versions of WRF: version 3.4.1 (WRF3) and version 4.3.1 (WRF4); both with a one-way nested domain system with the inner domain used predominantly. They adopt a horizontal resolution of 3 km, 79 vertical levels and a forecast range of 72 hours. The models use GFS data for its initial boundary conditions.

1.2 Consensus Forecast

The weather forecasts disseminated by NCHM at present, particularly the daily temperature forecasts, are a form of consensus forecast. It is a product formulated by combining forecasts from several methods. However, it is more of a qualitative consensus forecast whereby the forecasters refer to various products including NWP models, forecast guidance, and recent observation data. Then, using their extensive knowledge and experience, they make a subjective ‘average’ as the final forecast. This method has been the most effective considering the lack of capacity for probabilistic forecast. This forecast will be referred to in this paper as the ‘final forecast’.

1.3 Kalman-Filter Temperature Guidance

As useful as they are, NWP forecasts have a lot of uncertainty due to the stochastic nature of meteorological processes, the impracticality of having observations at every grid point, and inherent model errors arising from approximations. To reduce these errors in NWP models, guidance produced from the statistical interpretation of NWP and observation data is commonly used in many forecast centres. Most such guidance products are built on Model Output Statistics (MOS) such as the Multiple Linear Regression (MLR) method which statistically relates two or more variables in the following manner:

$$y = c_0 + c_1x_1 + c_2x_2 + \ldots \tag{1}$$

Whereby y is the predictand, c_n are the coefficients and x_n are the predictors (JMA, 2019). MLR is simple and easy to implement, and it was the bias correction method used by JMA operationally till 1996. However, Galanis et al. (2006) states that ‘discrepancies have been found in MOS applications in cases of short time local weather changes or updates of the atmospheric model in use’. Additionally, since the coefficients in Equation 1 are fixed, MLR requires a long set of past data to function well.

To approach this issue, JMA has since switched over to methods that allow ongoing adjustment of statistical equations based on Kalman Filtering. Kalman Filters are a set of equations that computationally solve the least square method using evolving coefficients to minimise errors. The KF guidance at NCHM is a modified version of the one used at JMA. It solves the following equations to find the forecast value $x_{\tau+1}$ at time $\tau + 1$:

$$y_\tau = c_\tau x_\tau + v_\tau \tag{2}$$

$$x\tau{+}1 = c\tau A\tau + u\tau \tag{3}$$

Where y_τ is the predictand, c_τ is the coefficent matrix, x_τ is the predictor matrix, v_τ is the observation noise, A_τ is a matrix describing the evolution of the coefficients and u_τ is the system noise. The salient advantages of this method are the adaptability to fluctuations in observation and functionality with a shorter set of past data (Galanis et al., 2006). Due to its dynamical error correction, KF allows for coping with rapidly changing weather conditions as seen in Bhutan. This juxtaposes MOS which is more appropriate for stable weather patterns.

2 Methodology

2.1 Dataset Preparation

The KF guidance system at NCHM is set up to use R, Python, and GRADS codes to numerically solve Equations 2 and 3. It is automated in a Windows environment using shell scripting. The guidance requires two types of initial datasets: observation and NWP data. NCHM prepares a daily Excel file containing the maximum (Tmax) and minimum (Tmin) temperatures of 20 manual observation stations. These are uploaded to a data storage server accessible to the guidance system.

For NWP data, the guidance extracts GSM, WRF3, and WRF4 outputs. JMA provides GSM data through their “JMA High-Resolution GSM Data Service”: 3-hourly surface data (Pressure, Rain, Wind, Temperature, Humidity, Cloud) up to 5.5 days ahead (00, 06, 12, and 18 UTC initial), and 6-hourly surface data from 5.75 days up to 11 days (00 and 12 UTC initial). Using this, the guidance acquires 3-hourly surface data of 12 and 00 UTC initial, and 6-hourly upper-level data of 12 and 00 UTC initial. These files are then combined into two ‘merged’ files for 00 UTC and 12 UTC saved in the data server. For WRF3 and WRF4 datasets, the models have inbuilt bash scripts to extract only temperature and precipitation data into a GRIB2 file which is automatically uploaded into the aforementioned data server. The guidance picks up the temperature variable from both model datasets and feed it into a single combined Comma Separated Values (CSV) file.

From this amalgamation of observation and NWP data, the guidance takes an assigned combination of temperature values from different sources as its predictors for Equations 2 and 3 during operational use. These combinations of surface and upper-level variables were determined after extensive verification and analysis for different regions.

Before operational use, the guidance requires a ‘development period’ dataset of at least 2-4 months. The guidance statistically interprets this development data, taking NWP variables as predictors and observation data as predictand to calculate the coefficients. These coefficients are then used for forecasting during the operational period where it successively updates each day. The length of operational KF guidance is four months but at the time of this research in June 2024, WRF4 only had data starting January 2024. Due to this limiting factor, the development period was decided to be two months; January-February 2024 and the operational period as March-April 2024.

Accordingly, for these periods, merged files for WRF3, WRF4, GSM, and an integrated WRF4-GSM were prepared for 20 stations, for both Tmax and Tmin, and then ran through the KF guidance to obtain this study’s dataset. Observation data was prepared for points that were forecast by all methods; here, the limiting factor was the final forecast which included only 20 points. Thus, those 20 corresponding locations were chosen for the study (Fig. 1).

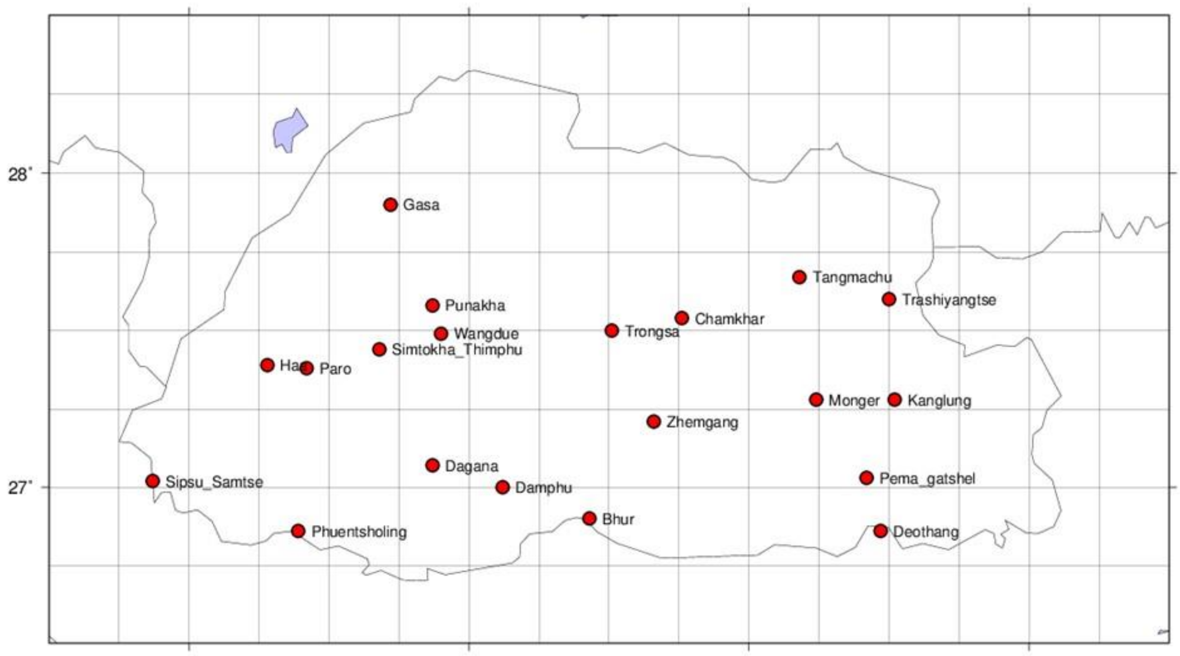

Figure 1: Locations and names of the 20 spatial points used for this research; each corresponds to an observation station

2.2 Statistical Verification

Two simplistic scores were chosen for the verification to garner a concise picture of the methods' performances. For the measure of differences, the RMSE metric was picked since it is commonly used for evaluating forecast accuracy. It calculates the square root of the average of the squared differences between forecast and observed values. Mathematically, it is represented as:

$$RMSE = \sqrt{\frac{1}{n}\sum_{i=1}^{n}(y_i - \hat{y}_i)^2} \tag{4}$$

where y_i is the observed value, $\hat{y}_i$ is the forecast value and n is the number of data points. The closer the RMSE is to zero, the better the model's predictions. Through squaring, RMSE gives more weight to larger errors, hence it is useful in forecast verification where large deviations are a concern. Additionally, it is expressed in the same units as the target variable enabling easier interpretations.

For the measure of dependence, the Pearson Correlation Coefficient (PCC) was chosen. PCC measures the strength and direction of the linear relationship between two variables. It ranges from -1 to 1, where 1 represents a perfect positive linear relationship, -1 represents a perfect negative linear relationship, and 0 indicates no linear relationship. It's widely used in data analysis due to its ease of interpretation and comparison. It is calculated as follows:

$$r = \frac{\sum_{i=1}^{n}(x_i - \bar{x})(y_i - \bar{y})}{\sqrt{\sum_{i=1}^{n}(x_i - \bar{x})^2}\sqrt{\sum_{i=1}^{n}(y_i - \bar{y})^2}} \tag{5}$$

where r is PCC, x_i and $\bar{x}$ are the forecast value and mean of forecasts, y_i and $\bar{y}$ are the observed value and mean of observations, and n is the number of data points.

3 Results

3.1 Average Verification Scores

The verification scores described in Section 2.2 were calculated for the 20 points and averaged to obtain a verification score representative of forecast accuracy in Bhutan as a whole.

3.1.1 Maximum Temperature

RMSE and PCC for Tmax are shown below (Fig. 1 & 2).

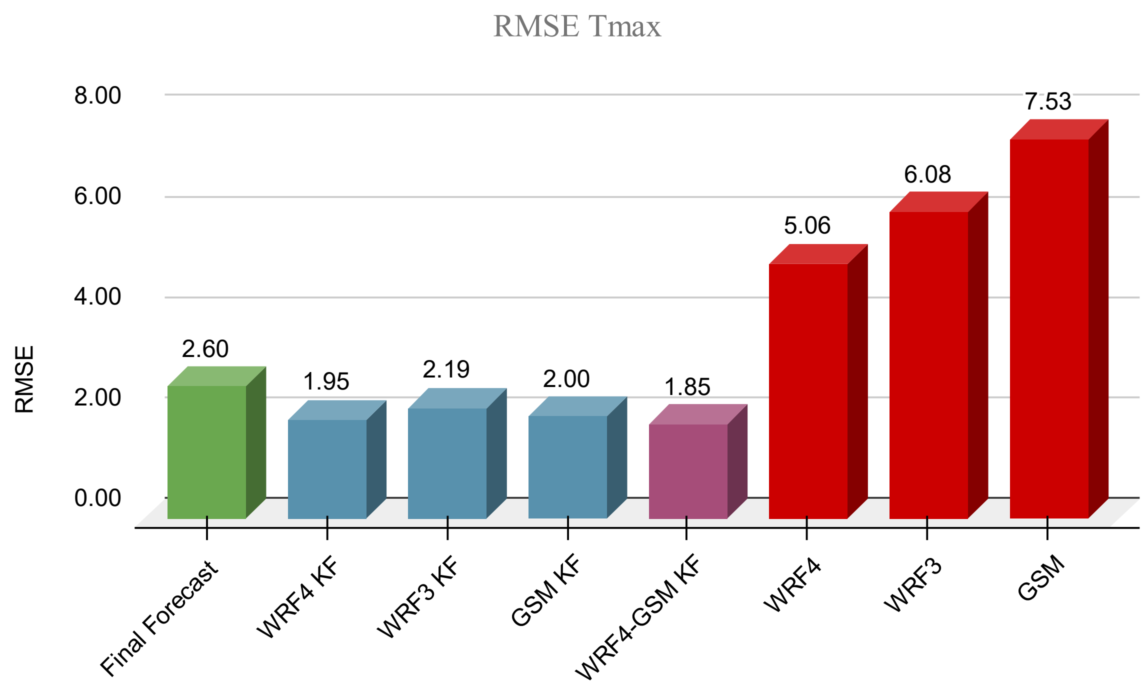

Figure 2: Averaged RMSE for different Tmax forecasts including NWP models, final consensus forecast, and KF guidance; green denotes forecasters' product, blue denotes KF guidance products, red denotes NWP products and purple identifies the best-performing product

The nationally averaged RMSE for March and April of each forecast method investigated by this paper are shown above (Fig. 2). Predictably, the raw NWP model outputs from GSM, WRF4, and WRF3 had relatively high errors. GSM, being a global model, had the highest RMSE value of 7.53 degrees Celsius. In comparison, the mesoscale models WRF3 and WRF4 had 6.08 and 5.06 degrees Celsius RMSE respectively. The final forecast, which is the consensus forecast currently disseminated by NCHM, had an RMSE value of 2.60 degrees Celsius.

All four KF guidances (which use different models) had lower RMSEs with respect to the final forecast, with the WRF4-GSM integrated KF guidance performing the best. Its RMSE value was 1.85 degrees Celsius, signifying a possible 0.75 degrees decrease in temperature forecast error if utilised by NCHM. Interestingly, despite having the highest error, GSM when bias corrected, made better forecasts than WRF3 and was almost as good as WRF4. Suspecting an underlying reason for this due to prior correlation, the three models' PCC to observation data was calculated.

(Fig. 3) shows the PCC values for the three models used for KF guidance. As suggested by the guidance performance, GSM had the highest correlation with a PCC of 0.8035, closely followed by WRF4 and then WRF3.

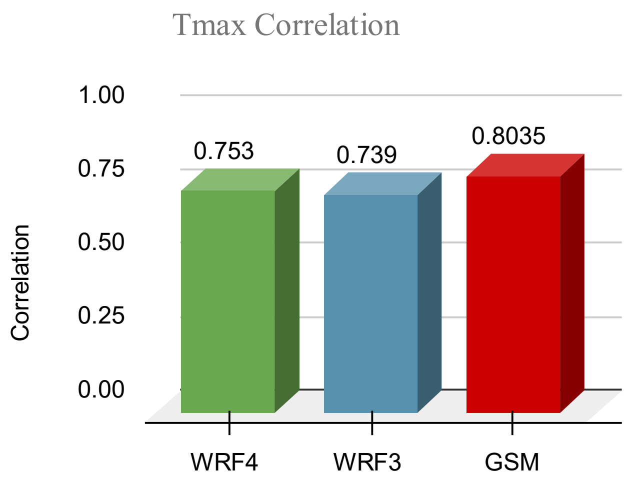

Figure 3: Averaged PCC between NWP model Tmax forecasts and observation

3.1.2 Minimum Temperature

RMSE and PCC for Tmin are illustrated by (Fig. 4) and (Fig. 5) respectively. The results for Tmin concurred with Tmax results. (Fig. 4) shows that the KF guidances had lower RMSEs than NCHM's current forecast with the WRF4-GSM integrated guidance again showcasing the best performance. The only contrast from Tmax results was the better forecasting by GSM guidance as compared to WRF4, signalling a higher correlation of GSM to observation for Tmin than for Tmax. However, as illustrated by (Fig.5), WRF4 had a PCC value higher than GSM. This disproves the hypothesis that GSM guidance had better performance than WRF4 due to a higher correlation with observation.

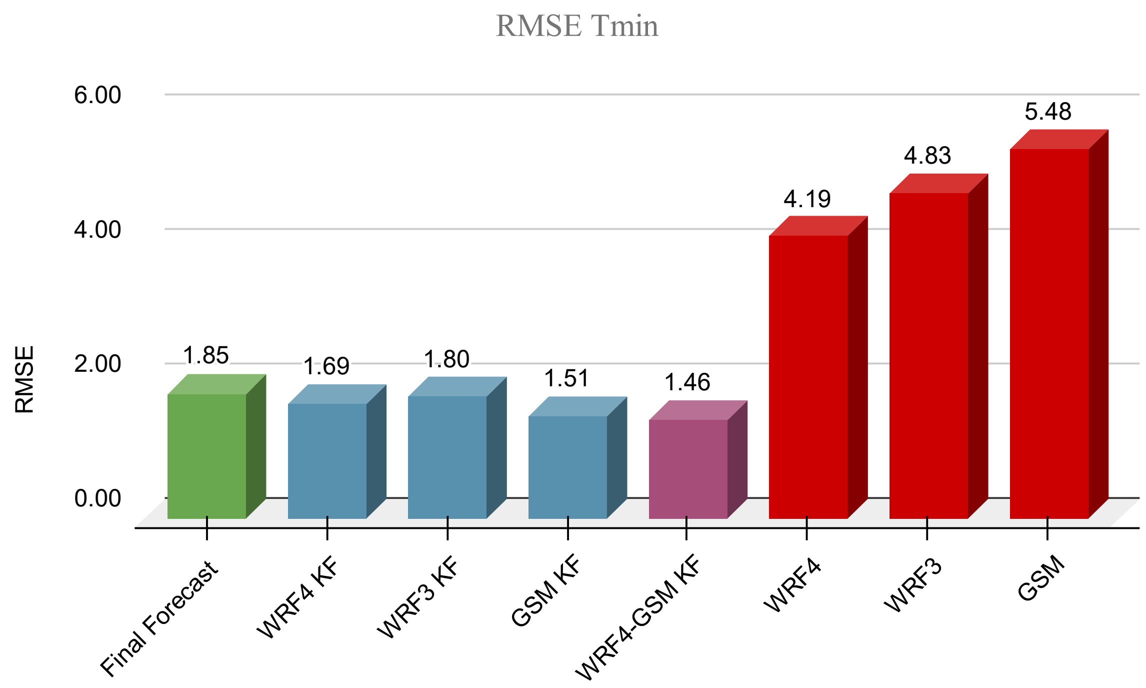

Figure 4: Averaged RMSE for different Tmin forecasts including NWP models, final consensus forecast, and KF guidance

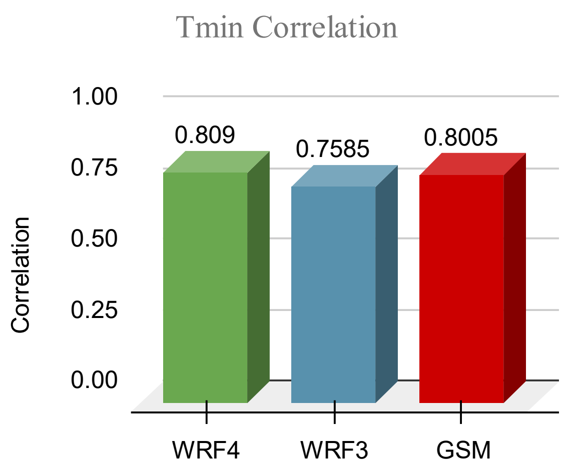

Figure 5: Averaged PCC between NWP model Tmin forecasts and observation

3.2 Point Verification Scores

Having identified the WRF4-GSM KF guidance as the best-performing forecast method for Bhutan as a whole, the regional variability of its performance was investigated by calculating the RMSEs for each point individually.

3.2.1 Maximum Temperature

Tmax RMSE values for each point are shown in (Fig. 1). Generally, the guidance performed better in the Western, Southwestern, and Central areas as compared to the Northern, Eastern, and South-eastern regions. To gauge the underlying cause, analysis was done on the best and the worst performing points, i.e., Tsirang being the best with an RMSE of 1.31 degrees Celsius and Trashiyangtse the worst with RMSE of 3.07 degrees Celsius.

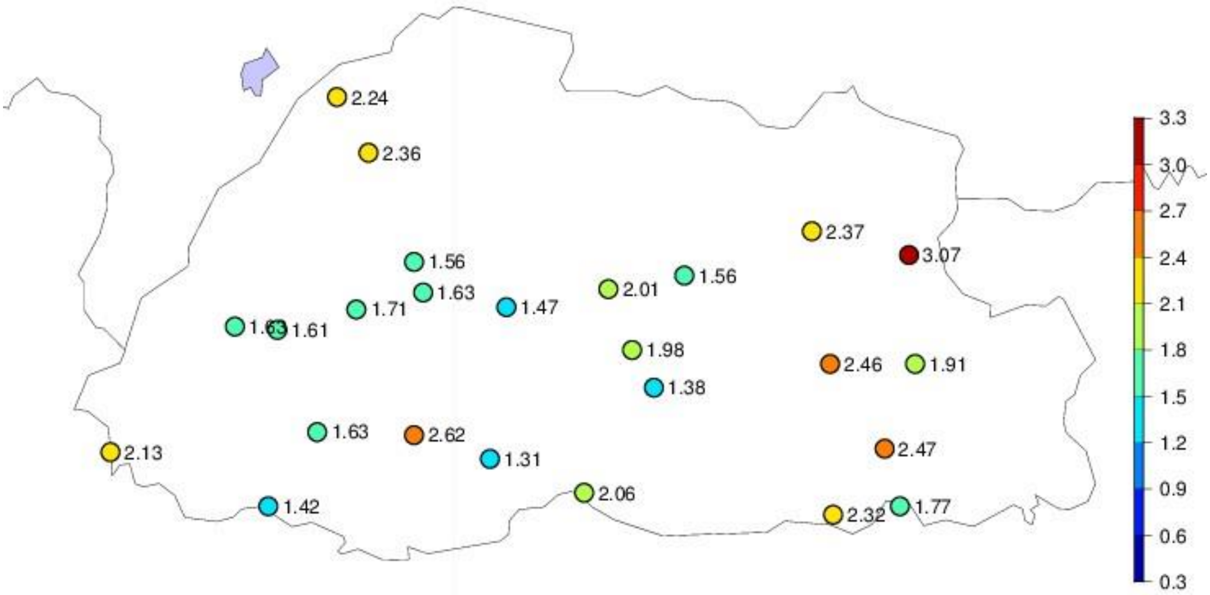

Figure 6: Point RMSE for Tmax forecasts from WRF4-GSM KF guidance

A time series for March and April for Damphu, Tsirang shows simultaneously the Tmax observation value, WRF4 NWP forecast value, and WRF4-GSM guidance value (Fig. 7). The three lines do not stray far from each other which is in alliance with the overall low RMSE. Large day-to-day changes were forecast well by the model and consequently by the guidance as well.

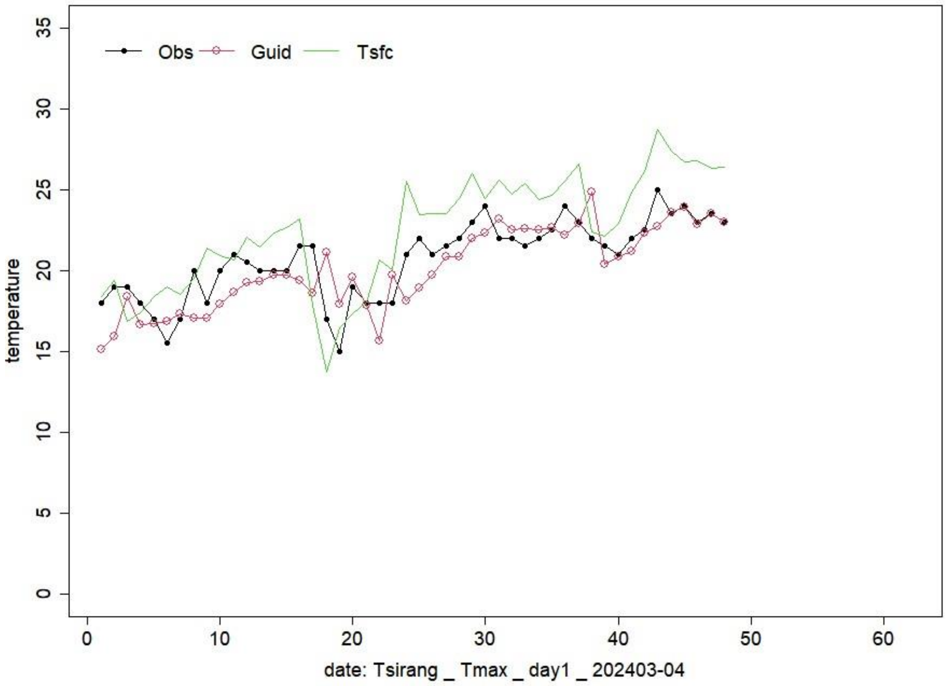

Figure 7: Tsirang daily observed Tmax (black line) as compared to WRF4 (green line) and WRF4-GSM KF guidance (red line) forecasts

Conversely, when looking at an identical time series plot for the worst performing point, Trashiyangtse (Fig. 8), we see the contrary to be true. Drastic day-to-day changes were under-predicted and the magnitude of changes observed were larger than Tsirang's.

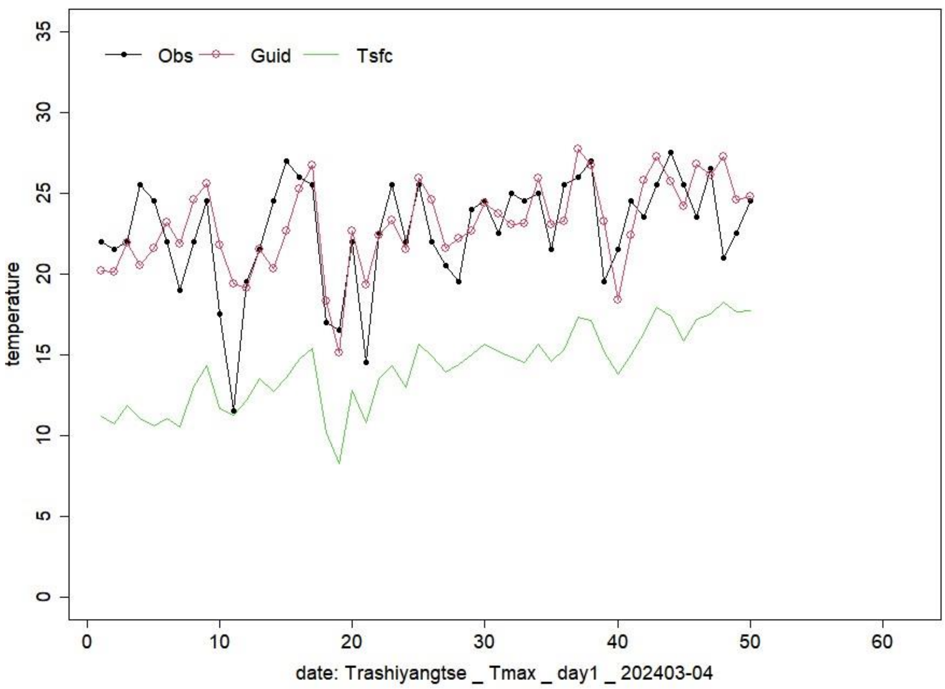

Figure 8: Trashiyangtse daily observed Tmax (black line) as compared to WRF4 (green line) and WRF4GSM KF guidance (red line) forecasts

3.2.2 Minimum Temperature

A similar point analysis was done for Tmin which remarkably showed differing results. As seen in (Fig. 9), the guidance performed better in the Eastern, South-eastern, and South-western regions, whereas the Western, Northern, and Central areas had higher errors. This distribution is almost an antithesis to that of Tmax as described under Section 3.2.1.

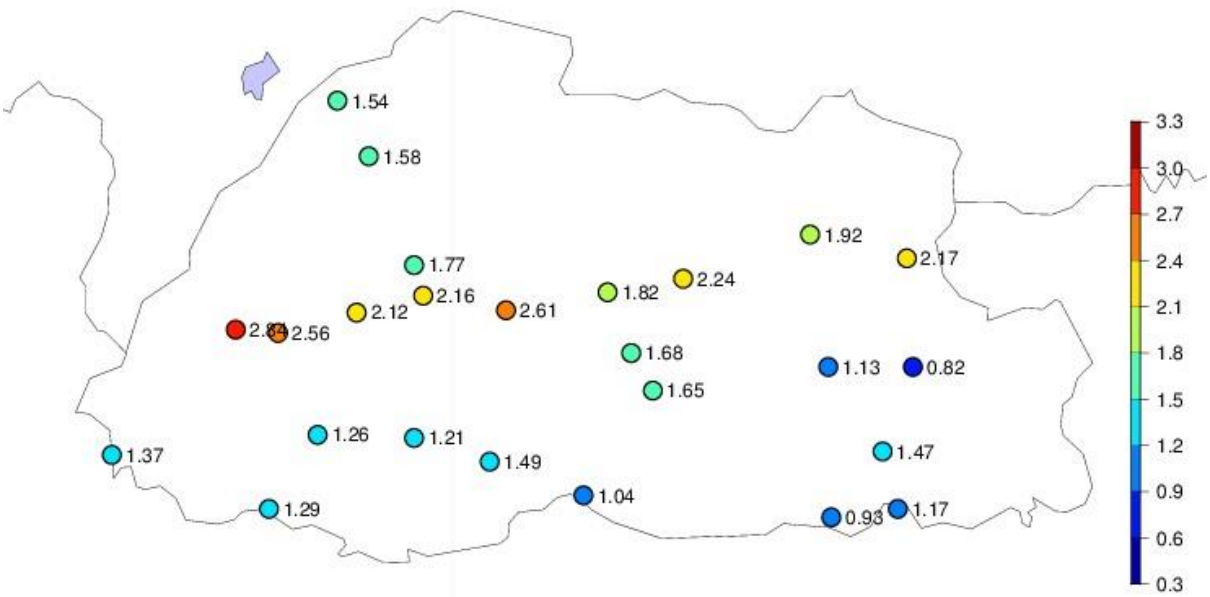

Figure 9: Point RMSE for Tmin forecasts from WRF4-GSM KF guidance

Notably, the best performing point in this case was Kanglung, Trashigang in the East with a low RMSE of 0.82 degrees Celsius. Looking at the time series, the relative lack of large dips and rises in temperature is most conspicuous (Fig. 10).

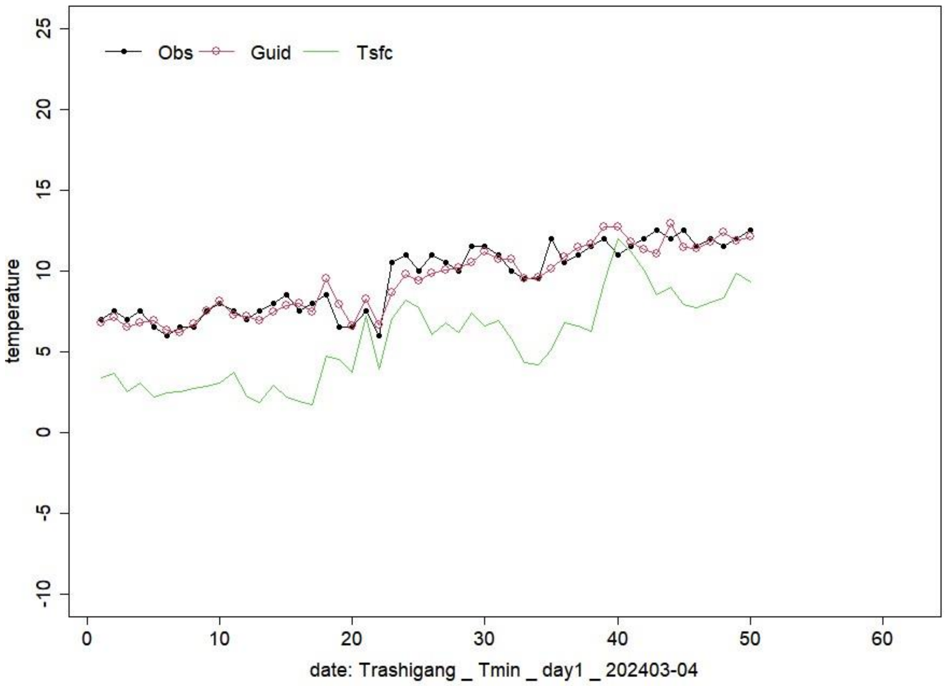

Figure 10: Trashigang daily observed Tmin (black line) as compared to WRF4 (green line) and WRF4GSM KF guidance (red line) forecasts

On the other hand, the worst performing point, Haa in the West, had an RMSE of 2.84 degrees Celsius. Expectedly, the time series plot for Haa (Fig. 11) demonstrates radical changes in daily Tmin.

However, it is worth noticing, qualitatively from the four time-series figures, that the KF guidance seems to be capable of handling daily changes within 5 degrees Celsius but has difficulty when it fluctuates more than that. So, it can be theorised that the guidance has issues with predicting the magnitude and not the event itself.

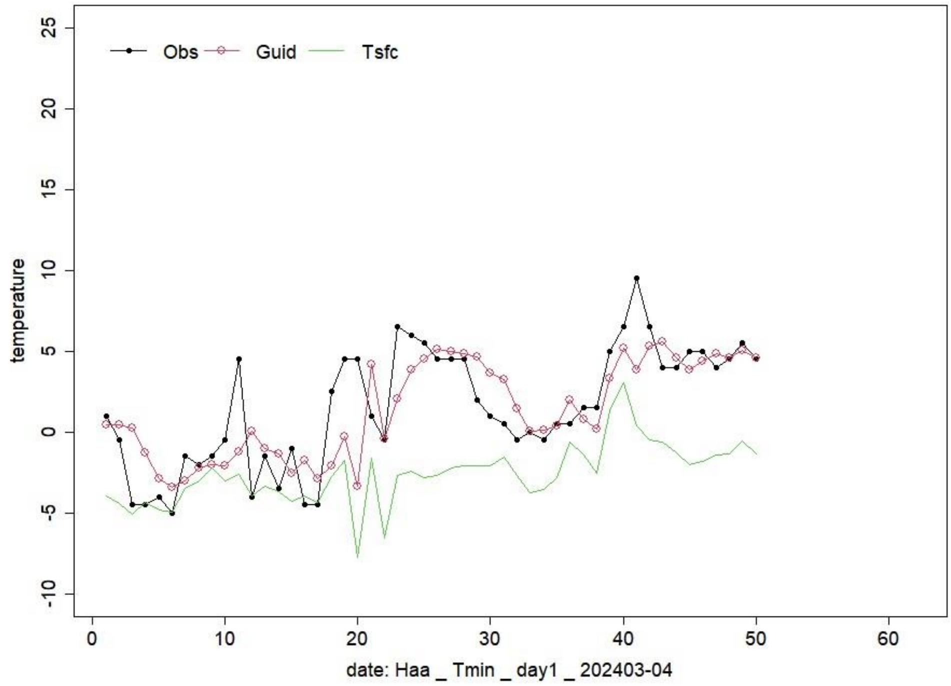

Figure 11: Haa daily observed Tmin (black line) as compared to WRF4 (green line) and WRF4-GSM KF guidance (red line) forecasts

4 Discussion

WRF4-GSM KF guidance had the lowest error for both Tmax and Tmin, proving to be better than NCHM's current final forecast (Fig. 2 and Fig. 4). This insinuates an improvement in NCHM's forecast accuracy if the KF guidance usage is implemented, confirming the efficacy of Kalman Filtering near-surface temperature forecasts in Bhutan. Additionally, because all four KF guidances performed better than the final forecast, it opens the possibility of a KF guidance probabilistic forecast as well. Another thing worth noting is that the newly operational WRF4 does better temperature forecasting than WRF3; this information is useful since standalone verification of WRF4 has not been done yet. These findings share a likeness with those of Sasaki et al. (2020) in Vietnam who also found the KF guidance performing better than their existing products.

When it came to PCC, it was interesting how some NWP models, namely GSM, underperformed by themselves but did better than other models once bias-corrected (Fig. 3 and Fig. 5). An analysis of PCC for the models showed that despite GSM's high RMSE, it had a higher PCC with observation. Therefore, once the systematic bias was corrected, it performed well. This indicates a need for considering correlation in addition to RMSE when planning to incorporate new models into the guidance system in the future. However, it is important to know this is not true for every case, as shown in Section 3.1.2 whereby GSM KF guidance had lower errors than WRF4 but also a lower PCC. Thus, there must have been a confounder variable somewhere causing this effect, the investigation of which is outside the scope of this particular study.

From the point verification in Section 3.2 (Fig. 6 and Fig. 9), it was shown that spatial variability in error does not display any logical pattern that could be corrected easily. However, it was interesting to see a complete contradiction between Tmax and Tmin; areas with low errors for Tmax had high errors for Tmin and vice versa. It could signal an inverse proportionality between Tmax and Tmin forecast accuracy, ergo between day and night temperatures. Detailed investigation of the diurnal effect on weather predictability could be the subject of future research.

Finally, through time-series analyses of the best and the worst performing points (Fig. 7, Fig. 8, Fig. 10, and Fig. 11), two factors contributing to accuracy were identified: smoothness of data and adaptability of the KF guidance. Low error points showed a steady daily change in temperature easily predicted by the KF guidance. High error points had huge daily changes in temperature uncaptured by the KF guidance. This suggests that the efficacy of KF guidance is reliant on its ability to capture extreme changes in temperature. However, it is worth noting that the high error points show massive and sudden daily changes of more than 10 degrees Celsius. Such variations in Bhutan are unlikely to occur as frequently as shown by some observation data. A study by Zhou et al. (2020) showed that day-to-day temperature changes of 10 degrees Celsius or more are classified as extreme events and in South Asia, occur only once or twice a year. Even in the central plains of the USA with the highest occurrences, it only happens about 10 times a year. Therefore, the quality of observation data is worth studying, and if it is indeed correct then the cause of such drastic changes could be interesting to investigate.

It is important to state that this study only serves as a preliminary investigation, and more substantial testing is necessary for the full implementation of the KF guidance for operational forecasting. This study was limited in spatiotemporal coverage; it considered only 20 points in Bhutan to represent it and used a two-month period. Although NWP and guidance outputs can be extracted for every gridpoint spaced by the model's resolution, the number of points usable is limited by observation data and the final forecast. Nevertheless, future studies could expand on this since Bhutan has a very complex topography that demands fine-scale delineation. Consideration of automatic weather stations is a viable avenue for this. On the other hand, the time period investigated was limited due to a lack of WRF4 data which is a huge caveat of this study; any seasonal variation of errors was completely overlooked which could hold important findings. WRF4 has been set up to store all future data, therefore follow up verification after a year of accumulation would be useful. Furthermore, only two statistical metrics were used to verify the forecasts, which had their pros but also contras: RMSE does not provide information on the direction of error which would be critical for bias correction, PCC assumes normal distribution, and the study did not include a measure of dispersion for that matter. Additionally, statistical significances of the metrics were not considered due to the preliminary nature of the study. Future work could incorporate more verification scores for a robust analysis such as absolute error (provides directional information about the errors), Spearman's rank correlation (does not assume normal distribution), and perform tests to ensure the results are statistically significant, i.e. does not arise from random chance.

5 Conclusion

While NWP models such as GSM and WRF provide valuable forecasts, their inherent uncertainties necessitate post-processing methods for better precision. NCHM's current consensus forecast combines multiple sources using qualitative judgment. The Kalman Filter (KF) guidance offers a promising improvement by dynamically adjusting forecast errors through evolving coefficients. Unlike traditional MOS methods, KF requires less historical data and adapts effectively to rapidly changing weather conditions, making it suitable for NCHM's use.

The results of this study confirmed that Kalman Filtering NWP temperature forecasts is effective for Bhutan. The KF guidance products have RMSEs lower than all current existing forecast methods at NCHM. Additionally, they can be further improved by quality-controlling observation data, investigating high error events, and through routine verification and maintenance. By implementing KF guidance, NCHM can not only improve its temperature forecast accuracy but also assure consistency and objectivity through automated corrections. The increased accuracy will be useful for all product users but especially so for stakeholders who utilise gridded data as input for their own models and/or analyses.

Any follow-up verification of forecast methods could take into account more forecast points, consider longer periods, and explore more apt verification scores. Future possibilities of producing probabilistic forecasts using outputs from different guidances could be explored as well.

6 Author Contributions

Dechen Lhamo Gyeltshen: Software, Investigation, Analysis, Visualization, Writing - Original Draft. Kiichi Sasaki: Conceptualisation, Methodology, Software, Writing - Review & Editing. Singay Dorji: Supervision, Writing - Review & Editing. Pema Syldon: Writing - Review & Editing.

7 Acknowledgements

The present work was carried out in the framework of the Japan International Corporation Agency (JICA) Technical Corporation Project (TCP) Phase II: Capacity Enhancement of Meteorological Observation, Forecasting and Flood Warning, for disaster preparedness and response in Thimphu and Paro River Basins which started operation in March 2020. The development and use of the Kalman Filter temperature forecast guidance is one of the main activities of Output 2 of the JICA Project to improve the forecasting services of NCHM.

References

Galanis, G., Louka, P., Katsafados, P., Pytharoulis, I., and Kallos, G. (2006). Applications of kalman filters based on non-linear functions to numerical weather predictions. *Annales Geophysicae*, 24(10):2451– 2460.

Haiden, T., Janousek, M., Vitart, F., Ferranti, L., and Prates, F. (2019). Evaluation of ecmwf forecasts, including the 2019 upgrade.

JMA (2019). Nwp application products. https://www.jma.go.jp/jma/jma-eng/jma-center/nwp/nwp-top.htm. [Accessed 18-09-2024].

Pielke, R. (2001). *Mesoscale Meteorological Modeling*. ISSN. Elsevier Science.

Sasaki, K., Anh, V., Hang, N., and Trang, D. (2020). Development of maximum and minimum temperature guidance with kalman filter for 63 cities in vietnam up to 10 days ahead. *Journal of HydroMeteorology*, 5:51–64.

Schultz, M. G., Betancourt, C., Gong, B., Kleinert, F., Langguth, M., Leufen, L. H., Mozaffari, A., and Stadtler, S. (2021). Can deep learning beat numerical weather prediction? *Philosophical Transactions of the Royal Society A: Mathematical, Physical and Engineering Sciences*, 379(2194):20200097.

Thepaut, J. and Andersson, E. (2010). The global observing system. *Data assimilation: making sense of observations*, pages 263–281.

UCAR (2024). Weather research and forecasting model (wrf). https://www.mmm.ucar.edu/models/wrf. [Accessed 17-09-2024].

The Met Office (2025). The Unified Model. https://www.metoffice.gov.uk/research/approach/modelling-systems/unified-model. [Accessed 13-03-2025].

Yonehara, H., Kuroki, Y., Ujiie, M., Matsukawa, C., Kanehama, T., Nagasawa, R., Ochi, K., Higuchi, M., Ichikawa, Y., Sekiguchi, R., et al. (2023). Upgrade of jma's operational global numerical weather prediction system. *WGNE Res. Activ. Earth Syst. Modell*, 53:6–15.

Zhou, X., Wang, Q., and Yang, T. (2020). Decreases in days with sudden day-to-day temperature change in the warming world. *Global and Planetary Change*, 192:103239.

Generation of Digital Terrain Models Using LiDAR equipped UAVs: Techniques and Applications, a case study in Chamkharchhu basin.

Tandin Wangchuk[1], Jamyang Zangpo[2], Chimi Namgyel[3]

[1,2,3] National Centre for Hydrology and Meteorology

Correspondence: tandinw@nchm.gov.bt

Abstract

The Digital Terrain Models provide a detailed representation of the earth's surface that has a wide range of applications. An accurate representation of the ground surface is essential for flood modeling as the model's performance is highly dependent on the DTM's accuracy. The UAV-LiDAR systems can capture and identify small topographical features like buildings, bridges, walls, vegetation, etc., which can have a substantial influence on flood pathways and flood travel time. The study explores the method involved in DTM generation from a UAV equipped with a LiDAR sensor. The paper then details a case study in the Chamkharchhu basin, where the UAV-LiDAR system was used to generate a highly accurate DTM, demonstrating its applicability in flood hazard mapping and other geospatial applications. A comparison of simulated results from two terrain sources is also presented. The simulated results demonstrate the significant influence of DTM accuracy in flood depth and the inundation extent, which affirms the use of high-resolution terrain models, especially in small-scale flood modeling studies.

1. Introduction

Digital Terrain Models (DTMs) are important tools in geography, environmental science, urban planning, and civil engineering because they provide detailed representations of the Earth's surface, allowing for precise spatial analysis, mapping, and decision-making (Muhadi et al., 2020; Ozdemir et al., 2013; Raber et al., 2007; Tsubaki & Fujita, 2010). DTMs have traditionally been constructed using technologies like ground surveying, satellite imagery, and aerial photogrammetry (Udin & Ahmad, 2014), all of which have limitations in terms of cost, accessibility, coverage, and accuracy. In recent years, the development and deployment of Unmanned Aerial Vehicles (UAVs) has revolutionized the process of DTM generation and its application, making it.

UAVs, commonly known as drones, offer a flexible and cost-effective solution for capturing high-resolution spatial data. Equipped with advanced sensors like RGB cameras and LiDAR, UAVs can operate in diverse environments and provide real-time data acquisition, which is particularly beneficial for dynamic and inaccessible terrains (Manfreda et al., 2018). LiDAR-equipped UAVs, although relatively expensive, streamline the field data acquisition and provide higher spatial resolution in which ground surfaces are represented better with high-density and high-accuracy ground points (Liu, 2008; Shahbazi et al., 2014). The desired spatial resolution and positional accuracy the UAV-based DTMs provide can be used for various studies and applications (Jiménez-Jiménez et al., 2021).

DTM, in general, has a wide range of applications, from obtaining mountain topography to studying glacial geomorphological changes, slope mapping to flood damage assessment, and so on. Also, DTMs produced through UAV technology provide an accurate representation of the ground with the most recent land use changes and developmental activities, which is essential for understanding and mapping high flood-risk areas and inundation extents. One of the compelling advantages of UAV with LiDAR technology over photogrammetry is its ability to penetrate the canopy and acquire ground data (Liu, 2008) although the presence of vegetation must be classified and processed accordingly. Another advantage of UAV is its ability to generate RBG values for each collected data point, which enables users to identify ground features with positional data (Furby & Akhavian, 2024).

The accuracy of the DEMs generated from UAVs can differ substantially depending on the type of UAV and the use of different sensors. Although the positional accuracy of the data is generally driven by the use of ground control points (GCPs) and RTK integration, the ability to gather detailed ground features depends on the sensor choices.

This study investigates the methodology involved in creating DTMs with UAVs, concentrating on procedures, accuracy, and application. By utilizing UAV technology, researchers and practitioners can overcome many of the problems associated with standard DTM generation techniques. The paper will go over the full workflow, from data collection to processing and accuracy evaluation, emphasizing the innovations and advances that UAVs bring to the sector. In addition, we will look at the practical application of UAV-generated DTMs, demonstrating their potential to improve decision-making processes in sectors such as flood hazard assessment and disaster management through a case study.

2. Methodology

2.1. Study Area

The satellite-based Digital Elevation Models (DEMs) with varying spatial and temporal resolutions (ranging from 10 m to 30 m) are freely available. They are extensively used for land use planning, glaciers and glacial lake mapping, infrastructure planning and development, flood forecasting and mapping, and flood damage assessments. The intricate mountainous terrain with dense vegetation often results in satellite-based, freely available DEMs failing to represent the ground features accurately, which is especially true in Bhutan. The UAV survey in such an environment bridges the gap and ensures better ground representation in digital elevation models through isolated aerial surveys.

The UAV survey was carried out in major settlement areas of the country that were impacted by flood hazards in the past and where there is potential flood risk in the future. This paper focuses on the Chamkharchhu basin of the Bumthang district in central Bhutan. The Chamkhar town (Fig. 1), which lies along the flood plains of Chamkharchhu, is regarded as highly vulnerable to rainstorm floods and Glacial Lake Outburst Floods (GLOFs) due to its low elevation and settlements being concentrated along the river banks. The Bathpalathang domestic airport (shown in Fig.1), located upstream of Chamkhar town, is also highly vulnerable to flooding. The 2009 Cyclone AILA brought heavy rain to the country, causing significant flooding in the area where farmlands along the flood plains were inundated due to swollen rivers.

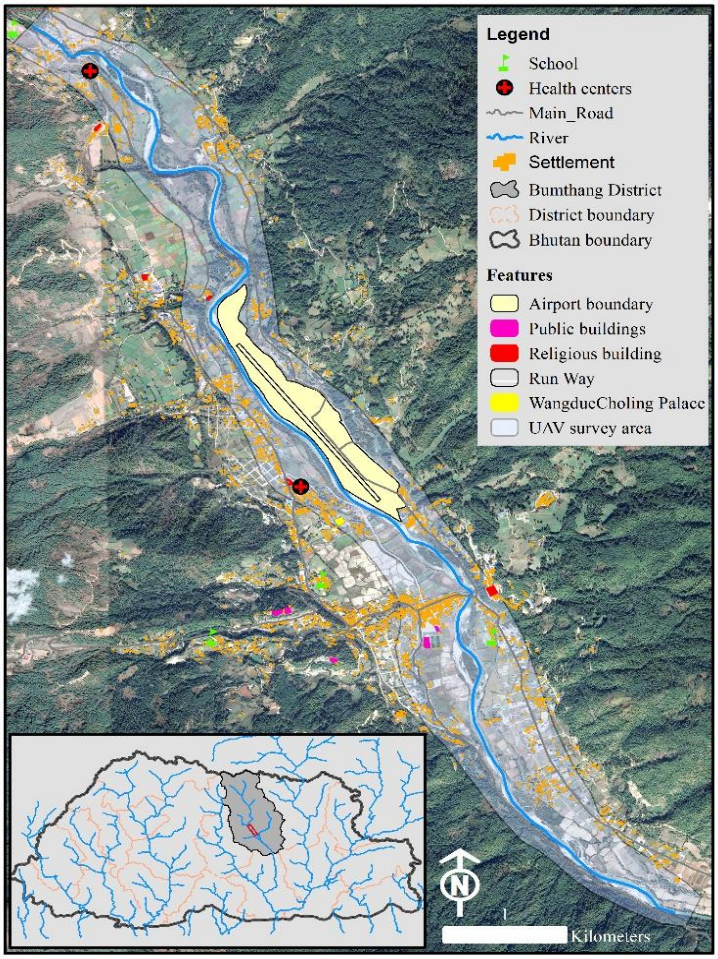

Fig. 1. Study area: Chamkhar valley, Bumthang

2.2. UAV and Equipment

The selection of the type of UAV platform depends on the user's end objectives, data requirements, and payload capability. Both fixed-wing and multicopter UAV platform has their own merits and demerits owing to their applications, site conditions, and weather conditions. For low-altitude flights that collect finer surface details and relatively small area coverage, multicopters are a better choice as they can take off and land on a small space (Jiménez-Jiménez et al., 2021).

For this study, a DJI Matrice 300 RTK equipped with a LiDAR sensor (Zenmuse L1) was used for data collection. The DJI Matrice 300 (M300) is a versatile and advanced drone platform that supports a wide range of applications, including aerial inspection, surveying, and mapping. One of its key features is its compatibility with Real-Time Kinematic (RTK) technology, which significantly enhances its positioning accuracy. The RTK technology is used to enhance the precision of satellite navigation by using a network of fixed ground stations that provide real-time corrections to the drone's onboard GPS. The integration of RTK with the DJI M300 significantly enhances its capability for high-precision applications. By reducing positional errors to the centimeter level, RTK enables the M300 to perform complex tasks with greater accuracy and reliability, making it a powerful tool for DTM generation.

For the RTK integration, the drone is connected to the Trimble GNSS R10 (base station) which relays the real-time accurate ground positions to the drone for its positional accuracy as shown in Fig. 2. The GNSS base stations used for this study are marked in Fig.1. Using RTK-equipped UAV foregoes the need to lay Ground Control Points (GCPs) but the overall accuracy is expected to be slightly less (Štroner et al., 2020). For vegetated and large areas, laying GCPs can be tedious, and the workflow is considerably faster when GCPs are not used. For the areas where the use of GCPs is not feasible, the use of multiple GNSS fixed base stations can be used to acquire differentially corrected geolocation of the images with very high accuracy (Martínez-Carricondo et al., 2023).

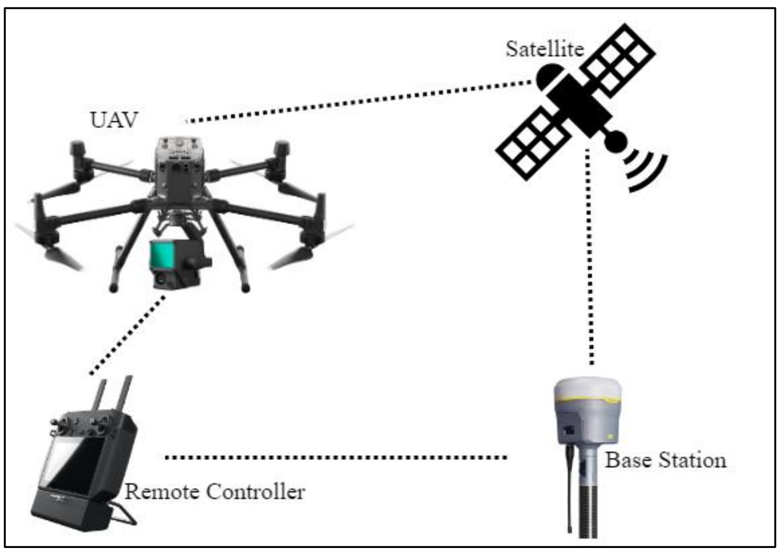

Fig. 2. RTK integration schematic with GNSS base station for UAV survey

2.3. Data Acquisition and Mission Planning

The images used in this study were obtained using Zenmuse L1, a LIDAR sensor with an RBG camera, which is an ultimate solution for aerial surveying. The mission planning was carried out in the DJI Pilot 2 app built with the remote controller (RC). Proper integration of RTK with the RC and UAV is essential to ensure accurate geolocation of images and for post-processing workflow. The operation of UAVs in

Bhutan requires permission from the Bhutan Civil Aviation Authority (BCAA), and the flight altitude is limited to 90 m above the ground level (Bhutan Civil Aviation Authority, 2017). The flight paths in each mission are parallel with constant forward and side overlaps and the camera is oriented vertically (90 deg angle) as shown in Fig. 4. The coverage area, camera location, and flight paths are presented in Fig.3. A total area of approximately 6.8 km^2 was covered by the aerial survey which includes all the major settlements in the Chamkharchhu river basin, from Kurjey (upstream) to Jalikhar (downstream).

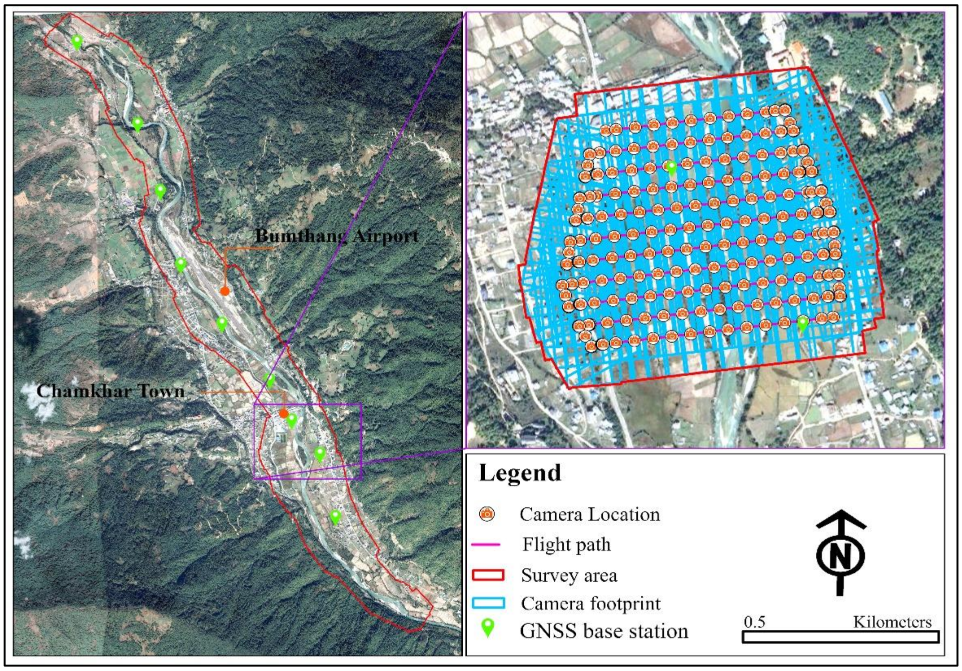

Fig. 3. Flight path and camera location of UAV survey

The flight parameters (altitude, overlap, flight speed) and the LiDAR settings (point cloud density, ground sampling distance (GSD), etc.) are presented in Table 1. The scanning mode of the LiDAR is set to repetitive and single return mode with a sampling rate of 240 KHz and RBG coloring.

Table 1. Flight parameters and sensor settings

Sl.no	Flight/sensor parameters	Values
1	Flight altitude (m)	90
2	Flight speed (m/s)	10
3	Overlaps (side)-LiDAR (%)	70
4	Overlaps (forward)-LiDAR (%)	70
5	Point cloud density (points/m^2)	290
6	GSD (cm/pixel)	4.09

A total of 3250 images were collected from 12 flight missions with nine ground base stations. The photos, along with the RTK files, are extracted for further data processing and DTM generation.

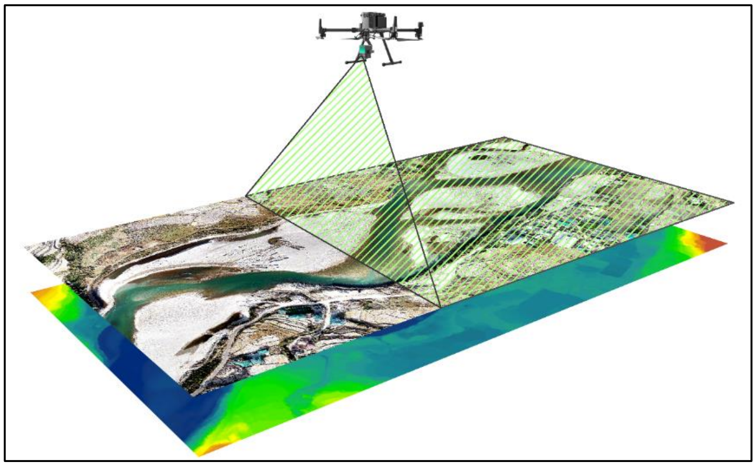

Fig. 4. Aerial survey approach set up using DJI M300 equipped with LiDAR sensor

2.4. Data Processing

Generating a Digital Terrain Model (DTM) using UAV LiDAR data with DJI TERRA and Metashape involves a detailed and precise workflow that leverages the strengths of both software platforms. Fig. 5 presents a generalized workflow of the UAV data processing from DTM generation using DJI TERRA and Agisoft Metashape.

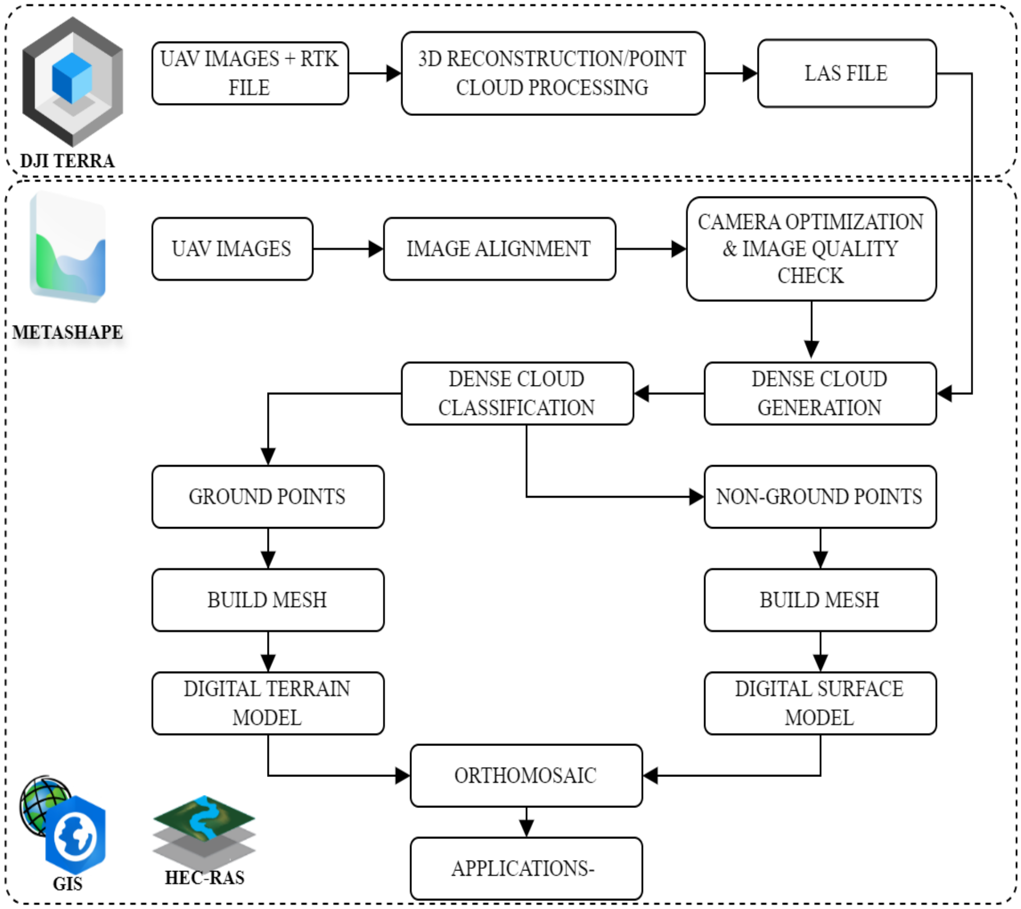

Fig. 5. Generalized UAV data processing workflow adopted for this study

The flight planning and flight parameter setup were carried out in the DJI Pilot 2 app with desired point cloud density and GSD for acquiring high-resolution LiDAR data. The raw LiDAR data is processed in DJI TERRA to create accurate point clouds, ensuring precise georeferencing and alignment. This software generates realistic 3D models and point clouds from photos, which can then be exported to common formats for image reconstruction based on the objectives as shown in Fig.6. This preliminary processing is crucial for filtering out noise and unwanted data points. This process converts proprietary LiDAR (.LDR) to a more usable format (.las), which can be used for processing in Metshape, GIS, and other data processing software.

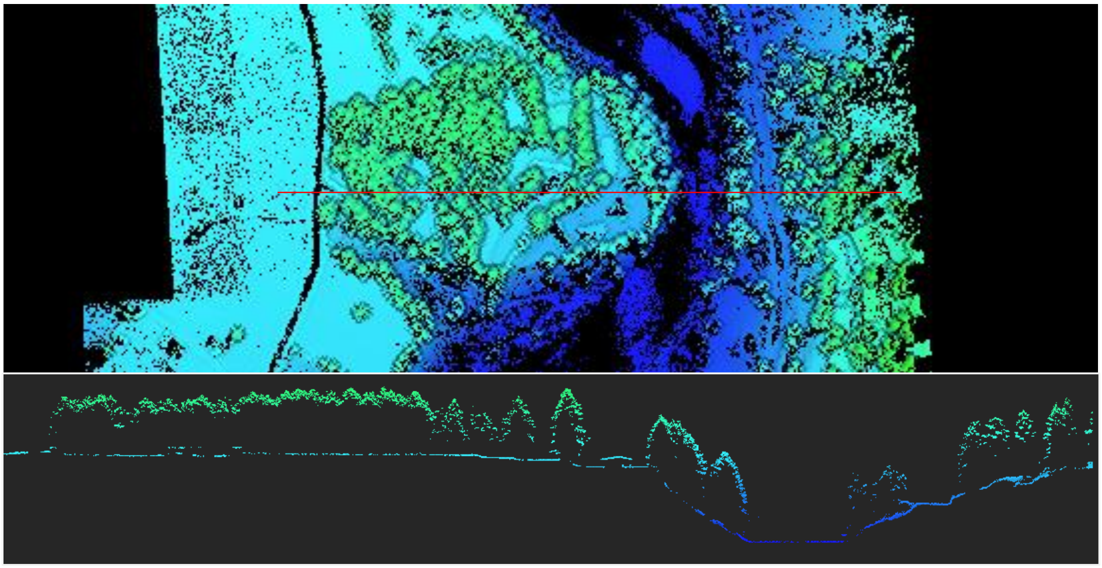

Fig. 6. LiDAR point cloud processing in DJI TERRA (top) and sectional view of the terrain with clear line of vegetation and ground (bottom).

Once the point cloud data is prepared, it is exported to Metashape, which excels in advanced photogrammetry and 3D modeling. In Metashape, the point clouds are further refined, and algorithms are applied to classify ground points, removing vegetation, buildings, and other non-ground elements. This classification is essential for generating a true representation of the terrain. The filtered ground points are then used to create a detailed and accurate DTM, while the unclassified points are used for generating DSM with varying resolutions, as shown in Table 2. The products generated after processing in Metashape are presented in Fig. 7. The spatial resolution of the generated products can vary depending on the user's requirements, although GSD can play a vital role in that aspect.

Table 2. Summary of products generated in Metashape

Area surveyed (km^2)	Georeferencing method	Cameras Total/aligned	Dense cloud points (number)	Orthomosaic/DTM resolution (cm)
6.8	RTK	3250/3250	357,455,725	4.1/12.5

The integration of DJI TERRA and Metashape ensures high-quality geospatial products such as DTM, DSM, and Ortho mosaic, facilitating applications such as topographic mapping, land-use planning, environmental monitoring, and hydrological modeling.

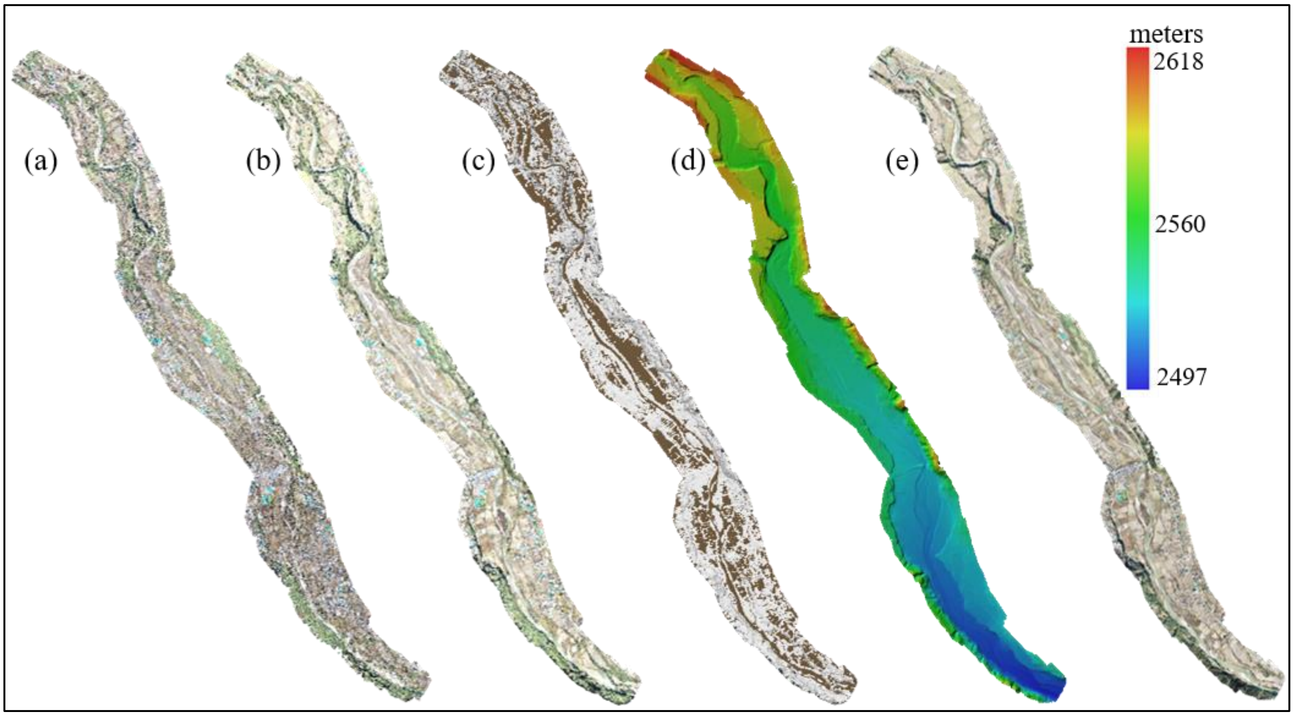

Fig. 7. Products generated from Agisoft Metashape using UAV image and LiDAR data ((a) Sparse cloud, (b) Dense cloud, (c) Dense cloud classification, (d) Digital Terrain Model, and (e) Ortho mosaic).

2.5. Accuracy Assessment

The direct georeferencing capabilities of UAVs equipped with GNSS RTK forego the need to use GCPs. Several studies (Harwin et al., 2015; Martínez-Carricondo et al., 2023; Taddia et al., 2020; Žabota & Kobal, 2021) have demonstrated the methods to assess the accuracy of the geospatial products generated from UAV images. A more detailed assessment using GCPs compiled by (Jiménez-Jiménez et al., 2021) emphasizes the importance of GCP distribution and the number of GCPs recommended for the size of the survey area and terrain morphology. In this study, a simpler approach is adopted where the ground GNSS station data are used to georeferenced the products generated; for more comprehensive assessment, GCPs are required to validate it.

3. Results

3.1. Generation of Digital Terrain Model and Ortho mosaic

The DTM is generated from the classified point cloud where vegetation and man-made structures are removed. The images are georeferenced with the differential position acquired from the GNSS base stations. The DTM, Digital Surface Model (DSM), and Orthomosaic obtained in this study are presented in Fig.8. The DTM generated in this study captures highly accurate geological features and recent land use changes along the river and riparian settlements. In DTM, all the structures and vegetation are removed, and a bare earth model is presented, while DSM contains all of these features (Fig. 7b, c).

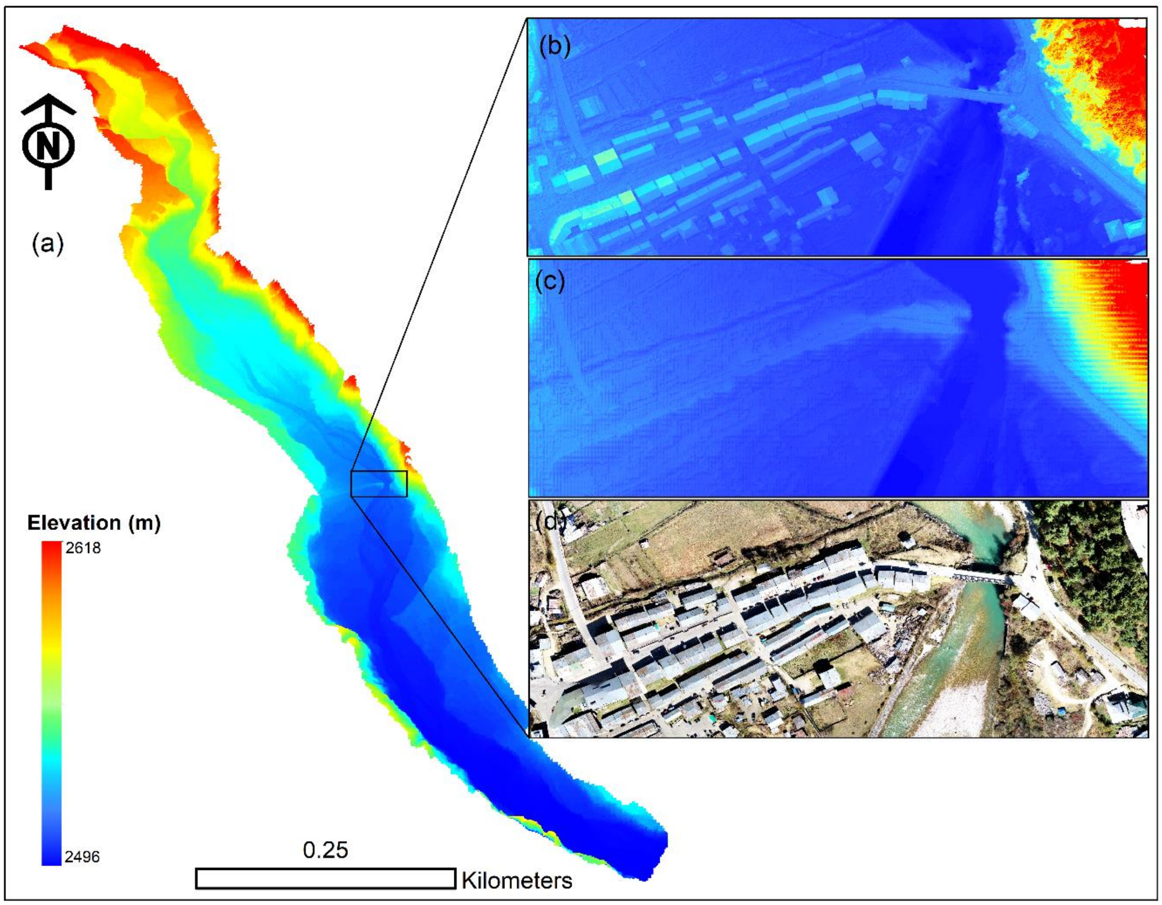

Fig. 8. Different models generated from LiDAR-equipped UAV: (a) 3D model of DTM for study area, (b) DSM, (c) DTM, and (d) Orthomosaic of Chamkhar town

The DTMs and Orthomosaic are extracted for further application in flood hazard mapping at a spatial resolution of one meter. A detail use of DTM for flood analysis and mapping is discussed in section 4.

4. Application of UAV-derived DTMs for Flood Hazard Mapping

4.1. Review of related studies

The digital terrain models have a wide range of applications, as described in the earlier sections of this paper. The application of LiDAR-equipped UAV-derived terrain models is seen as a fundamental input for hydrologic and hydraulic models as the accuracy of terrain models affects the modeling results (Muhadi et al., 2020). Various studies (Casas et al., 2006; Jakovljevic et al., 2019; Muhadi et al., 2020; Sampson et al., 2016; Trepekli et al., 2022) has demonstrated the use of terrain models derived from UAVs and LiDAR-equipped UAVs for hydrological modeling and, in particular, flood hazard mapping with highly accurate results.

Open-access global digital elevation models like AW3D, SRTM, and ASTER have been commonly used for flood modeling purposes, but the results rarely represent the ground reality due to inherent bias in such elevation models. Courty et al., 2019 compared the flood modeling simulation results from such global models with the LiDAR-derived DTM and concluded that the performance of DTM is closest to reality. An accurate representation of terrain is critical to leverage the information generated from flood modeling for vulnerability identification and risk mitigation. A LiDAR-based UAV-derived DTM can produce high-resolution and more accurate flood hazard maps for better decision-making and flood disaster management (Puno et al., 2018).

The topographical changes that occur due to river flow path alteration and changes in land use, largely due to past flood events and urbanization are essential to understand flood risk in the future. The global digital elevation models rarely capture these changes due to their low temporal and spatial resolution which makes it obsolete for its use in small-scale flood hazard and risk assessment.

4.2. LiDAR DTM for flood hazard mapping in Chamkharchhu

The present study assesses its application through a case study, where a flood hazard assessment of the study area (Chamkharchhu) is carried out. The spatial resolution of the DTM used in this case study is one meter in both directions to reduce the computational time during the analysis and modeling. Hydrologic Engineering Centers Flood Analysis Software (HEC-RAS) is a commonly used hydrodynamic model that allows users to perform 1D and 2D flow simulations for flood hazard assessment (Brunner & CEIWR-HEC, 2016). In this case study, 2D unsteady flow simulation was performed since it represents spatially varied flow hydraulics (Horritt & Bates, 2001). Flood hazard mapping is essential in predicting projected water levels and indicates the degree of vulnerability during the flood event.

To validate the performance of the UAV-derived DTM, the simulation results were compared with the simulation results using AW3D DEM (12.5 m resolution) as it performed better than other global DEMs (Courty et al., 2019) and the field observations. The difference in ground representation by terrain models from global source and DTM developed in this study (Fig.9) which clearly shows the superior representation of the ground features by DTM (c) compared to other global DEMs (a & b).

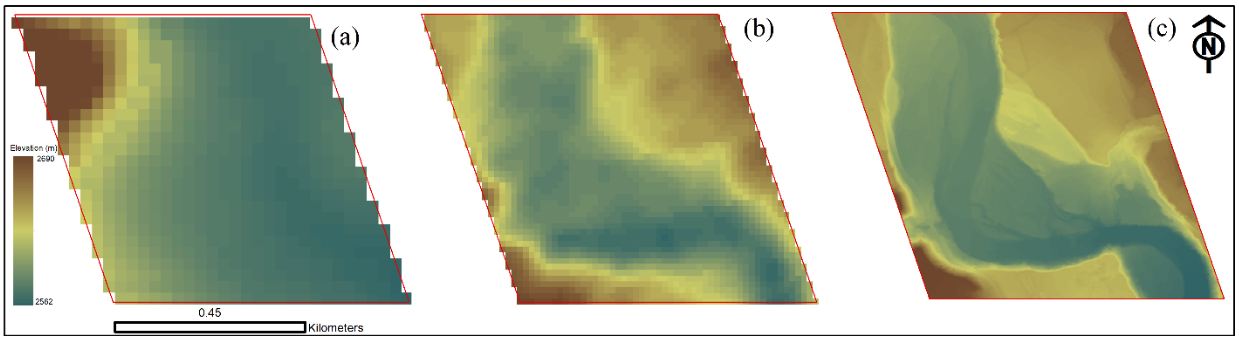

Fig. 9. Global digital elevation model comparison with LiDAR DTM, (a) ASTER DEM-30m, (b) ALOS DEM-12.5m, and (c) LiDAR-derived UAV DTM-1m.

The Cyclone AILA (2009) flow was simulated since it was the highest recorded flow in the study area, causing major flooding in the area, and was used for field validation. The results of flood analysis using ALOS DEM and DTM are illustrated (Fig. 10). The simulation was carried out with the same parameters and input data except for the terrain model. The result shows that even the best-performing global digital terrain models are inadequate and rarely produce accurate results. The simulated flood inundation extent for ALOS DEM was smaller and unrealistic, which can be attributed to its coarse resolution and requirement for hydrological correction to the original DEM. The presence of spikes and sinks in the DEM and river channel greatly impacts the flood inundation depth by damming the routed flow in the simulation, which is why there are unusually high flood depths in the result.

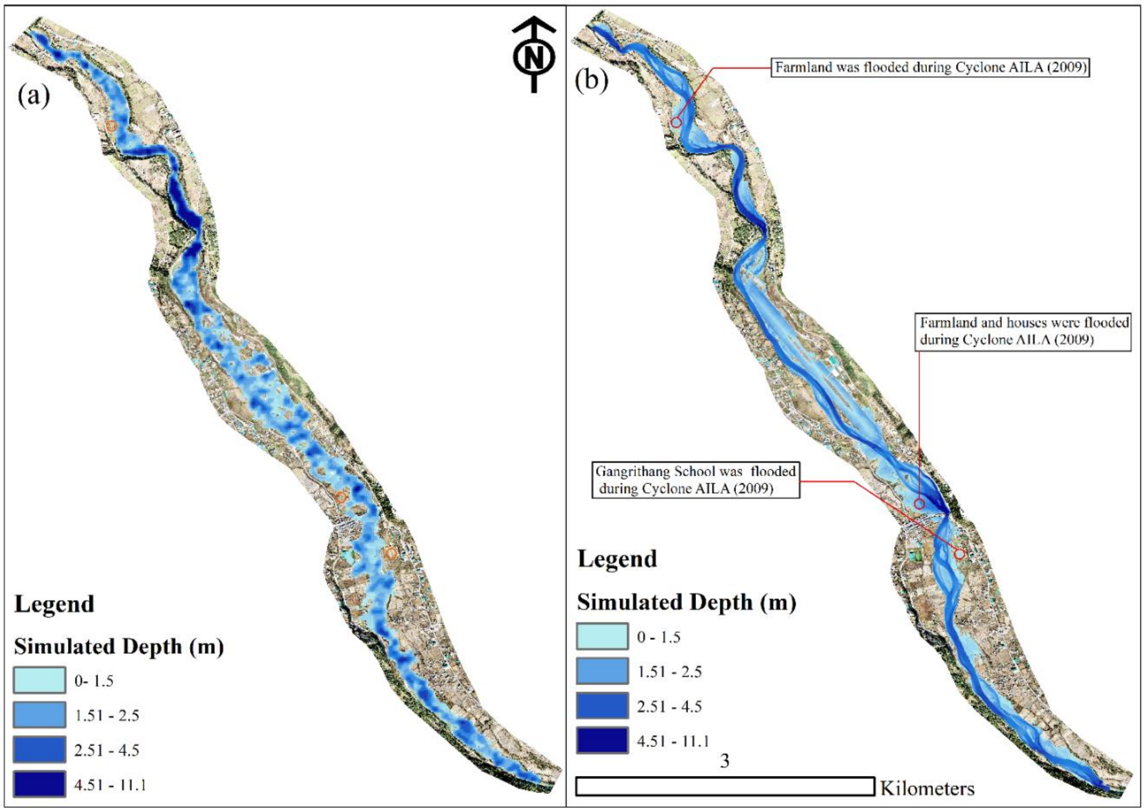

Fig. 10. Comparison of flood extent and depth obtained from flood simulation: (a) ALOS DEM; (b) LiDAR-equipped UAV-derived DTM.

The simulation result using the DTM produces more realistic results that are comparable to the field observations. The simulated flood inundation extent corresponds well to the observed data (Fig. 10). The simulated flood depth for different return periods and events are shown in Fig. 11.

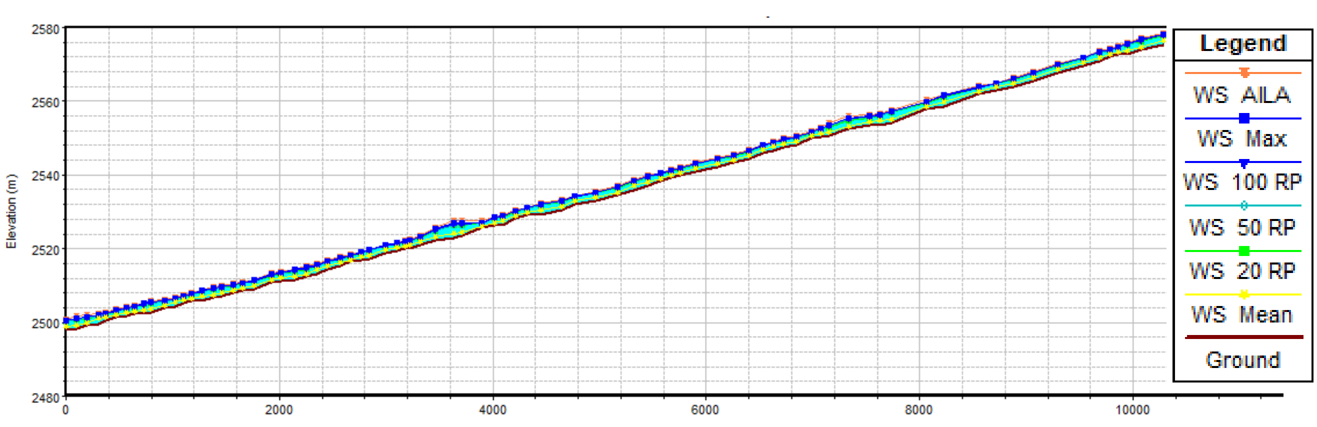

Fig. 11. Longitudinal profile of study area with simulated flood depth for different scenarios extracted from HEC-RAS model

Floods are one of the most commonly occurring natural disasters, and their frequency is expected to increase due to climate change, land use changes, and rapid urbanization (Muhadi et al., 2020). Furthermore, the Himalayan countries are exposed to the threat of potential Glacial Lake Outburst Floods (GLOFs), whose frequency and intensity are expected to increase in the future. Understanding the degree of risks posed by flood/GLOF is essential in planning and designing appropriate adaptation and mitigation measures. Flood hazard maps are fundamental tools for managing flood risks, urban planning, and disaster preparedness. The use of UAVs and LiDAR technologies in recent years is a promising approach to generating accurate topographic data. The LiDAR-derived DEM/DTM in the context of flood modeling captures small-scale features and small changes in topographical representation, which are critical since flood inundation responses are highly sensitive to them.

However, the classification of ground points from non-ground data for DTM generation is complicated, especially in settled and vegetated areas. The process of ground point classification is iterative, and a proper algorithm must be applied to generate accurate DTMs. The LiDAR sensor does not penetrate water bodies, and the river beds are not represented in LiDAR mapping. The bathymetric LiDAR, a specialized remote sensing technology, can be used to operate over water to collect bathymetric data. Also, field-surveyed cross-sections of the rivers can be integrated with the LiDAR-generated DTM to produce proper DTMs. In addition, LiDAR sensors are expensive equipment even for UAVs and require huge storage and computing resources, which are financially unviable for a developing country.

6. Conclusions

In this study, we demonstrated the methodology to generate DTM using LiDAR-equipped UAV and its application in flood mapping. The LiDAR-equipped UAVs are capable of providing accurate and high-resolution terrain models. An accurate representation of the ground surface is essential for flood modeling and management (Muhadi et al., 2020) as the performance of the model is highly dependent on the DTM accuracy. The simulated results demonstrate the significant influence of DTM accuracy in flood depth and the inundation extent, which affirms the use of high-resolution terrain models, especially in small-scale flood modeling studies. The UAV-LiDAR systems can capture and identify small topographical features like buildings, bridges, walls, vegetation, etc., which can have a substantial influence on flood pathways and flood travel time. A terrestrial survey of river bathymetry and its integration with the terrain models is vital to produce more accurate flood maps and flood zone delineation.

Since the UAV platform is equipped with GNSS and RTK integrated, georeferencing was obtained without GCPs, as laying GCPs over a large area can be tedious. We conclude that RTK-integrated UAVs provide highly accurate results, presenting a viable alternative to global products, especially in flood mapping and land use planning. The simulated flood result using DTM generated through this study shows a very close inundation extent to the observed flood in the Chamkhar Valley. To improve the accuracy, further surveys in combination with GCPs and river bathymetry need to be conducted.

References

1. Bhutan Civil Aviation Authority, B. (2017). Bhutan Air Navigation Regulations-UAS Operations. In *Bhutan Civil Aviation Authority, BCAA* (Issue May).
2. Brunner, G. W., & CEIWR-HEC. (2016). HEC-RAS River Analysis System: User Manual 1D and 2D Version 5.0. *US Army Corps of Engineers*, *February*, 1–790. www.hec.usace.army.mil
3. Casas, A., Benito, G., Thorndycraft, V. R., & Rico, M. (2006). The topographic data source of digital terrain models as a key element in the accuracy of hydraulic flood modelling. *Earth Surface Processes and Landforms*, *31*(4), 444–456. https://doi.org/10.1002/esp.1278
4. Courty, L. G., Soriano-Monzalvo, J. C., & Pedrozo-Acuña, A. (2019). Evaluation of open-access global digital elevation models (AW3D30, SRTM, and ASTER) for flood modelling purposes. *Journal of Flood Risk Management*, *12*(S1). https://doi.org/10.1111/jfr3.12550
5. Furby, B., & Akhavian, R. (2024). A Comprehensive Comparison of Photogrammetric and RTK-GPS Methods for General Order Land Surveying. *Buildings*, *14*(6). https://doi.org/10.3390/buildings14061863
6. Harwin, S., Lucieer, A., & Osborn, J. (2015). The impact of the calibration method on the accuracy of point clouds derived using unmanned aerial vehicle multi-view stereopsis. *Remote Sensing*, *7*(9), 11933–11953. https://doi.org/10.3390/rs70911933
7. Horritt, M. S., & Bates, P. D. (2001). Effects of spatial resolution on a raster-based model of flood flow. *Journal of Hydrology*, *253*(1–4), 239–249. https://doi.org/10.1016/S0022-1694(01)00490-5
8. Jakovljevic, G., Govedarica, M., Alvarez-Taboada, F., & Pajic, V. (2019). Accuracy assessment of deep learning-based classification of LiDAR and UAV points clouds for DTM creation and flood risk mapping. *Geosciences (Switzerland)*, *9*(7). https://doi.org/10.3390/geosciences9070323
9. Jiménez-Jiménez, S. I., Ojeda-Bustamante, W., Marcial-Pablo, M. D. J., & Enciso, J. (2021). Digital terrain models generated with low-cost UAV photogrammetry: Methodology and accuracy. *ISPRS International Journal of Geo-Information*, *10*(5). https://doi.org/10.3390/ijgi10050285
10. Liu, X. (2008). Airborne LiDAR for DEM generation: Some critical issues. *Progress in Physical Geography*, *32*(1), 31–49. https://doi.org/10.1177/0309133308089496
11. Manfreda, S., McCabe, M. F., Miller, P. E., Lucas, R., Madrigal, V. P., Mallinis, G., Dor, E. Ben, Helman, D., Estes, L., Ciraolo, G., Müllerová, J., Tauro, F., de Lima, M. I., de Lima, J. L. M. P., Maltese, A., Frances, F., Caylor, K., Kohv, M., Perks, M., … Toth, B. (2018). On the use of unmanned aerial systems for environmental monitoring. *Remote Sensing*, *10*(4). https://doi.org/10.3390/rs10040641
12. Martínez-Carricondo, P., Agüera-Vega, F., & Carvajal-Ramírez, F. (2023). Accuracy assessment of RTK/PPK UAV-photogrammetry projects using differential corrections from multiple GNSS fixed base stations. *Geocarto International*, *38*(1), 1–16. https://doi.org/10.1080/10106049.2023.2197507

13. Muhadi, N. A., Abdullah, A. F., Bejo, S. K., Mahadi, M. R., & Mijic, A. (2020). The use of LiDAR-derived DEM in flood applications: A review. *Remote Sensing*, *12*(14), 1–20. https://doi.org/10.3390/rs12142308
14. Ozdemir, H., Sampson, C. C., De Almeida, G. A. M., & Bates, P. D. (2013). Evaluating scale and roughness effects in urban flood modelling using terrestrial LIDAR data. *Hydrology and Earth System Sciences*, *17*(10), 4015–4030. https://doi.org/10.5194/hess-17-4015-2013
15. Puno, G. R., Marin, R. A., Angelica Amper, R. L., & Allan Talisay, B. M. (2018). Flood simulation using geospatial models in Manupali Flood simulation using geospatial and hydrologic models in Manupali Watershed, Bukidnon, Philippines. *Philippines Article in Journal of Biodiversity and Environmental Sciences*, *294*(3), 294–303. http://www.innspub.net
16. Raber, G. T., Jensen, J. R., Hodgson, M. E., Tullis, J. A., Davis, B. A., & Berglund, J. (2007). Impact of lidar nominal post-spacing on DEM accuracy and flood zone delineation. *Photogrammetric Engineering and Remote Sensing*, *73*(7), 793–804. https://doi.org/10.14358/PERS.73.7.793
17. Sampson, C. C., Smith, A. M., Bates, P. D., Neal, J. C., & Trigg, M. A. (2016). Perspectives on open access high resolution digital elevation models to produce global flood hazard layers. *Frontiers in Earth Science*, *3*(January), 1–6. https://doi.org/10.3389/feart.2015.00085
18. Shahbazi, M., Théau, J., & Ménard, P. (2014). Recent applications of unmanned aerial imagery in natural resource management. *GIScience and Remote Sensing*, *51*(4), 339–365. https://doi.org/10.1080/15481603.2014.926650
19. Štroner, M., Urban, R., Reindl, T., Seidl, J., & Brouček, J. (2020). Evaluation of the georeferencing accuracy of a photogrammetric model using a quadrocopter with onboard GNSS RTK. *Sensors (Switzerland)*, *20*(8). https://doi.org/10.3390/s20082318
20. Taddia, Y., Stecchi, F., & Pellegrinelli, A. (2020). Coastal mapping using dji phantom 4 RTK in post-processing kinematic mode. *Drones*, *4*(2), 1–19. https://doi.org/10.3390/drones4020009
21. Trepekli, K., Balstrøm, T., Friborg, T., & Fog, B. (2022). *UAV - borne , LiDAR - based elevation modelling : a method for improving local - scale urban flood risk assessment*. *0123456789*. https://doi.org/10.1007/s11069-022-05308-9
22. Tsubaki, R., & Fujita, I. (2010). Unstructured grid generation using LiDAR data for urban flood inundation modelling. *Hydrological Processes*, *24*(11), 1404–1420. https://doi.org/10.1002/hyp.7608
23. Udin, W. S., & Ahmad, A. (2014). Assessment of photogrammetric mapping accuracy based on variation flying altitude using unmanned aerial vehicle. *IOP Conference Series: Earth and Environmental Science*, *18*(1), 1–7. https://doi.org/10.1088/1755-1315/18/1/012027
24. Žabota, B., & Kobal, M. (2021). Accuracy assessment of uav-photogrammetric-derived products using ppk and gcps in challenging terrains: In search of optimized rockfall mapping. *Remote Sensing*, *13*(19), 1–31. https://doi.org/10.3390/rs13193812

National Centre for Hydrology and Meteorology
Thimphu, Bhutan
Tel.No: +975-2-327202
www.nchm.gov.bt